THE UNIVERSITY *of* EDINBURGH

The growth of massive seed black holes and their impact on their host galaxies

Daniel S. Eastwood

Doctor of Philosophy
The University of Edinburgh
June 2019

Lay Summary

Black holes around a billion times the mass of the Sun have been observed to have existed when the Universe was only a fraction of its current age, at less than a billion years old. Exactly how these super-massive objects formed within this, in cosmological terms, short timescale is not fully understood. The first generation of stars that formed in the Universe are thought to have had very short lifetimes before collapsing to form black holes. However, these black holes are thought to be too low in mass to grow to become super-massive within this first billion years. More exotic formation mechanisms are required to provide black holes which have higher initial masses and are therefore capable of reaching super-massive status. Such objects are known as massive seed black holes. One of the most promising mechanisms for forming seed black holes is known as direct collapse and results in the formation of a black hole with a mass of up to a million times the mass of the Sun.

This thesis details my investigations into how the development of galaxies in the early universe is affected by massive seed black holes formed via the direct collapse mechanism. I focus on using analytic modelling techniques to study how the presence of these most massive of seed black holes influenced the growth of galaxies in the early universe.

In Chapter 2, I create a simple model of a galaxy forming as a disc around a massive seed black hole. I follow the evolution of the system as the seed black hole grows from formation to become a super-massive black hole within the first billion years of the Universe. During this time the disc is growing, gaining more and more mass from gas falling into the system under gravity. As the disc grows in mass it will become more susceptible to collapsing under the gravitational force it exerts on itself, leading to the formation of stars from the collapsing gas. For the first time I show how the gravity of the black hole has a stabilising effect on the disc, preventing this collapse until the disc gains more mass. The black

hole therefore reduces the extent to which the disc can form stars, decreasing the overall rate of star formation. This can have a lasting effect on the evolution of the galaxy as the black hole grows and, in some circumstances, the black hole can prevent the formation of stars entirely.

In Chapter 3, I adapt the model to test whether a super-massive black hole can grow from a seed fed solely through the inflow of gas from the galactic disc. The inflow of gas within the disc can be modelled as driven by viscosity which is brought on by the instability of the disc. I find that this viscosity-driven inflow of gas is not sufficient to feed the required black hole growth to form a super-massive black hole within the first billion years of the Universe. This indicates that more efficient inflow mechanisms are needed to grow super-massive black holes in the early universe. I show that, as the merging of two similar mass galaxies can lead to the total disruption of any disc, such an event can provide the required inflow of gas to feed the formation of a super-massive black hole.

Both of these studies have lent some weight to an emerging theoretical picture for the potential growth of super-massive black holes seeded through direct collapse whereby the massive seeds originally form in separate haloes from their eventual host galaxies. Following their formation, the systems that host direct collapse seeds fall into the dark matter haloes of neighbouring star-forming galaxies which they subsequently merge with. In chapter 4, I investigate the process of a massive seed black hole system moving through a dark matter halo. As a massive system, the gravitational pull of the object falling in perturbs the background density to form a wake which drags behind it. This wake in turn has a gravitational pull and acts to slow the infalling object. This drag force is known as dynamical friction. As the massive seed black hole falls in, dynamical friction acts to convert the potential energy of the system into heating the gas of the halo. I find that the total energy released and the time it takes for the infalling system to reach the galaxy at the centre both depend on the mass of the infalling system. In certain circumstances the heating from dynamical friction is significant and can even be the primary mechanism for heating the gas in the halo while the massive seed black hole system falls in. This has potential consequences for black hole mass estimates based on brightness measurements. Such mass estimates are inferred by assuming that the power observed is solely generated by black hole growth. As dynamical friction heating may be providing a significant proportion of the observed power, black hole masses may be over-estimated in certain circumstances.

Abstract

The recent discovery of an 800 million solar mass black hole powering a quasar at a redshift corresponding to 690 million years after the Big Bang is the latest in a growing list of observations of super-massive black holes (SMBHs) that were most likely seeded with masses larger than those expected from the remnants of the first generation of stars. This thesis investigates the consequences of the seeding of SMBHs by massive black holes on galaxy evolution through a combination of analytic modelling techniques.

Firstly, I analytically model the growth of gravitational instabilities in an isolated proto-galaxy disc as it progresses into a fully-formed galaxy in the presence of a massive seed black hole formed directly through isothermal collapse. The model shows for the first time how the gravitational effects of a seed black hole lead to an increase in the stability of the disc and an increase in the star formation timescale in the region of the disc close to the black hole. This gravitational imprint of the black hole on the galactic disc has the effect of suppressing star formation. To investigate if this has a lasting effect on the properties of seed hosting galaxies, I evolve the disc galaxy model from the epoch of seed formation down to $z \sim 6$. I show how star formation in seed hosting galaxies is further regulated by a combination of gravitational stability and the accretion of gas onto the black hole, leading to a scenario where the resulting ratio of black hole to stellar mass at $z = 6$ is significantly higher than observed in the local universe.

I also investigate how the growth of massive seed black holes is regulated by the mass and momentum transport in the disc. The inward accretion of gas towards the central massive black hole and therefore the accretion of gas onto the black hole itself is a function of the stability of the disc. The stabilising effect of the black hole therefore has the potential to regulate the inflow of gas, depending on the relative masses of the galaxy disc and black hole. I find that even in the regime where the inflow rate is not affected by the presence of the black hole,

viscosity driven accretion is too inefficient for even massive seeds to grow into a SMBHs by $z \sim 6$. This indicates the isolated growth of SMBHs is not possible. Indeed, merger events or other processes which are efficient at dissipating angular momentum are required to provide the necessary rapid accretion of gas for SMBHs to form.

Finally, I study the dynamical heating of a dark matter halo through the accretion of massive black hole systems. Modelled as both a black hole embedded in its own subhalo and as a naked black hole, the infall of the black hole system acts as a perturber to the density of the central halo, converting potential energy to heat the gas of the central halo through dynamical friction. The timescale over which this infall occurs decreases with a larger perturber mass relative to the central halo mass. The total energy released through black hole accretion during the period of infall is strongly dependent on the black hole growth model. Generally, the total energy from black hole growth exceeds the total energy from dynamical friction. However, the energy released through dynamical friction reaches a maximum when the perturber's proximity to the centre of the central halo is minimised, generally after black hole accretion has ceased. There is therefore a period of time where dynamical friction is the primary source of heating within a halo, potentially contributing to the luminosities of some distant quasars and leading to over-estimates in inferred black hole masses.

Declaration

I declare that this thesis was composed by myself, that the work contained herein is my own except where explicitly stated otherwise in the text, and that this work has not been submitted for any other degree or professional qualification except as specified.

Parts of this work have been published in Eastwood & Khochfar (2018).

Parts of this work have been published in Eastwood et al. (2019).

(*Daniel S. Eastwood, June 2019*)

Acknowledgements

First and foremost I would like to thank Sadegh for his support and guidance over the last 3 and a half years. I could not have asked for a better supervisor. You always knew when to give me my freedom and when to provide the push I needed to keep things moving. Thank you for your patience and understanding, along with your ever-constant good humour. Your thirst for knowledge and enthusiasm for your research are inspirational and I am proud to have worked with you.

Thank you to Jose for all of the constructive advice and encouragement you have given that I will take with me. From rescuing me from my haphazard presentation slides to supporting my applications, you have always gone out of your way to help me and I am truly grateful.

I would also like to thank Ian, Hermine and William, who inspired me to pursue astronomy further and without whom I probably would not have been at the observatory in the first place. I will be forever grateful to you for giving me the opportunities I was very fortunate to receive.

There are too many of you to name but to all of my Astrobuddies: thank you for all of the laughs, rants, chats and stories. You are all such ridiculously bright and wonderful people and it has been a blast studying alongside you. The Royal Observatory is an inspirational place to work and I thank everyone who has helped create such a friendly and welcoming atmosphere over the last 3 and a half years.

Mum, Dad, Steph and Jussie, thank you for all of your love and support, I could not have done this without you.

Finally, I would like to thank my wife, Julia. Thank you for your love and encouragement throughout the last few years and for your endless patience during the completion of this thesis.

For Julia

Contents

List of Figures

List of Tables

Chapter 1

Introduction

Super-massive black holes observed to exist within the first billion years since the Big Bang (e.g., Bañados et al. 2018) likely have massive progenitors which formed prior to their host galaxies. These progenitors, known as massive seed black holes, are thought to have been more massive than the remnants from the first stars. Black holes formed through the direct collapse of gas clouds are an attractive theoretical progenitor as they provide the most massive seeds (Bromm & Loeb 2003; Begelman et al. 2006). The main focus of this thesis is to explore the consequences these massive seed black holes have on galaxy formation and evolution.

1.1 Massive seed black holes: What are they and why do we need them?

In this section I begin by discussing the idea of a black hole and the significance of the existence of SMBHs in the early universe. I then introduce the different seed black hole formation mechanisms, comparing their formation epochs and masses. From this we can infer which mechanism is the most capable of seeding SMBHs.

1.1.1 What is a black hole and how do they form?

When the self-gravity of an object is large enough to overcome all sources of pressure support, gravitational collapse becomes inevitable. The resulting compact object, warps the region of space-time around it such that light cannot escape it. This is shown classically as the point when the escape velocity, $V_{\rm esc}$, of an object exceeds the speed of light, $c = 2.998 \times 10^5\,{\rm km/s}$, at some radius, R.

$$V_{\rm esc} \equiv \sqrt{\frac{2GM(<R)}{R}} > c \tag{1.1}$$

where $G = 4.302 \times 10^{-3}\,{\rm pc\ M_\odot}^{-1}\,({\rm km/s})^2$ is the gravitational constant and $M(<R)$ is the mass of the object within radius, R. The radius where $V_{\rm esc} = c$ is known as the event horizon of a black hole. Inside of this radius nothing can escape as the velocity required to do so is greater than the universal speed limit that is the speed of light. Solving Equation 1.1 for this case we find the Schwarzschild radius.

$$r_{\rm Sch} \equiv \frac{2GM}{c^2} \tag{1.2}$$

This defines the event horizon for a non-rotating black hole with zero charge, known as a Static or Schwarzschild Black Hole.

For a black hole to form, an object has to become dense enough that it has an event horizon. For example, if the Earth were to undergo a gravitational collapse such that its entire mass ($M_\oplus = 5.97 \times 10^{24}$ kg) was compressed within its Schwarzschild radius, $r_{\rm Sch} = 8.87$ mm, it would become a black hole. Thankfully, there are several forces, such as electrostatic repulsion, acting as pressure support against such gravitational collapse. An object would need to have a stronger gravitational field, and therefore be much more dense, to overcome this pressure support.

In stars, this support comes from the energy released through nuclear fusion. At the end of a star's life, fusion can no longer take place and the loss of pressure support leads to the star collapsing under its own gravity. Whether this results in a supernova event and the formation of a black hole from the stellar remnant, will depend on the mass and metallicity of the star (De Loore & Doom 1992). As stars end their lives they lose energy and contract, forming a dense, degenerate

gas[1]. For a stellar remnant with a mass of $M \lesssim 5\,\mathrm{M}_\odot$, the gravitational force is insufficient to overcome the degeneracy pressure and the star will become a white dwarf, neutron star or even, theoretically, a quark star (supported by electron, neutron or quark degeneracy pressure). At higher masses, the stronger gravitational force results in the formation of a black hole. A black hole formed from the remnant of a star is known as a stellar black hole.

Observations of stellar black holes have found masses in the range of $M_\bullet \approx 5 - 11\mathrm{M}_\odot$. With the advent of gravitational wave astronomy, more massive black holes ($M_\bullet \lesssim 50\,\mathrm{M}_\odot$), thought to be the remnants of massive stars, have been observed during black hole merging events (Abbott et al. 2016; The LIGO Scientific Collaboration et al. 2018).

As I will discuss later, the remnants of the first generation of stars are thought to have generally been more massive and therefore produced more massive stellar black holes. There is still, however, several orders of magnitude between the largest predicted stellar mass black holes and the masses inferred from distant quasars.

1.1.2 Super-massive black holes and high redshift quasars

Super-massive black holes (SMBHs), such as Sagittarius A* at the centre of our Milky-Way, have been observed with masses $M_\bullet \sim 10^{6-10}$ $\mathrm{M}_\odot$ at the centre of galaxies throughout the local universe (Kormendy & Richstone 1995; Magorrian et al. 1998). A significant proportion of galaxy have been observed to have active galactic nuclei (AGNs) from which black hole masses can be inferred (Heckman & Best 2014). Most massive galaxies are thought to play host to a central massive black hole, and the masses of these black holes correlate with the properties of their host galaxies (Magorrian et al. 1998; Merloni et al. 2003; Merritt 2006; Kormendy & Bender 2009; Kormendy & Ho 2013; Heckman & Best 2014; Reines & Volonteri 2015; Thomas et al. 2016). Investigations have looked to higher redshifts in hopes to study these correlations and how SMBHs formed.

For several years the most distant quasar observed to be powered by a SMBH was at $z \sim 7$ (Mortlock et al. 2011). More recently Bañados et al. (2018) detected quasar ULAS J134208.10+092838.61 (hereafter J1342+0928) at $z = 7.54$ with a

[1]The sub-atomic species that makes up the degenerate gas will vary with the mass of the remnant

black hole mass of $M_\bullet = 8 \times 10^8$ $M_\odot$. At this redshift the Universe is only 690 million years old for the standard ΛCDM model, leading to the question: how did such a massive black hole form this shortly after the Big Bang? Indeed, there are a more than a handful of such objects with masses of $M_\bullet \sim 10^9\,M_\odot$ that have been discovered to date at high redshift $z > 6$ (Fan et al. 2006; De Rosa et al. 2014; Mazzucchelli et al. 2017; Reed et al. 2019).

The growth of compact objects such as black holes occurs through either the accretion of surrounding material or mergers. The process of accretion heats the material falling onto the black hole. The infalling material can then radiate, efficiently converting the potential energy gained to radiation. The rate at which the black hole can grow is classically limited by the balancing of the resulting radiation pressure against the infall of material under gravity at hydrostatic equilibrium. This is the Eddington limit which gives the following as the theoretical limit to the growth rate of a black hole:

$$\dot{M}_{\bullet,\,\mathrm{Edd}} = \frac{M_\bullet}{\tau_{\mathrm{Sal}}} \tag{1.3}$$

where $\tau_{\mathrm{Sal}} = 0.45\,\eta/(1-\eta)$ Gyr is the Salpeter time-scale and η is the radiative efficiency (Rybicki & Lightman 1986). The radiative efficiency describes how efficiently the gravitational potential is converted into radiation. η is a function of the radius of the innermost stable circular orbit which depends on the spin and mass of the black hole. The relative rotation of the accretion disc with the black hole spin also plays a role, though typically $\eta \sim 0.1$ (see, e.g. King et al. 2008). With this fiducial value the Salpeter time-scale becomes $\tau_{\mathrm{Sal}} = 50$ Myr. A black hole with some initial mass $M_{\bullet,\,\mathrm{i}}$ at t_i, growing continuously at the Eddington limit, will reach the following mass at time, t:

$$M_\bullet(t) = M_{\bullet,\,\mathrm{i}}\,\exp\left(\frac{t - t_\mathrm{i}}{t_{\mathrm{Sal}}}\right) \tag{1.4}$$

The growth rate of a black hole is then limited to grow on an e-folding time with the Salpeter time-scale.

To reach Equation 1.3 and calculate the Salpeter timescale we have assumed spherical symmetry and that the material being accreted is purely ionized hydrogen. Super-Eddington accretion should therefore be viable through a number of scenarios (Ohsuga et al. 2005; Pacucci et al. 2015; Inayoshi et al.

2016; Pacucci et al. 2017; Takeo et al. 2019). To truly test the viability of these super-Eddington growth scenarios in a cosmological context would require large-scale simulations to reach a resolution beyond the limit of modern technology. Cosmological hydrodynamic simulations struggle to reach densities above $n_{\rm res} \sim 10^4\,{\rm cm}^{-3}$ (e.g. Johnson et al. 2011), at least two orders of magnitude below the densities required to test super-Eddington accretion onto stellar black holes (Inayoshi et al. 2016). Super-Eddington accretion is therefore still largely untested and cannot be ruled out. Note however, cosmological hydrodynamic zoom simulations which model feedback effects and black hole growth based on properties within the black hole's sphere of influence have struggled to even reach the Eddington accretion rate (see, e.g. Johnson et al. 2011; Latif et al. 2018).

The presence of massive black holes less than a billion years after the Big Bang begs the question: How did such massive compact objects form in what is a relatively short space of time? In the following section I outline three different theoretical mechanisms for the formation of black holes in the early universe: (**1**) the remnants of the first generation of stars, (**2**) the massive black holes formed through run-away collisions of stars in the collapsed cores of star clusters, and (**3**) the direct collapse of primordial gas in atomic cooling haloes into massive black holes.

1.1.3 Population III remnants

The first generation of stars, known as Population III (PopIII) stars, are expected to form out of primordial gas in haloes with virial temperatures $T_{\rm vir} < 10^4\,{\rm K}$ known as mini-haloes (Bromm et al. 2009). These low-mass haloes are expected to collapse around $z \sim 20 - 30$. The zero-metallicity gas from which PopIII stars form by definition is absent of either metals or dust. Hence, the dominant mini-halo cooling species is molecular hydrogen. The resulting cooling of the gas leads to fragmentation during cloud collapse and stars are able to form. When compared to star formation in higher metallicity gas, the relative inefficiency of H_2 cooling results in significantly higher initial stellar masses (Bromm et al. 1999). Predictions of the PopIII initial mass function (IMF) are often referred to as being "top-heavy" when compared to a local IMF, in that more massive stars take up a larger fraction of the total number of stars formed.

As the first stars are expected to be typically more massive than later generations, it is reasonable to infer that their remnants would be massive also. By assuming

non-rotating stars, Woosley et al. (2002) calculated the mass of a PopIII remnant as a function of the mass of the PopIII star (see Figure 1.1):

- The lowest PopIII stellar mass range expected to form black holes ($M_\star \sim 25 - 140\,\mathrm{M}_\odot$) are thought to produce remnants with approximately half their mass.
- Stars with $M_\star \sim 140 - 260\,\mathrm{M}_\odot$ have no remnants as the star is destroyed through nuclear explosions in what is known as pair instability supernovae.
- Stars with masses $> 260\,\mathrm{M}_\odot$, black holes are again expected to form when the star collapses.

In this final case the black hole is expected to form inside the star, taking up at least half the total mass of the star. Assuming such massive stars can form, they are expected to collapse to form black holes with masses $\gtrsim 150\,M_\odot$ after very short lifetimes (Schaerer 2002). The merging of massive PopIII remnant hosting haloes could potentially result in the formation of clusters of massive black holes at the centre of more massive haloes which, in turn, could merge into more massive black holes (Madau & Rees 2001).

However, there are problems with this picture of black hole seed formation. The IMF of PopIII stars is still largely uncertain (see review, Klessen 2018). For example, if several low mass PopIII stars form within a single halo, fewer high mass stars are expected to form, while on the other hand, lone PopIII stars forming in mini-haloes could also result in lower final stellar masses (Volonteri 2010). Other work has also shown that the expected number density of PopIII remnant black holes is too low for mergers to play a key role in their growth (Johnson et al. 2013). This leaves PopIII remnant black holes having to grow rapidly via accretion for a long period in order to seed SMBHs. A recent study of the *Renaissance* simulations by Smith et al. (2018) found rapid PopIII remnant growth to be unsustainable, with the fastest growing black holes only growing in mass by around only 10%. This limited growth indicates that PopIII remnants would struggle to reach even intermediate masses, let alone the $M_\bullet \sim 10^9\,\mathrm{M}_\odot$ SMBHs at $z \sim 6$. It is therefore more likely that the seeds of SMBHs are more massive than PopIII remnants, commanding a more significant gravitational influence over their host haloes and avoiding the need for such intensive gas accretion.

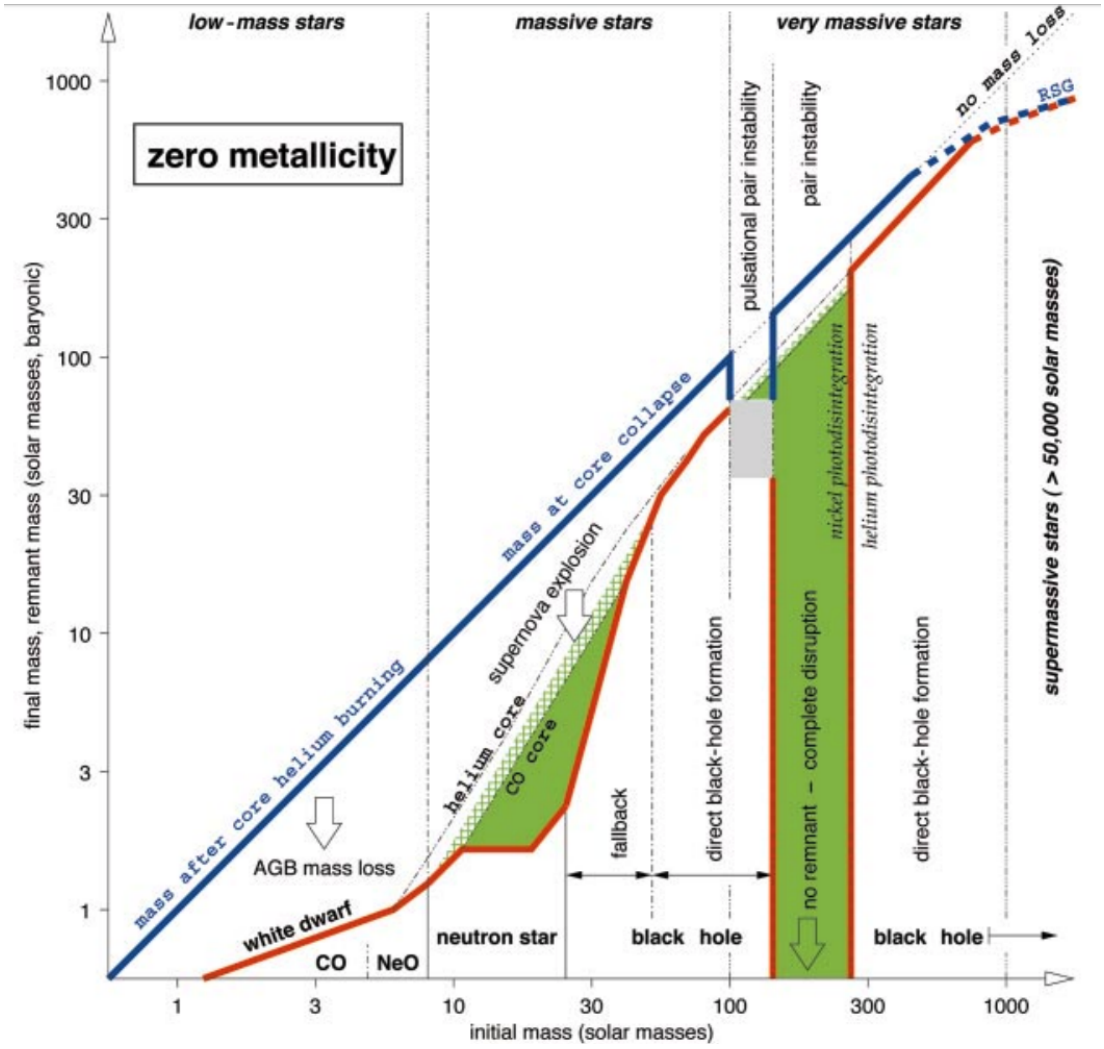

Figure 1.1 *Taken from Woosley et al. (2002), Figure 12: "The x axis gives the initial stellar mass. The y axis gives both the final mass of the collapsed remnant (thick red curve) and the mass of the star when the event that produces that remnant begins (e.g., mass loss in asymptotic giant branch (AGB) stars, supernova explosion for those stars that make a neutron star, etc.; thick blue curve). Dark green indicates regions of heavy-element ($Z > 2$) synthesis and cross-hatched green shows regions of partial helium burning to carbon and oxygen. We distinguish four regimes of initial mass: low-mass stars below $\sim 10\,M_\odot$ that form white dwarfs; massive stars between $\sim 10\,M_\odot$ and $\sim 100\,M_\odot$; very massive stars between $\sim 100\,M_\odot$ and $\sim 10^3\,M_\odot$; and super-massive stars (arbitrarily) above $\sim 10^3\,M_\odot$."*

1.1.4 Star cluster black holes

After the first stars form in mini-haloes (as described above), more massive haloes will be able to form through the merging of mini-haloes. These haloes are expected to have similar virial temperatures ($T_{\rm vir} \gtrsim 10^4\,{\rm K}$) to those thought to collapse to form direct collapse black holes (see following section). However, the haloes will be slightly enriched with metals from their progenitors, allowing the gas to cool and fragment more rapidly, leading to the formation of PopII stars (Omukai et al. 2008). The collapse of a metal enriched halo will initiate a period of efficient star formation and the first star clusters will be born (Clark et al. 2008). The cores of systems are expected to contract as they reach thermal equilibrium, becoming so compact that numerous stellar collisions are likely, leading to the formation of a very massive star (VMS) which could further collapse to form a massive black hole (Omukai et al. 2008; Devecchi & Volonteri 2009; Devecchi et al. 2010; Yajima & Khochfar 2016).

Simulations have shown how runaway collisions of stars can lead to significant mass loss which is made worse at high metallicity (Glebbeek et al. 2009), limiting the possible mass of any VMS remnant seed black holes. At low, but not zero, metallicity the situation is more favourable to the formation of massive seed black holes as mass losses through stellar winds and collisions are reduced. Furthermore, stars at low metallicity with masses $\gtrsim 40\,{\rm M}_\odot$ are predicted to form black hole remnants without losing significant mass through supernovae (Heger et al. 2003).

These compact stellar clusters are expected to form in the nuclei of pre-galactic structures, surrounded by partially stable gas discs (Devecchi & Volonteri 2009). Due to high background intensities of UV photons, any H_2 in these discs is expected to be dissociated, leaving only atomic and metal cooling. This is thought to prevent star formation in the outer part of the disc, allowing the infall of gas to fuel star formation in the dense central region. The resulting compact stellar cluster then undergoes core collapse on fast timescales, forming a VMS and ultimately a seed black hole of mass $M_\bullet \sim 10^3\,{\rm M}_\odot$ at $z \sim 10 - 20$ (Devecchi & Volonteri 2009).

1.1.5 Direct collapse black holes

The formation of black holes through direct collapse has the potential to provide the most massive seeds for the growth of SMBHs. Direct collapse black holes (DCBHs) are predicted to have masses of $M_\bullet = 10^{4-6}\,\mathrm{M}_\odot$ (Bromm & Loeb 2003; Begelman et al. 2006; Agarwal et al. 2012; Latif et al. 2013), $100-1000$ times the masses expected from PopIII remnants. Due to the e-folding nature of Eddington limited accretion, increasing the seed mass reduces the required growth rate for black holes to become super-massive by $z \sim 6$.

DCBHs are thought to form from pristine gas in low-spin, dark matter haloes of virial temperatures of $T_{\mathrm{vir}} \sim 10^4\,\mathrm{K}$ (Eisenstein & Loeb 1995; Bromm & Loeb 2003; Lodato & Natarajan 2006) where atomic cooling can dominate in the absence of metal coolants and the intergalactic UV radiation field is adequate to suppress the formation of H_2 molecules and H^- ions. Gas temperatures of $T_{\mathrm{gas}} \sim 10^4\,\mathrm{K}$ enables the collapse of atomic cooling haloes to occur isothermally. Keeping the gas isothermal will prevent the fragmentation of gas and the formation of stars, forcing gas to collapse into more massive structures and hence aiding the formation of DCBHs. This recipe for the formation of DCBHs does appear to require highly specific conditions which could lead some to question whether the rate of DCBH formation is sufficient to explain the observed number density of quasars, $\phi \sim 1\,\mathrm{Gpc}^{-1}$ (Fan et al. 2003; Shankar et al. 2009). However, theoretical studies have shown these conditions are frequently satisfied in the high redshift universe, allowing for the ubiquitous formation of DCBHs (e.g., Agarwal et al. 2012).

Primordial gas in haloes with virial temperatures of $T_{\mathrm{vir}} \sim 10^4\,\mathrm{K}$ are expected to collapse at $z \sim 10$ to form compact, gas discs (Oh & Haiman 2002; Lodato & Natarajan 2006). The disc material can then rapidly accrete towards the centre of the halo and form a seed black hole, possibly via a temporary super-massive star (SMS) phase (Begelman 2010), provided fragmentation and the subsequent formation of stars can be avoided.

The possibility of fragmentation in collapsing gas clouds is a key issue for the formation of DCBHs. The more a cloud is able to fragment and form stars, the harder it is for a large portion of the gas to go into forming a black hole. In a collapsing cloud the material has to condense while maintaining $T_{\mathrm{gas}} = 10^4$ K to avoid fragmentation. Bromm & Loeb (2003) suggest that if the gas temperature

is only somewhat lower than the virial temperature of the dark matter halo then fragmentation into small clumps is avoided, and the gas will tend to condense isothermally. This isothermal collapse will form large clumps which are then able to continue to collapse further and form DCBHs. The mass of these clumps will be of the order of the Jeans mass of the cloud. The ability for a cloud to collapse to form a DCBH is therefore dependent on the gas temperature and whether the cloud can remain isothermal.

Lodato & Natarajan (2006) show that if we assume some fraction of gas in a halo is able to collapse to form a disc, the ratio of the virial temperature to the gas temperature $T_{\rm vir}/T_{\rm gas}$, along with the spin parameter of the halo, λ, determines the degree to which the gas will fragment. They suggest that if $T_{\rm vir}/T_{\rm gas} \gtrsim 2.9$ the halo will collapse to form a fragmenting disc that will form stars, strongly limiting the fraction of gas available to directly form a seed black hole. However, if a halo is able to maintain $T_{\rm vir}/T_{\rm gas} \sim 1$, fragmentation of the disc is avoided and a significant fraction of the gas will accrete towards the centre, possibly feeding the formation of a DCBH.

This is an interesting point from which one can draw analogues with models of small scale systems such as the formation of a star in gas clouds. Just like in cloud-core-collapse models of star formation, there is a balancing of gravitational potential (the virial temperature) against outward pressures (the gas temperature). When the two terms are equivalent the system in question is in equilibrium and collapse is not possible. Decreasing the pressure term will lead to a collapse of gas to form a compact central object. In the case of the isothermal collapse of haloes, the necessary discrepancy between the pressure and gravitational terms is only slight. If the pressure term is drastically lowered from equilibrium through highly significant cooling (e.g. H_2 cooling), the collapse will not be isothermal and fragmentation will occur during the formation of the proto-galaxy disc.

So the question is therefore, how can haloes maintain a gas temperature similar to their virial temperature? Dark matter haloes with virial temperatures of $T_{\rm vir} \sim 10^4\,{\rm K}$ can achieve this when the dominant cooling species is atomic hydrogen. Atomic hydrogen can cool the gas of a halo down slightly below $T_{\rm gas} \sim 10^4\,{\rm K}$ through collisional excitation and radiative de-excitation. Further cooling can be prevented through dissociation of molecular hydrogen which could otherwise cool gas down to around $T \sim 100$ K, making the gas unstable to fragmentation.

Metal enrichment of halo gas, a product of star formation in haloes, can also lead to further fragmentation. Enriched haloes have a more efficient cooling than those with gas made of only hydrogen and helium, leading to greater fragmentation and star formation during collapse. However, it has been suggested that fragmentation can still be avoided in gas enriched haloes where the metallicity of the gas is still below a critical threshold (Santoro & Shull 2006; Latif et al. 2016).

Even though DCBHs are expected to form in haloes with $T_{\rm vir} \gtrsim 10^4\,K$ where atomic hydrogen dominates the gas composition, molecular hydrogen can still be produced in high density regions through three-body hydrogen reactions, or at low densities ($n < 10^3\,{\rm cm}^{-3}$) via the H^- channel (Equations 1.5 and 1.6) (Agarwal et al. 2016a):

$$H + e^- \longrightarrow H^- + \gamma \tag{1.5}$$

$$H^- + H \longrightarrow H_2 + e^- \tag{1.6}$$

Calculations have shown in the absence of any strong UV flux, the universal molecular fraction reaches $x_{H_2} \approx 10^{-3}$ as H_2 forms in dense collapsing gas (Oh & Haiman 2002). Molecular hydrogen can cool gas to $T \sim 100$ K. The rotational and vibrational modes of the H_2 molecule have lower excitation energies than the states available to atomic hydrogen, meaning the cross-section of collisional excitation of these modes remain significant at lower gas temperatures than the cross-section for the collisional excitation of atomic hydrogen. This results in molecular cooling remaining effective at lower temperatures than atomic cooling. For the formation of DCBHs, the gas temperature must be kept around 10^4 K. To avoid cooling below this temperature (via molecular cooling), H_2-dissociation is possible through Lyman-Werner (LW) photons (UV photons with energies between $11.2 - 13.6\,{\rm eV}$; see Equation 1.7). The molecular fraction of the gas can also be limited via the photo-detachment of H^- by photons with energies greater than 0.76 eV (see Equation 1.8).

$$H_2 + \gamma_{\rm LW} \longrightarrow H + H \tag{1.7}$$

$$H^- + \gamma_{0.76} \longrightarrow H + e^- \tag{1.8}$$

Bromm & Loeb (2003) calculate $J_{\rm crit}$, the critical intensity of LW photons required to suppress the formation of molecular hydrogen even in dense regions. Their results show that the critical intensity required from quasar and PopIII star sources are higher than the background level expected at $z \sim 10$. The background intensity is expected to be fairly uniform due to the large mean free path of LW photons and therefore this suggests that quasar and PopIII star sources would be incapable of preventing the build up of H_2 and the resulting cooling. The Pop II model did give a critical intensity of the order of the expected background value, suggesting Pop II stars could therefore produce the required UV flux to prevent H_2 formation. However Bromm & Loeb (2003) note, as Pop II stars form from higher metallicity gas, dust grains which can catalyze the formation of H_2 will also be present. Therefore, the source of LW photons from Pop II stars must exist in entirely separate haloes from the black hole seeds.

Other work has suggested that even Pop II stars cannot provide the critical background intensity (Shang et al. 2010; Agarwal et al. 2012, 2014). Instead of a critical background intensity, it is argued that due to the discrete nature of LW sources, the local intensity of LW photons will actually fluctuate above and below the background level and that some regions, such as haloes neighbouring Pop II star-forming haloes, will have local intensities much higher than the background level (Dijkstra et al. 2008), enabling DCBH formation. By considering the local LW radiation intensity, some models have shown that the local intensity can be up to $\sim 10^6$ times higher than the background level (Agarwal et al. 2012, 2014). These models where LW radiation field varies spatially have shown that the clustering of sources in close proximity to pristine haloes is key to the formation of DCBHs. In fact simulations have shown that the LW radiation field is such that the seeding of quasar black holes by DCBHs is likely commonplace (Agarwal et al. 2012).

A further problem which must be addressed by DCBH formation theory is the redistribution of angular momentum. If angular momentum cannot be efficiently transferred during collapse, the gas will be unable to accrete inwards. The resulting disc will grow until it becomes unstable to fragmentation, leading to the formation of stars instead of a black hole seed. The dimensionless spin parameter $\lambda = J|E|^{1/2}/(GM^{5/2})$ is a measure of the total angular momentum of a halo, where E and M are the total energy and mass of the halo, respectively. Numerical simulations have found a log-normal distribution in the spin parameters of haloes with the moments $\bar{\lambda} = 0.05$ and $\sigma_\lambda = 0.5$ (Mo et al. 1998). This implies that

for a typical $T_{\rm vir} \gtrsim 10^4\,{\rm K}$ halo at $z \sim 10$, the angular momentum would cause any isothermal collapse to lead to the formation of a disc. To further congregate the material of the halo in its centre will require the transfer of the angular momentum of the disc outwards via some viscosity or gravitational instability. It is therefore thought that DCBH formation is more likely to occur in lower-spin haloes (Eisenstein & Loeb 1995). These haloes would have lower total angular momentum and therefore the required efficiency of angular momentum redistribution is lower. Furthermore, it can be noted that in some haloes, it is sufficient for only the low angular momentum fraction of the material to go into forming a black hole seed. However, significant transfer is still required to reach the necessary black hole seed mass.

Several processes have been put forward to tackle this issue. One such mechanism is the "bars-within-bars" process (Begelman et al. 2006) which assumes that the thickness and density of a newly formed, rotationally supported, proto-galaxy disc are such that the self gravity of the disc leads to a bar instability. A bar can form once the rotational support of disc material reaches a critical level. The bar then causes a "quasi-stable inflow" of material as angular momentum is transferred outwards through gravitational torques on a dynamical timescale. Further cooling of the gas can lead to a greater inflow of material on shorter timescales, as another, smaller bar instability forms within the previous one. This cascade of instabilities gives the mechanism its name. This mechanism is expected to produce the required strong flow of material to form a massive central object.

Lodato & Natarajan (2006) suggest that in collapsing low-spin haloes, the self-gravity of the resulting proto-galaxy disc will form local gravitational instabilities. They argue that once a disc reaches a mass where it is only marginally stable, structures will form in the disc. These structures will act to transport angular momentum outwards while forming clumps which can travel inwards. The mass that travels inwards will go towards forming a $\sim 10^5\,{\rm M}_\odot$ central object. Ultimately, in the right conditions, this process allows the disc to regulate its density and prevents further fragmentation and suppresses star formation. Lodato & Natarajan (2006) do assume isothermal halo density profiles, though the authors argue a more realistic, NFW profile (Navarro et al. 1997) will not change the outcome of their simulations. An NFW profile halo may result in the disc dominating the gravitational potential in its innermost region, leading to the formation of bar instabilities. However, they argue the global instabilities will

only enhance the accretion rate in the inner disc and ultimately will not change the resulting black hole seed mass.

Cosmological hydrodynamic simulations investigating the idealised collapse of gas in atomic cooling haloes indicate that supersonic turbulent motions of the collapsing gas can remove $\gtrsim 90\%$ of the angular momentum (Regan & Haehnelt 2009). This results in very high inflow rates ($\sim 1\,\mathrm{M}_\odot\,\mathrm{yr}^{-1}$) which are sufficient for the formation of $M_\bullet \sim 10^5\,\mathrm{M}_\odot$ black hole seeds (Regan & Haehnelt 2009).

Models of SMS formation have shown that the required massive proto-stellar core can only form in metal-free haloes through rapid collapse, where the rate of gas infall onto the forming core is greater than a critical value of $\dot{M}_{\mathrm{in,\,c}} \sim 0.04\mathrm{M}_\odot\,\mathrm{yr}^{-1}$ (Schleicher et al. 2013; Hosokawa et al. 2013; Umeda et al. 2016). At infall rates of $\dot{M}_{\mathrm{in}} > \dot{M}_{\mathrm{in,\,c}}$, the UV radiation from these cores is unable to halt the gas inflow, allowing accretion to continue (Sakurai et al. 2015; Hosokawa et al. 2016). Indeed, recent work by Wise et al. (2019) has indicated that a super-critical infall rate is all that is required for DCBH formation to occur. However, this does not take into account possible fragmentation of the infalling gas within the radius where the infall rate is at the critical value, close to the forming massive proto-stellar core.

1.1.6 Comparison of black hole seeds

The left panel of Figure 1.3 shows what fraction of the Eddington growth rate a black hole would be required to maintain to reach a mass of $M_\bullet = 10^9\,\mathrm{M}_\odot$ at $z = 6$, as a function of black hole mass and redshift. The right panel shows the same but for the case of J1342+0928 which has a black hole mass of $M_\bullet = 8 \times 10^8\,\mathrm{M}_\odot$ at $z = 7.54$, providing a tighter constraint on the evolution of its progenitor black hole.

PopIII remnant black holes with masses of $M_\bullet \lesssim 330\mathrm{M}_\odot$ can exist following the formation of the first stars around $z \lesssim 30$ (Heger et al. 2003; Bromm et al. 2009). These black holes would need to accrete constantly at a rate near the Eddington limit from their formation to become super-massive by $z \sim 6$. However, theoretical studies have shown that PopIII remnant black holes struggle to grow at high redshift (Johnson & Bromm 2007; Milosavljević et al. 2009; Alvarez et al. 2009; Smith et al. 2018), limiting their viability as the seeds of SMBHs. In the case of J1342+0928, a PopIII remnant black hole seed growing

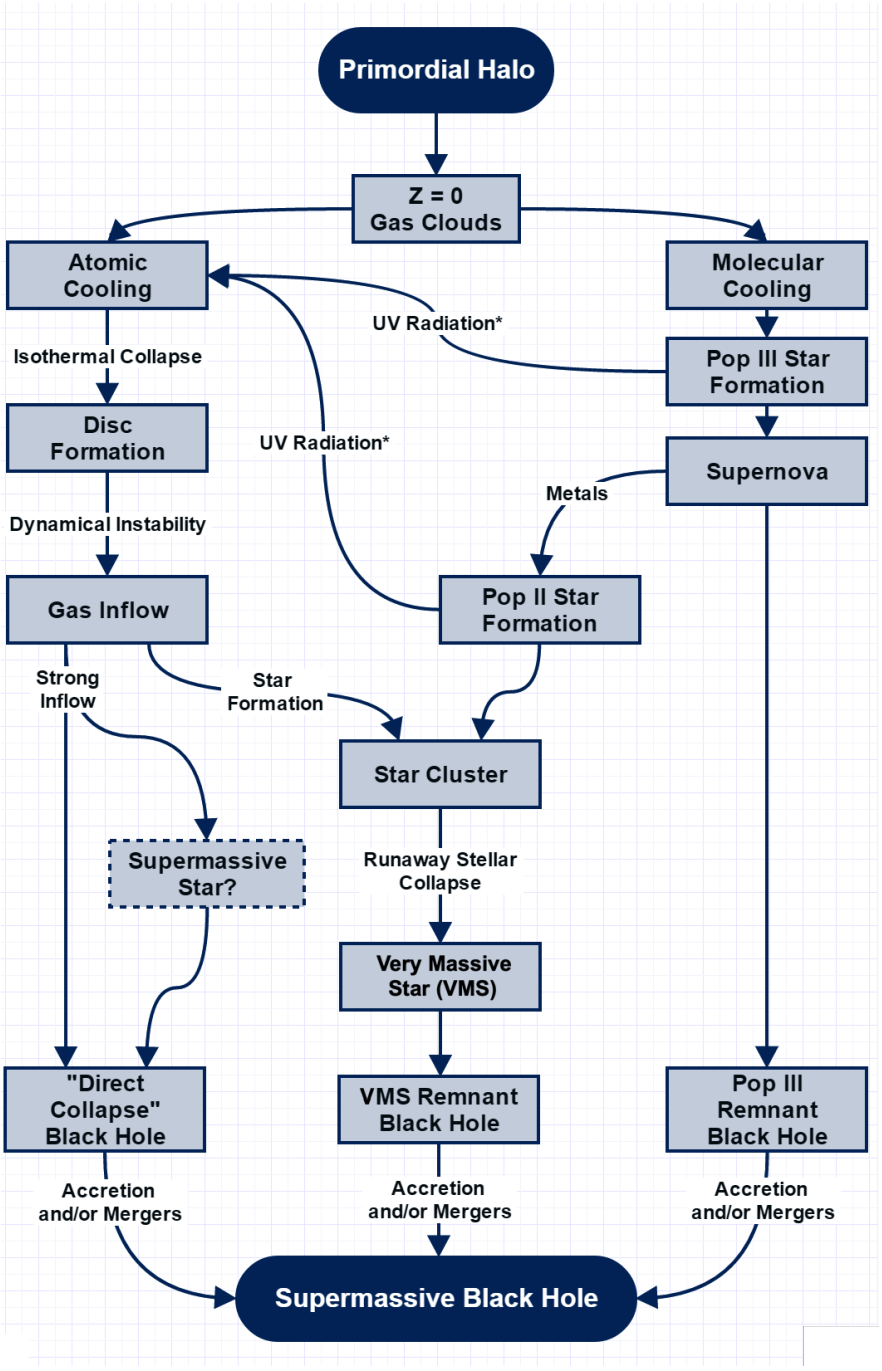

Figure 1.2 *A flow chart, inspired by a similar diagram in Rees (1984), that illustrates the potential formation mechanisms for the seeds of supermassive black holes. *Lyman-Werner photons can dissociate* H_2 *in nearby haloes, leaving atomic hydrogen as the dominant coolant.*

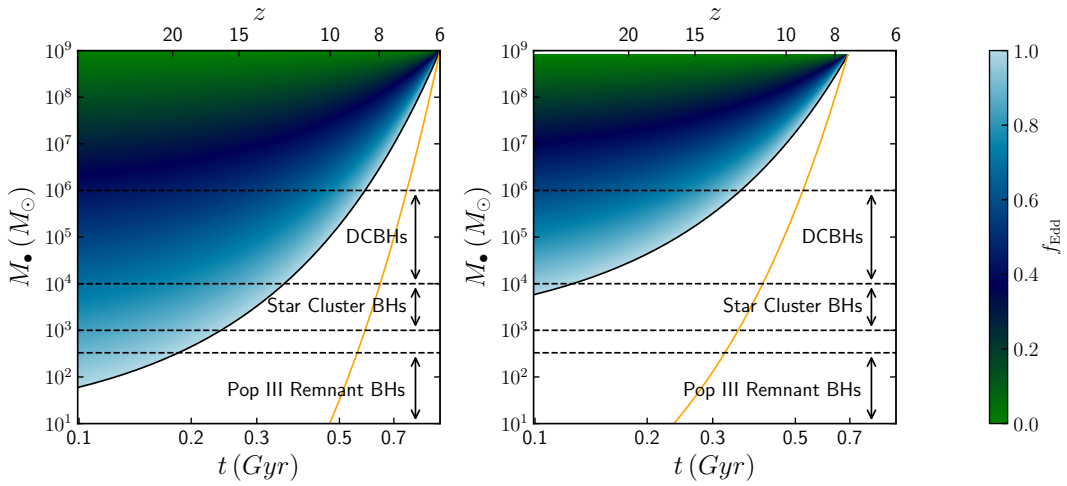

Figure 1.3 *The fraction of the Eddington limit, $f_{\rm Edd}$, required for a black hole with mass $M_\bullet$ at time t to reach $M_\bullet(z = z_{\rm final})$. $M_\bullet = 10^9$ M$_\odot$ at $z_{\rm final} = 6$ for the left panel and $M_\bullet = 8 \times 10^8$ M$_\odot$ at $z_{\rm final} = 7.54$ for the right panel. The black solid line is $f_{\rm Edd} = 1$ and the orange line is $f_{\rm Edd} = 2$*

below the Eddington limit is ruled out as a possible progenitor (see Figure 1.3, right panel), and more massive seeds are required to explain how black holes become super-massive within the first billion years. However, if super-Eddington accretion rates are viable (e.g. Inayoshi et al. 2016), PopIII black holes could still be the seeds of SMBHs.

As discussed above, DCBHs are the most promising candidates for seed black holes as they are the most massive. Note however, even the most massive DCBH seeds need to grow efficiently to reach $M_\bullet \sim 10^9\,{\rm M}_\odot$ by $z \sim 6$. DCBHs forming between $z = 20-10$ are still required to grow by at least three orders of magnitude in mass within ~ 750 Myr, corresponding to a constant Eddington fraction of $f_{\rm Edd} \gtrsim 0.4$. Simulations of accretion onto DCBHs have struggled to reach such a rate when taking feedback from stars and the black hole itself into account (Johnson et al. 2011; Latif et al. 2018). This shows that the growth of black holes is still an unresolved issue, even with the introduction of DCBHs.

1.2 Galaxy formation and evolution at high redshift

To study the evolution of the seeds of SMBHs, such as DCBHs, we need to understand the context in which they evolve and, in turn, study their influence on their environment. With black hole seeds and the first galaxies predicted to be forming concurrently (see, e.g. Bromm & Loeb 2003; Agarwal et al. 2012) within the same hierarchically growing structure, it is important to explore the effect their growth should have on one-another. Indeed, the correlations seen between SMBHs and their host galaxies in the local universe (see, e.g. Kormendy & Ho 2013; Reines & Volonteri 2015; Volonteri & Reines 2016) may yet be hinting at an underlying co-evolution.

1.2.1 The first galaxies

Following the formation of the first stars in the universe at $z \sim 30$ within mini-haloes of only $M \sim 10^6\,\mathrm{M}_\odot$ (see above), the first galaxies began to form. That is not to say that the sites of very first stars directly grew into galaxies. Due to the absence of metal cooling, PopIII stars are predicted to be typically more massive, resulting in stronger feedback (from both strong UV photo-ionizing radiation and stellar winds) when compared to that of higher metallicity stars (Bromm et al. 2009). Any subsequent star formation will effectively be inhibited by the strong feedback from PopIII stars driving all remaining dense gas from the shallow potential well of the mini-haloes in which they form (Kitayama et al. 2004; Whalen et al. 2004; Alvarez et al. 2006). The formation sites of the first galaxies are therefore more likely to be in more massive haloes, capable of holding onto their dense gas and maintaining star formation (Wise & Abel 2007; Greif et al. 2008). Indeed, the first *bona fide* galaxies are unlikely to have only been comprised of PopIII stars and likely had a PopII component (Greif et al. 2010; Maio et al. 2011).

1.2.2 Hierarchical growth and mass assembly downsizing

In standard, ΛCDM cosmology structure forms in a hierarchical fashion (White & Rees 1978; Peacock 1999); over-densities in the cosmic microwave background

(CMB) grow and condense to form dark matter haloes which then grow through accretion and merging to form more and more massive haloes. With galaxies forming out of the baryons which trace the distribution of dark matter haloes (Blumenthal et al. 1984), one might expect the first galaxies to be the basic building blocks of further galaxy growth. However, different observations have revealed that the star formation histories of galaxies are more nuanced.

The total mass of galaxies does grow over cosmic time, supporting the hierarchical formation of galaxies (Madau & Dickinson 2014). The growth in the comoving number density of massive galaxies begins to slow significantly at redshifts below $z \sim 2$ while the comoving number density of lower mass galaxies grows more rapidly, indicating that the majority of massive galaxies assembled at earlier times and lower mass galaxies continued to form at later times and over longer timescales (Marchesini et al. 2009; Moustakas et al. 2013; Muzzin et al. 2013). This is often referred to as "downsizing" which describes the phenomenon of the primary sites of star formation changing from the high-redshift progenitors of massive low-redshift galaxies to low mass galaxies over cosmic time. The drop in the growing number of massive galaxies can be somewhat explained if we consider the drop in the number of mergers at lower redshifts as the universe expands.

1.2.3 Star formation

Star formation is the main driver of galaxy evolution. Other than simply being the process by which the gas content of galaxies is converted into stellar mass, it also governs the properties of the interstellar medium (ISM) and can even influence the density profile of dark matter haloes (Navarro et al. 1996; Pontzen & Governato 2012; Oñorbe et al. 2015). Generations of stars lead to the metal enrichment of the ISM, while heating and galactic outflows are brought about through stellar winds and supernovae feedback effects. The rate at which gas is converted into stars is therefore a critical property of a galaxy.

For some time the star formation rate was thought to vary with the gas density (Schmidt 1959). Kennicutt (1998) observed how the star formation rate surface density, $\dot{\Sigma}_\star$, in local disc galaxies varies with the gas surface density, Σ_g with the functional form:

$$\dot{\Sigma}_\star = A \left(\frac{\Sigma_\mathrm{g}}{1 \mathrm{M}_\odot \, \mathrm{pc}^{-2}} \right)^b \mathrm{M}_\odot \, \mathrm{yr}^{-1} \, \mathrm{kpc}^{-2} \tag{1.9}$$

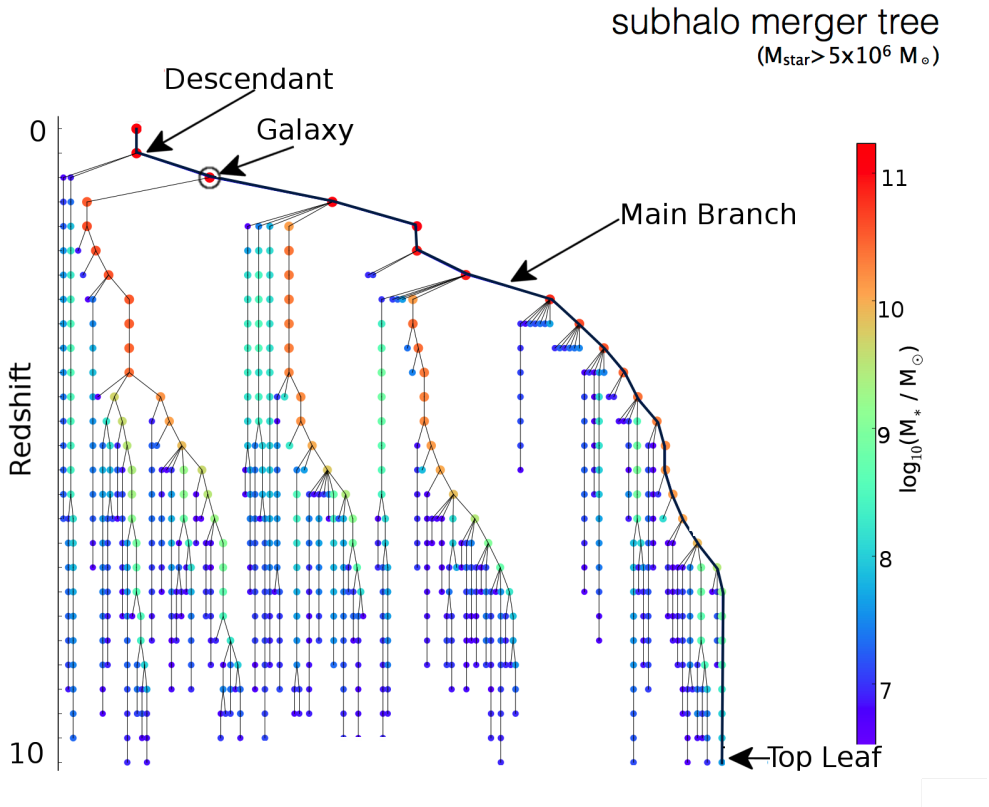

Figure 1.4 *A merger tree from the main EAGLE simulation, showing the hierarchical growth of structure in ΛCDM. This plot is adapted from McAlpine et al. (2016).*

with $b = 1.4 \pm 0.15$ and $A = (2.5 \pm 0.7) \times 10^{-4}$. Equation 1.9 is known as the Schmidt-Kennicutt relation and it describes how efficiently gas can be turned into stars. It is not a physical law in the usual sense as it is purely empirical, however, in part due to its universality (see, Kennicutt & Evans 2012), it has become the standard to refer to the Schmidt-Kennicutt relation as the star formation "law".

There is not a complete consensus in the community as to the physical mechanism behind the star formation law. It is generally accepted that the Schmidt-Kennicutt relation comes from the timescale over which star formation occurs, $t_{\rm sf}$ scaling with the local dynamical time (Silk 1997).

$$\dot{\Sigma}_{\star} = \frac{\Sigma_{\rm g}}{t_{\rm sf}} \propto \frac{\Sigma_{\rm g}}{t_{\rm dyn}} \propto \Sigma_{\rm g}^{1.5} \tag{1.10}$$

However, the physics behind the star formation efficiency ($\varepsilon = t_{\rm dyn}/t_{\rm sf}$) is not fully understood. ε encapsulates all of the physical processes acting against the gravitational collapse of molecular gas clouds to form stars, such as, the thermal energy of the gas clouds, magnetic fields and turbulence (see, e.g. Klessen & Hennebelle 2010). The star formation efficiency in a dynamical time is roughly constant over a variety of scales such that $\varepsilon \sim 0.01$ (Krumholz & Tan 2007).

Star formation can only occur where there is sufficient cold gas. The gas density has to be above a certain threshold for star formation to occur, $\Sigma_{\rm Thres} \sim 10\,{\rm M}_{\odot}\,{\rm pc}^{-2}$ (see, e.g. Schaye 2004; Schaye et al. 2010). For a cloud to undergo gravitational collapse and begin to form stars it must be massive enough to be susceptible to the Jeans instability, i.e. the cloud mass is such that gravity can overcome all forms of pressure support. This critical mass is known as the Jeans mass. In the absence of magnetic fields, the Jeans mass of a non-rotating cloud is a function of its density, ρ, and gas temperature, $T_{\rm gas}$. For a spherical, atomic gas cloud with uniform temperature and density the Jeans mass becomes,

$$M_{\rm J} = \left(\frac{5k_{\rm B}T_{\rm gas}}{G\mu m_{\rm H}}\right)^{3/2} \left(\frac{3}{4\pi\rho}\right)^{1/2} \propto T_{\rm gas}^{3/2}\mu^{-3/2}\rho^{-1/2} \tag{1.11}$$

where μ is the mean molecular weight, $k_{\rm B}$ is the Boltzmann constant and $m_{\rm H}$ is the mass of a hydrogen atom. Increasing the temperature of the cloud, increases the Jeans mass, i.e. the minimum mass required for the cloud to collapse increases. When the mass of the gas cloud is such that, $M_{\rm cloud} > M_{\rm J}$, the cloud will fragment and to first order the number of fragments formed should be roughly

$N \sim M_{\rm cloud}/M_{\rm J}$.

1.2.4 Disc instabilities

The gravitational stability of a disc is an indicator of the extent to which the disc is susceptible to disruptions through perturbations. A perturbation could represent a variety of different physical processes depending on the scenario. When considering a (proto-)galactic disc, this could be, for example, a tidal interaction event with an external mass or an perturbation in the disc itself, such a spiral arm or an orbiting massive black hole.

If we consider axis symmetric perturbations acting on a gaseous disc, the dispersion relation is given by (Toomre 1964; Wang & Silk 1994),

$$\omega_{\rm g}^2 = \kappa^2 + k^2\sigma_{\rm g}^2 - 2\pi G k \Sigma_{\rm g} \tag{1.12}$$

where $\omega_{\rm g}$ and k are the perturbation growth rate and wavenumber respectively. κ is the epicyclic frequency in the disc, $\sigma_{\rm g}$ is the velocity dispersion in the disc and is usually defined as the sound speed in a gaseous disc, $\sigma_{\rm g} = c_{\rm s}$ (see, e.g. Stark et al. 2018). $\Sigma_{\rm g}$ is the surface density of the gas. If $\omega_{\rm g}^2 < 0$ then the instability will grow. The first term in Equation 1.12, κ^2, represents the rotational support term while the second term, $k^2\sigma_{\rm g}^2$, is the thermal support. The final term is negative, as rather than support against the growth of instabilities, it is this gravitational term that drives the growth. One can see that $\omega_{\rm g}^2 < 0$ will be true if the following holds:

$$Q_{\rm g} \equiv \frac{\kappa\sigma_{\rm g}}{\pi G \Sigma_{\rm g}} < 1 \tag{1.13}$$

This is the stability parameter first described by Toomre (1964), which is used to identify whether a disc is stable to the development of gravitational instabilities. Romeo & Wiegert (2011) showed how the Toomre stability parameter of both stellar and gas disc components can be combined to find the full Toomre

parameter, $Q_{\rm Toomre}$, using the following:

$$Q_{\rm Toomre} = \begin{cases} \left(\frac{W}{Q_{\rm g}} + \frac{1}{Q_\star}\right)^{-1} & Q_{\rm g} \geq Q_\star \\ \left(\frac{1}{Q_{\rm g}} + \frac{W}{Q_\star}\right)^{-1} & Q_\star \geq Q_{\rm g} \end{cases} \tag{1.14}$$

where $W = 2\sigma_{\rm g}\sigma_\star/(\sigma_{\rm g}^2 + \sigma_\star^2)$. In the case where $\sigma_{\rm g} = \sigma_\star$, $W = 1$ and the full Toomre stability parameter becomes simply:

$$Q_{\rm Toomre} = \frac{\kappa\sigma}{\pi G\Sigma} \tag{1.15}$$

where $\Sigma = \Sigma_{\rm g} + \Sigma_\star$ and $\sigma = \sigma_\star = \sigma_{\rm g}$.

As I will discuss in Chapter 2, Wang & Silk (1994) showed how the Toomre stability parameter can be related to the star formation rate by assuming the star formation rate within an unstable disc is a function of the growth rate of gravitational instabilities, ω (cf. Schaye 2004). $Q_{\rm Toomre}$ has also been used to calculate gravitational instability driven viscosity and inflow rates within gravitationally unstable discs (Lin & Pringle 1987; Lodato 2007; Devecchi et al. 2010).

1.2.5 Black hole growth

A black hole can gain mass through the accretion of gas and stars or through merging with other black holes. For substantial growth to occur over a short timescale (such as that required to form SMBHs by $z \sim 6$) through black hole mergers, a high frequency of merging events is need. For example, a PopIII remnant black hole formed at $z = 30$ with a mass of $M_\bullet = 330\,{\rm M}_\odot$ would have to undergo ~ 22 equal-mass mergers to reach $M_\bullet = 10^9\,{\rm M}_\odot$ by $z = 6$. The expected distribution of seed black holes indicate that an individual black hole will experience an insignificant number of mergers prior to $z \sim 6$ (Johnson et al. 2013).

Growth through accretion has a greater potential for providing the necessary increase in mass. However, accretion is still limited by the supply of gas to the black hole as well as the rate and efficiency at which a black hole can accrete (e.g. the Eddington limit discussed above). For gas to be available to the black hole

and feed its accretion disc, it has to reach the gravitational sphere of influence of the black hole. This requires gas to lose angular momentum and travel inwards through some torque. I will discuss this in more detail in Chapter 3.

Once the gas is within the gravitational influence of the black hole, the retained angular momentum forces the gas into an accretion disc (Lynden-Bell 1969; Gurzadian & Ozernoi 1979). This disc feeds the black hole with friction from turbulent motions within the disc acting as a torque, driving the transport of mass inwards and angular momentum outwards. The disc is not self-gravitating as on this scale ($R \lesssim 1 - 10$ pc) the black hole dominates the gravitational potential. As gas within the disc approaches the black hole the change in potential energy is converted into kinetic energy raising the velocity dispersion and increasing friction. The friction in the disc leads to the release of energy through radiation. The accretion discs around SMBHs emit powerful UV and X-ray radiation which has a feedback effect on the surround medium, potentially limiting the inflow of gas and the resulting growth rate (see, e.g. Johnson et al. 2011).

The standard approach used in simulations to model accretion below resolution limits, referred to as Bondi-Hoyle accretion, models the spherical accretion of gas onto the black hole (Hoyle & Lyttleton 1941; Bondi & Hoyle 1944; Bondi 1952; Edgar 2004). In this model, the accretion rate onto the black hole is a function of the mass of the black hole, $M_\bullet$, along with the gas density, ρ_∞, sound speed, c_s, and the relative velocity of the gas and the black hole v_∞.

$$\dot{M}_\mathrm{Bondi} = \frac{4\pi \left(GM_\bullet\right)^2 \rho_\infty}{\left(c_\mathrm{s}^2 + v_\infty^2\right)^{3/2}} \tag{1.16}$$

In simulations, the growth of the black hole has commonly been modelled using the rate from Equation 1.16, with an upper limit of the Eddington rate (Equation 1.3). However, a boosting factor of $\sim 100 - 1000$ is often required to match the growth rate inferred from observations.

1.2.6 Galaxy-black hole relations and co-evolution

As black hole growth and star formation both rely on a plentiful supply of gas the two processes are in direct competition. Black hole accretion and star formation can also directly impact one-another through feedback heat gas and driving outflows (see, e.g. Schawinski et al. 2006; Latif et al. 2018). As the main

drivers of galaxy evolution, understanding the interaction of these processes as both the galaxy and its massive black hole evolve is important to understanding galaxy evolution as a whole.

The results of SDSS (the Sloan Digital Sky Survey) have helped reveal the apparent bi-modality of the population of galaxies out to redshifts around $z \lesssim 3$ (see, e.g. Baldry et al. 2004; Muzzin et al. 2013; Willett et al. 2013), with galaxies generally existing in either the "blue cloud" of star forming galaxies or on the "red sequence" of quenched galaxies (so-called because of their respective positions in the colour-magnitude diagram). The comoving number and mass density of the two populations following opposite trends over cosmic time, with the quiescent, red galaxies becoming more popular over time (Muzzin et al. 2013). The red population generally have older stellar populations (Kauffmann et al. 2003) and as the star forming galaxies are, by definition, growing in stellar mass over time, this implies that the blue population are becoming quenched and joining the red sequence once they have grown (Schawinski et al. 2014, see, e.g.). Possibly the most popular explanation for this quenching in the most massive galaxies is through the heating and expulsion of gas via the energetic feedback from the AGN within these galaxies (Di Matteo et al. 2005; Schawinski et al. 2007; Fabian 2012; Trayford et al. 2016; Correa et al. 2019).

Observations of the local universe have revealed correlations between black holes and the larger scale properties of their host galaxies, possibly hinting at a co-evolution (Kormendy & Ho 2013; McConnell & Ma 2013; Heckman & Best 2014). The observed correlation between the mass of a galaxy's SMBH, $M_\bullet$, and the stellar velocity dispersion, σ, in the stellar bulge (known as the $M - \sigma$ relation, Ferrarese & Merritt 2000; Gebhardt et al. 2000), historically gave the first clues on a feedback driven co-evolution of black holes and their host galaxies (Silk & Rees 1998; King 2003).

Another hint of co-evolution is found when comparing SMBH masses with the stellar masses of their host galaxies (Kormendy & Ho 2013). Though the correlation is not tight, Reines & Volonteri (2015) find the following trend between the masses inferred from local AGN and their host's stellar mass (with a rms deviation of 0.55 dex in black hole mass):

$$\log_{10}\left(M_\bullet/M_\odot\right) = \alpha + \beta \log_{10}\left(M_\star/10^{11} M_\odot\right) \tag{1.17}$$

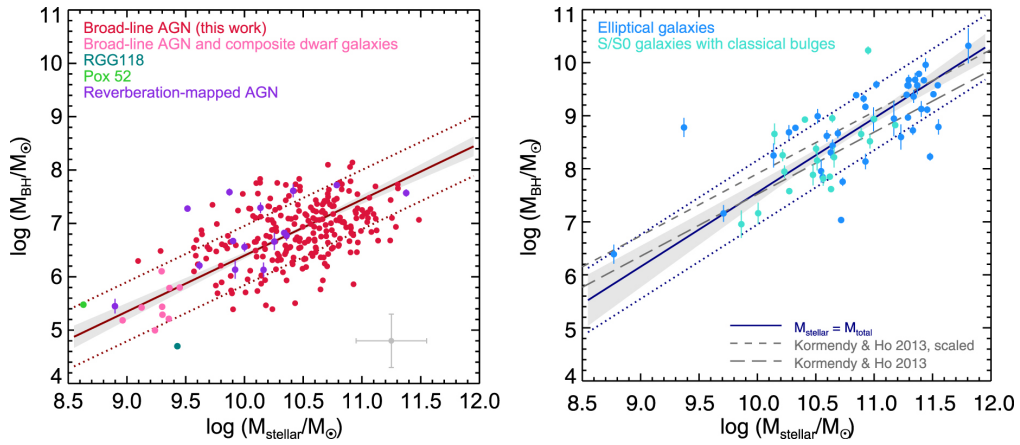

Figure 1.5 *Taken from Reines & Volonteri (2015) Figure 10: "Left: the black-hole-to-total stellar mass relation for local AGNs (dark red line; [Equation 1.17, case 1]). The light gray shaded region accounts for the errors in the slope and intercept of the relation, and the dark red dotted lines indicate the rms scatter of points around the relation (0.55 dex). The gray error bar indicates uncertainties in stellar masses for all points, and single-epoch spectroscopic black hole masses. Black hole mass errors for the reverberation-mapped AGNs are shown on the (purple) data points. Right: same as the left panel, but for the inactive sample of elliptical galaxies and spiral/S0 galaxies with classical bulges ([Equation 1.17, case 2]). The dark blue line indicates our relation derived using total stellar mass."*

where $\alpha = 7.45 \pm 0.08$ and $\beta = 1.05 \pm 0.11$ (case 1, see left panel of Figure 1.5). Reines & Volonteri (2015) note that this relation is flatter than the relations found from the stronger correlation observed when focusing only on stellar bulges (Magorrian et al. 1998; Häring & Rix 2004) or elliptical galaxies (Kormendy & Ho 2013). When focusing on only the elliptical or bulge-dominated galaxies in their sample, they find a steeper correlation ($\alpha = 8.95 \pm 0.09$, $\beta = 1.40 \pm 0.21$; case 2, see right panel of Figure 1.5) than either their local AGN sample or those found in previous work (Häring & Rix 2004; Kormendy & Ho 2013; McConnell & Ma 2013).

1.3 This thesis

In this thesis I explore the consequences of direct collapse black hole formation on galaxy formation and evolution. From this I predict how these consequences should manifest in the galaxies of the early universe, providing a hypothesis to be tested with the next generation of observational studies.

In Chapter 2 I introduce an analytic model of a growing, isolated proto-galactic disc and massive black hole system. I use my model to investigate the consequences of seeding SMBHs with DCBHs on proto-galactic disc evolution by studying the impact the massive seed has on the development of gravitational disc instabilities. This work has been published as Eastwood & Khochfar (2018).

Chapter 3 explores capability of the inflow of gas from gravitational-unstable discs to feed the growth of the massive seed black holes to SMBHs by $z \sim 6$, in the absence of environmental effects such as galaxy mergers. To do this I develop the analytic model further to include an estimate for the viscosity driven inflow of gas through the disc to feed the growth of the massive black hole. This work has been submitted for publication and has undergone revisions through the peer review process.

In Chapter 4, I investigate the infall of massive black holes into the haloes of their eventual host galaxies. With the aim of testing the potential of this process to heat gas within the halo, I model the torque acting on the black hole from dynamical friction which drives the infall, calculating infall timescales and the energy released throughout the process.

Finally, in Chapter 5 I wrap-up with the main conclusions of my work and I

Table 1.1 *Table of acronyms.*

Acronym	Full form
SMBH	Super-massive black hole
DCBH	Direct collapse black hole
AGN	Active galactic nucleus
VMS	Very massive star
SMS	Super massive star
UV	Ultra-violet
LW	Lyman-Werner
CMB	Cosmic microwave background
SFR	Star formation rate
sSFR	Specific star formation rate
ΛCDM	Lambda cold dark matter

discuss possible future steps for my research.

Throughout this work a ΛCDM Universe is assumed with the following cosmological parameters unless otherwise stated: $\mathrm{H}_0 = 70\,\mathrm{km\,s^{-1}\,Mpc^{-1}}$, $\Omega_{\mathrm{m},0} = 0.27$ and $\Omega_{\Lambda,0} = 0.73$.

Chapter 2

How black holes stop their host galaxy from growing without AGN feedback

This chapter is composed of a paper published in MNRAS (Eastwood & Khochfar 2018). Revisions have been made as requested by the allocated peer during the review process.

2.1 Introduction

The relationship between super-massive black holes (SMBHs) and their host galaxies is an active area of research (see, e.g. Kormendy & Ho 2013; Hickox et al. 2014; Delvecchio et al. 2015; Bongiorno et al. 2016; Yang et al. 2018). Several empirical correlations between the mass of a black hole (black hole) and the physical properties of its host galaxy have been reported (e.g. Magorrian et al. 1998; Merloni et al. 2003; Merritt 2006; Kormendy & Bender 2009). Of these correlations the black hole mass-stellar velocity dispersion (the $M_\bullet - \sigma$ relation) (e.g Ferrarese & Merritt 2000; Gebhardt et al. 2000; McConnell et al. 2011) historically gave the first clues on a feedback driven co-evolution of black holes and their host galaxies (Silk & Rees 1998; King 2003).

Theoretical and observational studies suggest that major mergers play a fundamental role in establishing feedback and feeding cycles (e.g. Di Matteo et al. 2005;

Hopkins et al. 2006; Kormendy et al. 2011). Further support for the importance of mergers comes from the increased scatter in the black hole-host correlations at larger redshifts which is a natural consequence of the central-limit theorem and an increasing number of black hole mergers for SMBH toward low redshifts (Schawinski et al. 2006; Peng et al. 2006; Hirschmann et al. 2010). However, mergers are not the only physical processes involved; offsets in the $\mathrm{M}_{\bullet} - \mathrm{M}_{\mathrm{Bulge}}$ relation corresponding to disc galaxies can be explained through the co-evolution of SMBHs with their disc-galaxy hosts through secular processes (Volonteri et al. 2016; Simmons et al. 2017; Martin et al. 2018).

SMBHs with masses of $M_{\bullet} \sim 10^9\,\mathrm{M}_{\odot}$ have been observed in galaxies at high redshifts ($z \sim 6$ – 7) (Fan et al. 2006; Mortlock et al. 2011; Bañados et al. 2018) corresponding to less than a gigayear after The Big Bang. This population of black holes must have had a rapid formation process to reach the masses observed at this early epoch. Indeed, if the growth rate of SMBHs is limited by the Eddington accretion rate (see however, Natarajan & Volonteri 2012; Pacucci et al. 2017), they must be seeded by some massive progenitor at an early epoch $z \geq 10$, prior to the onset of reionization and the shutdown of Population-III stars (Paardekooper et al. 2015; Johnson et al. 2013).

Given the e-folding nature of an Eddington limited black hole-growth rate on a Salpeter time scale of $t_{\mathrm{Sal}} = 0.45\,\eta/(1-\eta)$ Gyr (where $\eta \sim 0.1$ is the radiative efficiency (see, e.g. King et al. 2008)), varying the initial seed mass by factors of ten can have a strong impact on relaxing the constraints on the formation time in the early Universe. Consequently, various seed formation processes are discussed (see, e.g. for a review Volonteri 2010), including population III stellar remnants (Madau & Rees 2001) and the collapse of dense stellar clusters (Clark et al. 2008; Yajima & Khochfar 2016) or the direct collapse of gas through the state of a super-massive star (Bromm & Loeb 2003; Lodato & Natarajan 2006; Begelman et al. 2006; Begelman 2010; Agarwal et al. 2012). The latter channel has received heightened attention due to the massive seeds it produces and the ability to grow to super-massive scales with less stringent constraints on the average accretion rate (Agarwal et al. 2012; Latif et al. 2013, 2014; Pacucci et al. 2015; Agarwal et al. 2016b). [1]

Direct collapse black holes (DCBHs) form during the collapse of pristine gas in

[1] Johnson et al. (2011) simulated the radiative feedback from such a seed black hole showing that the average accretion rate is very low, indicating that the feedback might off-set the advantage you gain of having a higher initial mass.

haloes with virial temperatures of $T_{\rm v} \gtrsim 10^4$ K (Bromm & Loeb 2003). Provided a halo remains pristine and the local intensity of the Lyman-Werner radiation field is greater than the critical intensity required to dissociate any H_2 gas (Agarwal et al. 2016a), cooling within the halo will only take place via atomic hydrogen. The gas temperature in such a halo will be kept at $T_{\rm g} \sim 10^4$ K during collapse with a Jeans Mass of $M_{\rm J} \sim 10^6\,{\rm M}_\odot$; preventing the fragmentation into gas clumps and stars, and leading to the isothermal collapse of a massive gas cloud into a single black hole (Bromm & Loeb 2003), possibly via an intermediate stage of a super-massive star (Begelman 2010). This process results in the formation of massive seed black holes with masses of $M_\bullet \sim 10^4 - 10^6\,{\rm M}_\odot$ at $z \sim 10-20$, prior to the formation of the host galaxy in the halo (Agarwal et al. 2012). If SMBHs are truly seeded by DCBHs it would affect the early stages of galaxy evolution. Gas build up around the gravitational potential well of a DCBH through cosmological accretion and halo merging, would not only lead to further black hole growth but also potentially to the gradual growth of a proto-galaxy around the black hole. Besides feedback from the black hole affecting the proto-galaxy, initially such a proto-galaxy would be gravitationally dominated by the mass of the black hole as well. However, it is not clear how this would affect the processes of galaxy evolution, such as star formation, and the cycle of baryons in the galaxy.

Recently, a first potential candidate for an observed DCBH system has been proposed (Sobral et al. 2015; but see Bowler et al. 2017). The system, called CR7, is a very bright Ly α emitter at $z = 6.6$ with $L_{{\rm Ly}\alpha} \sim 10^{44}{\rm erg\,s^{-1}}$ (Matthee et al. 2015; Sobral et al. 2015; Bowler et al. 2017). Sobral et al. (2015) have identified CR7 as a combination of three components: Two clumps which appear to be evolved galaxies in close proximity to a third clump, which provides the vast majority of the Ly α flux. This third clump has been successfully modelled by Agarwal et al. (2016b) as a $M_\bullet \sim 4.4 \times 10^6\,{\rm M}_\odot$ black hole formed through direct collapse around $z \sim 20$. Recent work has shown either an active galactic nucleus (AGN) or a young starburst population are also likely explanations for the observed characteristics of CR7 (Bowler et al. 2017). With the former being potentially seeded via the stage of a DCBH, and the latter not requiring a DCBH at all.

The evolution during the initial stages of a potential DCBH-systems such as CR7 is unknown and yet likely consists of a constant interplay between star formation and black hole growth. The formation of stars in proto-galaxies is driven by the accretion of gas and subsequent gravitational collapse. The star formation

law relating the star formation rate (SFR) surface density in a disc galaxy to its gas surface density (Schmidt 1959), once confirmed by observations of local galaxies (Kennicutt 1998), has more recently been shown to extend to $z \sim 1.5$ (see, e.g. Carilli & Walter 2013). At higher redshifts, the higher densities imply shorter cooling times (as $t_{\rm cool} \propto \rho^{-1}$). Rapid cooling means that the SFR is only limited by the total gas accretion rate and the growth rate of gravitational instabilities in a galaxy (Dekel et al. 2009, 2013). Previous studies on galaxy evolution and star formation have related the global SFR to disc properties via the growth rate of instabilities (Fall & Efstathiou 1980; Lacey & Fall 1983; Wang & Silk 1994; Schaye 2004; Elmegreen & Burkert 2010). For example, Elmegreen & Burkert (2010) modeled the growth in gas mass and turbulence driven by gas accretion onto a galaxy and found the SFR was mainly a function of the gas accretion rate. However, star formation is a local process. Star formation can only take place where the gas is unstable to gravitational collapse (Wang & Silk 1994). In this context the black hole may also play an important role in the stability of the disc (Lodato 2012). The gas properties will change throughout the galaxy with some regions being more unstable than others. Indeed, Schaye (2004) found that if disc galaxies are rotationally supported against collapse this will be particularly at large radii, limiting the radial extent of star formation to within some truncation radius.

A further complicating factor for the growth of proto-galaxies around DCBHs is that the hosting halo is generally in the vicinity of a more massive halo it is likely to merge with at a later stage during its evolution (Agarwal et al. 2014). During the satellite-phase the provision of fuel for star formation will cease due to stripping processes in the environment (van den Bosch et al. 2008). The growth of the host galaxy will thus be affected and in turn the path to the locally observed black hole-galaxy correlations.

The aim of this study is two-fold, to model the stabilising effect of DCBHs on the gaseous disc in proto-galaxies and their impact on the onset of star formation, and to, based on these models, present arguments for the evolution of DCBHs toward locally observed correlations with host galaxies. First, I lay out the star formation model used, which relates star formation rate to disc instabilities (section 2.2). The model is first introduced by discussing a non-evolving case in section 2.3 before being fully explored in section 2.4 with evolving the halo and stellar mass. Finally, I discuss the implications of the model for massive seed hosting galaxies and the onset of star formation within them (section 2.5). Throughout this study

a ΛCDM Universe is assumed with $H_0 = 70 \mathrm{km\,s^{-1}\,Mpc^{-1}}$, $\Omega_{\mathrm{m},0} = 0.27$ and $\Omega_{\Lambda,0} = 0.73$.

2.2 Star formation

The empirical star formation law derived from local observation (Kennicutt 1998),

$$\dot{\Sigma}_{\star}^{\mathrm{KS}}(t) = 1.515 \times 10^{-4}\,\mathrm{M_{\odot}\,yr^{-1}\,kpc^{-2}}\left(\Sigma_{\mathrm{g}}/1\,\mathrm{M_{\odot}\,pc^{-2}}\right)^{1.4} \tag{2.1}$$

where the amplitude has been adjusted to fit with a Chabrier (2003) IMF (Schaye et al. 2010), has been seen to hold to high redshift (see, e.g. Carilli & Walter 2013, and references therein). Furthermore, the relation appears to hold for both local surface density values and those integrated over an aperture (Kennicutt 1998). One can understand this relation between star formation rate surface density and gas density using a star formation timescale (see, e.g. Wang & Silk 1994; Kennicutt 1998; Krumholz & Tan 2007; Elmegreen & Burkert 2010). The local dynamical or free-fall time within a star forming region is often used to relate the timescale to the gas density while the different mechanisms that would work against gravitational collapse, such as thermal and rotational support, are factored in either explicitly (Wang & Silk 1994; Elmegreen & Burkert 2010) or as part of an efficiency parameter (Krumholz & Tan 2007).

In contrast to global models of star formation in proto-galactic discs (e.g. Elmegreen & Burkert 2010), the focus here is on the radial star formation profile, which depends on local gravitational instabilities in the disc and allows the investigation of the impact of massive seed black holes.

The Ansatz for the star formation model used here is: (1) Star formation can only take place above a minimum threshold $\Sigma_{\mathrm{g}} > \Sigma_{\mathrm{th}} = 10.0\,\mathrm{M_{\odot}\,pc^{-2}}$ (Schaye 2004). (2) No star formation will take place if the disc is locally stabilised against gravitational collapse $Q_{\mathrm{Toomre}} \geq 1$ or (3) if the local density is too low to overcome tidal forces $Q_{\mathrm{tidal}} \geq 1$ (see section 2.3.1).

If these conditions for star formation are met, the SFR surface density is calculated by relating the timescale for star formation to the maximal growth

rate of axisymmetric perturbations, $\omega_{\rm WS}$ (Wang & Silk 1994):

$$t_{\rm SF} = \frac{1}{\omega_{\rm WS}} = \frac{Q_{\rm Toomre}}{\kappa\sqrt{1 - Q^2_{\rm Toomre}}} \tag{2.2}$$

where κ is the epicyclic frequency and $Q_{\rm Toomre}$ is the Toomre disc instability parameter (see section 2.3). The SFR surface density $\dot{\Sigma}_\star$ can then be written as a function of this timescale, the gas surface density profile $\Sigma_{\rm g}$, and the star formation efficiency parameter ϵ, to obtain the following (Wang & Silk 1994):

$$\begin{aligned} \dot{\Sigma}^{\rm WS}_\star(t) = \epsilon\frac{\Sigma_{\rm g}}{t_{\rm SF}} &= \epsilon\frac{\kappa}{Q_{\rm Toomre}}\Sigma_{\rm g}\left(1 - Q^2_{\rm Toomre}\right)^{0.5} \\ &= \epsilon\frac{\pi G\Sigma_{\rm d}}{\sigma}\Sigma_{\rm g}\left(1 - Q^2_{\rm Toomre}\right)^{0.5} \end{aligned} \tag{2.3}$$

where σ is the velocity dispersion (from here on taken to be the sound speed, c_s) and the $\Sigma_{\rm d} = \Sigma_{\rm g} + \Sigma_\star$ is the total surface density of the disc. This formulation includes explicitly the effects of rotation on the growth rate of instabilities in the disc. The rotation of the disc provides support against gravitational instabilities, preventing the collapse of gas to form stars (Fall & Efstathiou 1980; Lacey & Fall 1983). This then relates the SFR to the growth rate of gravitational instabilities rather than simply the free-fall timescale and allows one to take the structure of the disc in to account. [2]

2.3 Non-evolving, non-star forming case

2.3.1 Model setup

This first case looks at the effect of the black hole in a non-evolving gaseous disc (The fully evolving case is addressed in section 2.4). The mass of the halo is kept constant, $\dot{M}_{200} = 0$, and the stellar mass is zero throughout, $M_\star = 0$. To investigate the effects of a seed black hole on a galaxy forming in its host halo it is necessary to probe the inner region of the proto-galactic disc. For this reason we take the radial dependencies of system's properties into account. For the

[2] Equation 2.3 will result in a steeper $\dot{\Sigma}_\star - \Sigma_{\rm g}$ relation ($\dot{\Sigma}_\star \propto \Sigma^2_{\rm g}$) than the Kennicutt (1998) law (equation 2.1) and is therefore likely to overestimate the total SFR, providing a conservative, upper-limit estimate for the model SFR in this study.

non-evolving case we have a purely gaseous disc embedded in a halo we model simply as an isothermal sphere. We assume the gas disc has an exponential profile centred on the black hole such that the surface density of gas goes with radius as,

$$\Sigma_{\rm g}(R) = \Sigma_{g,\,0}\exp(-R/R_{\rm d}) \tag{2.4}$$

$R_{\rm d}$ is the disc scale radius which is set by the halo parameters and $\Sigma_{g,\,0} = M_{\rm g}/(2\pi R_{\rm d}^2)$. The halo is assumed to be an isothermal sphere, giving the following for the disc scale radius (Mo et al. 1998):

$$R_{\rm d} = \frac{1}{\sqrt{2}}\left(\frac{j_{\rm d}}{m_{\rm d}}\right)\lambda\, r_{200} \tag{2.5}$$

Throughout this study $j_{\rm d}/m_{\rm d}$ is assumed to be unity and the spin parameter is taken from the log-normal distribution used by Mo et al. (1998) with the first and second moments: $\bar{\lambda} = 0.05$ and σ_λ respectively. For simplicity the first moment of the distribution is used as a fiducial value for λ unless otherwise stated, though it is important to note changing λ will have an effect on the model. For example, taking λ at the 10% point of the distribution roughly halves the disc scale radius which, for the same disc mass, doubles the surface density, $\Sigma_{g,\,0}$. For further discussion in the context of the model see Appendix 2.6.

The local stability of the disc against gravitational collapse is parametrised by the Toomre stability parameter (Toomre 1964). If we have a disc which has both a stellar and gas component and assume the velocity dispersion of each component is such that $\sigma \equiv \sigma_{\rm g} = \sigma_{\rm s}$, the Toomre parameter becomes:

$$Q_{\rm Toomre} = \frac{\kappa\,\sigma}{\pi\,G\,\Sigma_{\rm d}} \tag{2.6}$$

where κ is the epicyclic frequency and σ is the velocity dispersion (Toomre 1964; Wang & Silk 1994; Romeo & Wiegert 2011). If $Q_{\rm Toomre} > 1$ the disc is stable to gravitational instabilities; $Q_{\rm Toomre} < 1$ the disc is unstable and $Q_{\rm Toomre} \sim 1$ the disc is partially stable (see, e.g. Lodato 2007). The velocity dispersion is taken as the sound speed of the gas, $c_{\rm s}$. This acts as a lower limit as turbulent motions are not taken into account, however at $T_{\rm g} = 8000$ K, the sound speed

should provide a significant fraction of the gas velocity dispersion[3]. The epicyclic frequency describes the rotational support of the system due to the gravitational potential. It can be expressed as a function of the angular velocity, $\Omega = V_{\rm c}/R$ (where V_c is the circular velocity which is calculated from the radial derivative of the gravitational potential):

$$\kappa^2 = \frac{2\,\Omega}{R}\frac{d}{dR}(R^2\Omega) \tag{2.7}$$

This is therefore a function of the three components of the system: the halo, disc and black hole. As the potential due to these components can be combined to find the full potential, κ can be split into the corresponding parts. The relative importance of the component of κ due to the black hole will increase with proximity to the black hole.

Similarly to the Toomre parameter, the critical tidal density, $\rho_{\rm tidal}$, defines the limit to the local density of the disc below which the local self gravity of the disc is weak compared to the tidal forces on the disc (Hunter et al. 2001; Martig et al. 2009).

$$\rho_{\rm tidal} = \frac{3\,\Omega\,R}{2\pi G}\left|\frac{d\Omega}{dR}\right| \tag{2.8}$$

Dominant tidal forces inhibit the growth of density perturbations, preventing stars from forming. To compare the tidal and Toomre stability of the disc one must make a comparison between the critical tidal density and the Toomre parameter. The critical tidal surface density can be defined as $\Sigma_{\rm tidal} = 2H\rho_{\rm tidal}$ and using the scale height of the disc, $H = \sigma^2/(\pi\,G\,\Sigma_{\rm d})$, we obtain:

$$\Sigma_{\rm tidal} = 3\Omega R\frac{\sigma^2}{\pi^2 G^2\Sigma_{\rm d}}\left|\frac{d\Omega}{dR}\right|. \tag{2.9}$$

With some rearranging we can see the square root of the ratio of the critical tidal surface density to the local surface density is of a similar form to the Toomre

[3]With $\sigma = c_{\rm s}$, Equation 2.6 is similar to $Q_{\rm Thermal}$ as described recently by Stark et al. (2018)

Table 2.1 *Table of non-evolving, non-star forming model parameters.*

Parameter	Definition	Fiducial
M_{200}	dark matter halo mass ($\mathrm{M}_\odot$)	5×10^8
λ	halo spin parameter	0.05
$j_\mathrm{d}/m_\mathrm{d}$	disc and halo specific momenta ratio	1.0
f_b	baryon fraction	0.17
T_g	gas temperature (K)	8000
z	redshift	10.0

parameter.

$$Q_\mathrm{tidal} \equiv \sqrt{\frac{\Sigma_\mathrm{tidal}}{\Sigma_d}} = \frac{\sigma}{\pi G \Sigma_\mathrm{d}} \sqrt{3\Omega R \left|\frac{d\Omega}{dR}\right|}. = Q_\mathrm{Toomre} \frac{\nu}{\kappa} \tag{2.10}$$

where we define the tidal frequency ν,

$$\nu^2 = 3\Omega R \left|\frac{d\Omega}{dR}\right| \tag{2.11}$$

It follows that Q_tidal will behave similarly to the Toomre parameter; if $Q_\mathrm{tidal} < 1$ it implies $\rho > \rho_\mathrm{tidal}$ and the disc's local self gravity dominates but if $Q_\mathrm{tidal} > 1$, $\rho < \rho_\mathrm{tidal}$ and the disc is locally unstable to tidal forces, and the growth of gravitational instabilities locally in the disc is inhibited. We combine the two stability parameters by defining Q_* as the maximum of the two:

$$Q_* = \max[Q_\mathrm{tidal},\ Q_\mathrm{Toomre}] \tag{2.12}$$

this reduces the conditions for star formation down to two: that the surface density is above the threshold ($\Sigma_\mathrm{g} > \Sigma_\mathrm{th} = 10.0\,\mathrm{M}_\odot\,\mathrm{pc}^{-2}$) and that $Q_* > 1$.

2.3.2 Stability parameters and timescale profiles

For the analysis here I use a fiducial model of an atomic cooling halo at $z \sim 10$ (see Table 2.1). The total mass of the system was calculated for an atomic cooling halo $M_\mathrm{tot} \sim M(T_\mathrm{vir} = 8000\,K)$ (Mo et al. 2010) and the disc mass was calculated by taking the baryonic mass of the halo, $M_\mathrm{d} = f_\mathrm{b} M_\mathrm{tot}$ where $f_\mathrm{b} = 0.17$ is the universal baryon fraction, unless otherwise stated.

Figure 2.1 shows the radial profiles for the Toomre and tidal stability parameters

respectively for the fiducial set-up as summarized in table 2.1. If we first look at the upper panel of Figure 2.1, the increase in κ at small radii due to the presence of the black hole stabilises the inner-most region of the disc, shown by the increase in Q_{Toomre} at small radii. Increasing the black hole mass increases this effect, narrowing the region of the disc where star formation can take place. For a constant disc mass an accreting black hole thus would be able to prevent a larger fraction of the disc from forming stars as it grows in mass. At larger radii the influence of the black hole diminishes and the disc determines the shape of the stability profiles except for cases with the largest black hole masses. After reaching a minimum both of the stability parameters increase as the disc surface density decreases with radius.

The tidal stability parameter profile (the lower panel of Figure 2.1) shows how the black hole also has a strong tidal effect on the disc at small radii. The tidal and Toomre parameter profiles are similar in shape however, the tidal parameter appears to be below the critical value of 1 over a narrower range in radius. This suggests $Q_{\mathrm{tidal}} \leq 1$ is a stricter condition for star formation in the disc within the model than simply $Q_{\mathrm{Toomre}} \leq 1$.

For a constant disc mass the inner critical radius, the inner-most radius where star formation can occur (where both Q_{Toomre} and Q_{tidal} are ≤ 1), increases with black hole mass (Figure 2.2). The inner critical radius, $R_{\mathrm{c,\,in}}$, is smallest when there is no black hole at $R_{\mathrm{c,\,in}} = 27.3\,\mathrm{pc}$ and is $R_{\mathrm{c,\,in}} = 32.3\,\mathrm{pc}$ for $M_\bullet = 10^6\,\mathrm{M}_\odot$. If the black hole mass is increased enough we reach a point where the whole disc becomes stabilised (For example, the yellow $M_\bullet = 10^8\,\mathrm{M}_\odot$ black hole case in Figure 2.1). The point where the disc becomes completely stabilised is represented in Figure 2.2 by the point where the $R_{\mathrm{c,\,in}}$ lines end around $M_\bullet \sim 10^7\,\mathrm{M}_\odot$ which is less than a tenth of the disc mass ($M_{\mathrm{d}} = 1.02 \times 10^8\,\mathrm{M}_\odot$). It can be useful to compare this inner critical radius to the radius of the sphere of influence of the black hole, $R_\bullet$. We calculate this from $M_\bullet$ and the circular velocity profile of the system, $V_c(R)$, using:

$$R_\bullet = \frac{GM_\bullet}{V_c^2} \tag{2.13}$$

Due to the radial dependence of $V_c(R)$ it is necessary to solve Equation 2.13 iteratively such that $V_c = V_c(R_\bullet)$.

As we increase the black hole mass towards this disc-stabilising value, $R_{\mathrm{c,\,in}}$ and $R_{\mathrm{c,\,out}}$ are of the same order as R_{d}, with $R_{\mathrm{c,\,in}}$ roughly 2.5 times $R_\bullet$.

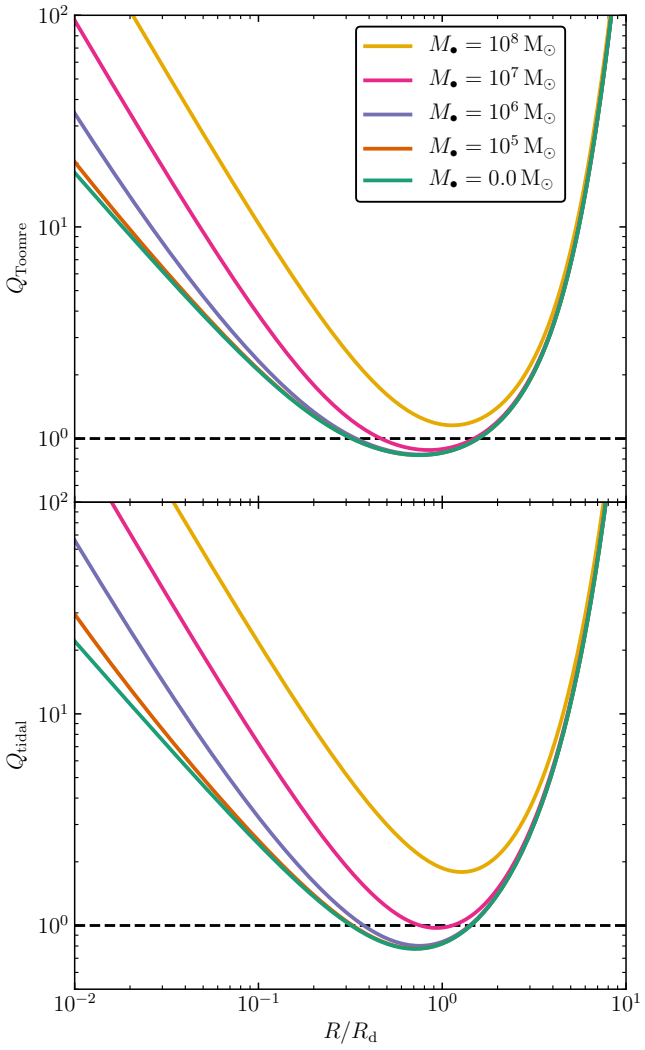

Figure 2.1 *The stability parameters profiles for the same disc without a black hole and for four different mass black holes. The top panel shows the Toomre stability parameter profile and the bottom shows the tidal stability parameter profile. The disc is the same in all cases with* $M_{\mathrm{d}} = 1.02 \times 10^8\,\mathrm{M}_\odot$ *and* $R_{\mathrm{d}} = 86.5\,\mathrm{pc}$.

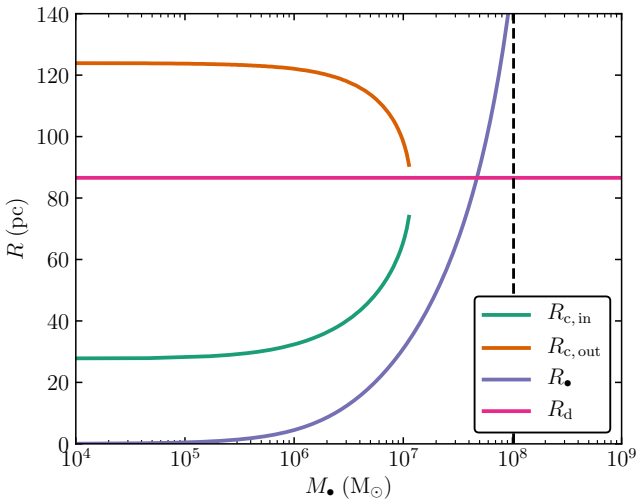

Figure 2.2 *The relationship between characteristic radii versus black hole mass for a disc with $M_d = 1.02 \times 10^8\,M_\odot$ (shown as the vertical, dashed line) and a scale radius of $R_d = 86.5\,pc$. The disc scale radius is shown in pink, the sphere of influence radius of the black hole ($R_\bullet$) is shown in purple, the inner and outer critical radii ($R_{c,\,in}$ and $R_{c,\,out}$) are shown in green and orange respectively. The green and orange lines stop at $M_\bullet \sim 10^7\,M_\odot$, the mass at which the black hole completely stabilises the disc.*

The radius at which either stability parameter is minimized is always of the order of the disc scale radius (see Figure 2.3 and the following section). Starting at black hole mass fractions of 10% the radius at which the tidal stability parameter is minimized quickly catches up with the scale radius of the disc. This helps to explain why $R_{c,\,in}$ approaches R_d as the disc becomes stabilised as we increase the black hole mass.

As the disc approaches stability the minimum value of Q_{tidal} approaches 1 until the black hole mass is sufficiently massive to fully stabilise the disc ($M_\bullet/M_d \sim 10\%$) and $R_{c,\,in} = R_{c,\,out} = R_{Q_{min}}$. At lower black hole masses, the inner critical radius is generally less than the disc scale radius but it can be significantly greater than $R_\bullet$ depending on the masses of the black hole and disc.

2.3.3 Minima of the stability parameter profiles

The radii of the minimum of the two stability parameter profiles as a fraction of the disc scale radius are only a function of the black hole-to-disc mass ratio, the baryon fraction and the spin parameter of the halo (Assuming $j_d/m_d = 1$). Each

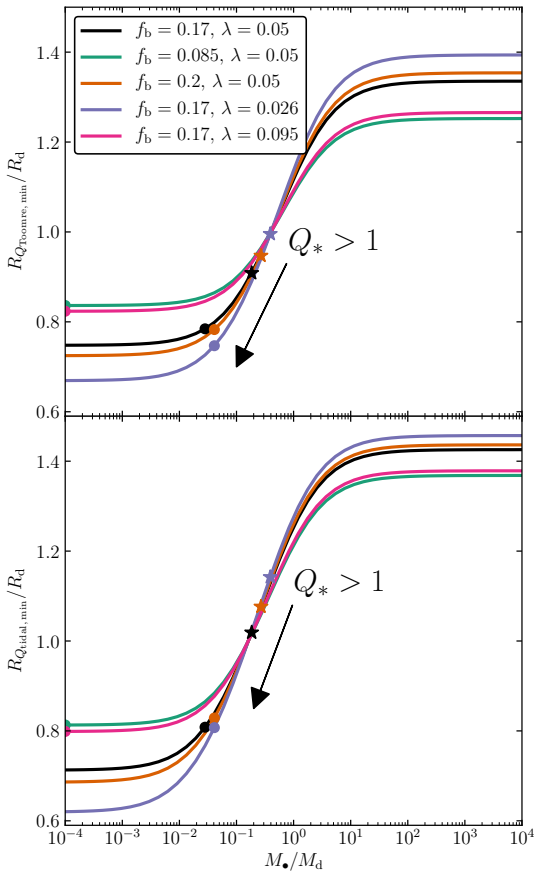

Figure 2.3 *The top panel shows radius where the Toomre stability parameter is minimised as a fraction of the disc scale radius as a function of the mass ratio of the black hole and disc. The bottom panel shows the same for the tidal stability parameter. The black line was found for the fiducial case of* $f_\mathrm{b} = 0.17$, $\lambda = \bar{\lambda} \equiv 0.05$. *The remaining lines represent cases where either* f_b *or* λ *are changed from fiducial case to the values indicated in the legend. Unlike the curves, the position of the markers are dependent on the total mass of the system. The* $M_\mathrm{tot} = 10^9 \mathrm{M}_\odot$ *case is shown as an example. The dots correspond to the point where* $Q_\mathrm{tidal,\,min} = Q_\mathrm{Toomre,\,min}$ *i.e. to the left of these dots the Toomre parameter is a stricter criterion for star formation and to the right the tidal parameter is more the strict of the two. The stars correspond to the point where* $Q_{*,\,\mathrm{min}} = 1$. *There are no star symbols shown for the low baryon fraction and high spin parameter cases (green and pink lines respectively) as the disc is fully stable for both, even in the absence of a black hole.*

of the lines in Figure 2.3 represent a different combination of baryon fraction and spin parameter. While changing the total mass of the system will change the absolute value of Q_*, it does not change the positions (as a fraction of R_d) of the minimum values of Q_Toomre and Q_tidal. That is the ratios f_b and $M_\bullet/M_\mathrm{d}$ define the relative importance of the different components of each Q and therefore shape of the Q profiles. The spin parameter λ defines R_d and therefore changes the surface density of the disc. Hence, the $R_{Q_\mathrm{min}}/R_\mathrm{d}$ – $M_\bullet/M_\mathrm{d}$ relationships are influenced by λ as the disc surface density and velocity profile (and therefore the disc stability) are dependent on it. Increasing the baryon fraction or decreasing the spin parameter leads to a similar change in the $R_{Q_\mathrm{min}}/R_\mathrm{d}$ – $M_\bullet/M_\mathrm{d}$ curves. The curves shown with the higher and lower spin parameters correspond to the upper and lower limits of the 80% confidence interval of the λ probability distribution (Mo et al. 1998). The upper limit to the baryon fraction is unlikely to be much greater than the fiducial value (Qin et al. 2017). Therefore, $f_\mathrm{b} = 0.2$ would be an extreme case. Though a lower baryon fraction than $f_\mathrm{b} = 0.085$ is possible (Qin et al. 2017), such a system would struggle to have an unstable disc in this model. Over this range of values, the lower spin parameter limit case, $\lambda = 0.026344$, has the largest range in $R_{Q_\mathrm{min}}/R_\mathrm{d}$, with a factor of < 2.5 change. This indicates $R_{Q_\mathrm{min}} \sim R_\mathrm{d}$ over the relevant parameter space.

The curves in Figure 2.3 were found to follow the functional form:

$$\frac{R_{Q_\mathrm{min}}}{R_\mathrm{d}} = A - B\tan^{-1}\left[C\left(\frac{M_\bullet}{M_\mathrm{d}}\right)^{-D}\right] \tag{2.14}$$

See Table 2.2 for the values corresponding to each curve in Figure 2.3.

For all curves, $R_{Q_\mathrm{tidal,\,min}}/R_\mathrm{d}$ – $M_\bullet/M_\mathrm{d}$ is steepest between $M_\bullet/M_\mathrm{d} \sim 0.1$ and $M_\bullet/M_\mathrm{d} \sim 2$ and the points found for $Q_{*,\,\mathrm{min}} = 1$ all lie in that range. Note, for $M_\mathrm{tot} = 10^9\,\mathrm{M}_\odot$, the tidal parameter becomes the more strict criterion at $M_\bullet/M_\mathrm{d} < 0.1$ in each case shown.

2.3.4 Change in disc stability with black hole and disc mass

The inner critical radius is shown as a function of black hole mass for different disc masses in the top left panel of Figure 2.4. The purple line represents the same disc mass as used in Figures 2.2. Increasing the disc mass decreases the

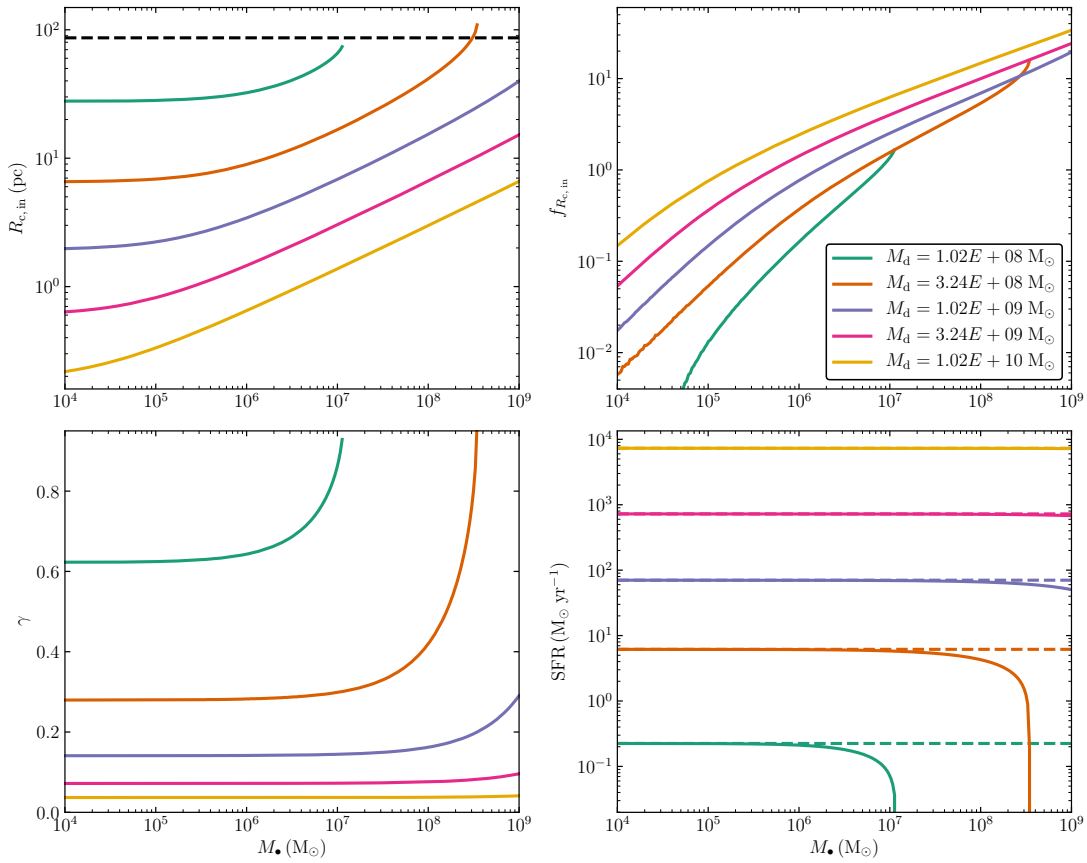

Figure 2.4 *Each of the panels show a property of a disc relating to its stability as a function of black hole mass for different disc masses. The halo mass, $M_{200} = 5 \times 10^8\,\mathrm{M}_\odot$, and the disc scale radius, $R_\mathrm{d} = 86.5\,\mathrm{pc}$, are the same in all cases. The top left panel shows the inner critical radius. The curves tend to the no black hole case at the low mass black hole end. The disc scale radius is shown as a black dashed line. The top right panel shows the relative difference in the inner critical radius with and without a black hole $f_{R_{\mathrm{c,\,in}}}$ (see Equation 2.15). The bottom left panel shows the stable fraction of the disc γ (see Equation 2.16). The bottom right panel shows the star formation rate (SFR) for both with and without a black hole (the solid and dashed lines respectively).*

Table 2.2 *Table of the $R_{Q_{\min}}/R_{\rm d}$ – $M_\bullet/M_{\rm d}$ fit parameters for each curve in Figure 2.3. The fiducial case is shown in the top row.*

		$Q_{\rm Toomre}$			
$f_{\rm b}$	λ	A	B	C	D
0.17	0.05	1.43	0.4596	0.3904	0.6898
0.085	0.05	1.371	0.3571	0.4572	0.7338
0.2	0.05	1.441	0.4842	0.3773	0.6782
0.17	0.026344	1.463	0.5414	0.3505	0.6496
0.17	0.094898	1.381	0.3731	0.4454	0.7275
		$Q_{\rm tidal}$			
$f_{\rm b}$	λ	A	B	C	D
0.17	0.05	1.338	0.3776	0.6429	0.7381
0.085	0.05	1.254	0.2669	0.7043	0.7739
0.2	0.05	1.357	0.4046	0.6302	0.7281
0.17	0.026344	1.398	0.4665	0.6028	0.7031
0.17	0.094898	1.267	0.2836	0.6938	0.7691

critical radius as the disc becomes more unstable. For each case in the top left panel of Figure 2.2 the curve tends to the no black hole case at the low mass black hole end. As said above, as the black hole mass increases the critical radius does increase, however, this increase behaves slightly differently for the higher disc masses. Since the higher disc mass decreases $R_{\rm c,\,in}$, the critical radius is closer to the black hole. This in turn means small changes to the black hole mass at the low mass end has a greater influence on the value of $R_{\rm c,\,in}$; the relative difference in $R_{\rm c,\,in}$ between the cases with and without a black hole is defined as:

$$f_{R_{\rm c,\,in}} \equiv (R_{\rm c,\,in} - R_{\rm c,\,in}(M_\bullet = 0))/R_{\rm c,\,in}(M_\bullet = 0) \tag{2.15}$$

This is shown to increase with disc mass in the top right panel of Figure 2.4 which shows the relative difference as a function of black hole mass for different disc masses. At higher black hole masses the lower mass disc curves are steeper as the black hole mass is increasingly comparable with the disc until the disc is fully stabilised. This is not seen in the higher disc mass cases as the black hole masses investigated do not reach the range required to stabilise these discs. Note the black hole mass required to fully stabilise the $M_{\rm d} = 3.24 \times 10^8\,{\rm M}_\odot$ disc (orange curve) is $M_\bullet \gtrsim M_{\rm d}$ whereas the lowest disc mass case needs only $M_\bullet \lesssim 0.1\,M_{\rm d}$. These numbers are in line with the range where the dependence of $R_{Q_{\rm tidal,\,min}}/R_{\rm d}$ on $M_\bullet/M_{\rm d}$ is strongest ($0.1 \lesssim M_\bullet/M_{\rm d} \lesssim 2$; see previous section).

The stable fraction of the disc is defined as the fraction of the disc mass outside

the unstable region between $R_{\mathrm{c,\,in}}$ and $R_{\mathrm{c,\,out}}$,

$$\gamma \equiv 1 - \frac{M_{\mathrm{g}}(< R_{\mathrm{c,\,out}}) - M_{\mathrm{g}}(< R_{\mathrm{c,\,in}})}{M_{\mathrm{g}}} \tag{2.16}$$

The bottom left panel of Figure 2.4 shows the stable fraction of the disc mass γ as a function of the black hole mass for the same cases as the other panels in the figure. In the model this is the fraction of the disc that is stabilised against gravitational collapse, i.e. the fraction of the disc that is outside the region where star formation can take place. That the most massive disc case is almost completely unstable is to be expected and the black hole has no effect on the stability fraction for this case. Such a disc could not form as in this case as it greatly outweighs its host halo. Looking at the two lowest mass cases, there is a sharp change in the stable fraction of the disc as the black hole mass becomes more comparable with the disc mass ($\sim 10\%$), in line with trend seen in $R_{\mathrm{c,\,in}}$ panel as the disc reaches stability and $R_{\mathrm{c,\,in}} \sim R_{\mathrm{d}}$.

The bottom right panel of Figure 2.4 shows the how the total SFR changes as a function of black hole mass for different disc masses. The two cases with the lowest disc masses are where the difference between the cases with and without a black can be most significant. In these cases, the steep drop in SFR we see as the black hole mass increases appears to simply reflect the stable gas fraction increase on the adjacent panel. In the lowest disc mass the drop-off occurs with $M_{\bullet} \lesssim 0.1\, M_{\mathrm{d}}$ (green line) while with the next higher mass disc the drop-off is at $M_{\bullet} \sim M_{\mathrm{d}}$, following the trend in stable fraction.

2.3.5 Star formation timescale profile

To see how star formation is affected by the mass of the black hole in more detail we need to look at the star formation timescale. Not only is the region where star formation can take place constrained by the black hole but also the star formation timescale in the model can, in principle, be affected by the presence of the black hole. This is because the timescale, t_{SF}, is dependent on Q_{Toomre} and therefore κ (see Equation 2.2), which depends on the black hole mass as outlined above. The top panel of Figure 2.5 shows how the star formation timescale varies as a function of radius for different black hole masses and a constant disc mass ($M_{\mathrm{d}} = 1.02 \times 10^8\,\mathrm{M}_{\odot}$). At a given radius close to the black hole, increasing

the black hole mass increases the timescale until the disc becomes locally stable ($Q_*(R) \geq 1$). There is little variation between the profiles except for the largest black hole mass case with $M_\bullet = 10^7\,\mathrm{M}_\odot$, where the black hole mass is 10% of the disc mass. Between this case and the lowest black hole mass case, the width and area of the star forming region of the disc are around 2/3 smaller while the value of the timescale increases at a given radius by ∼15%. The reduction in the fraction of the gas capable of forming stars at higher black hole masses provides a more significant decrease in the star formation rate than the increase in the value of star formation timescale.

A comparison is made with the no black hole case in the bottom panel of Figure 2.5 through finding the ratio of star formation surface density profiles for with and without a black hole. The star formation rate in the presence of a black hole is less than the no-black hole case at all radii and is ∼15% lower close to the black hole at $R_{\mathrm{c,\,in}}$ for the two most massive black hole cases. The presences of the black hole changes the SFR surface density profile, and therefore the total SFR, due to the change in the Toomre parameter profile. By limiting the range in radius where stars can form the black hole limits the total SFR and would confine the stellar mass to a narrow ring in the disc, ignoring any following redistribution of stars (e.g. through stellar or tidal interactions).

2.4 Evolving halo model

2.4.1 DCBH hosting haloes

The formation of a seed black hole through direct collapse is expected to take place in haloes within regions of high-intensity local LW radiation (e.g Agarwal et al. 2012). Recent studies have shown a local source of H_2-dissociating radiation from nearby quasars or PopII or PopIII stars is required (Agarwal et al. 2016b) to provide the critical LW intensity. For this reason the properties of the model proto-galaxy are chosen to reflect those expected in proximity to a larger galaxy which formed at an earlier time. The LW radiation field is assumed to be sufficient to entirely dissociate molecular hydrogen in the proto-galaxy and the gas temperature is set to $T_{\mathrm{g}} = 8000$ K. Due to this assumed proximity there is a strong likelihood of a DCBH hosting halo to undergo a merger in its evolution (Agarwal et al. 2014). To account for the variation in the growth of seed black

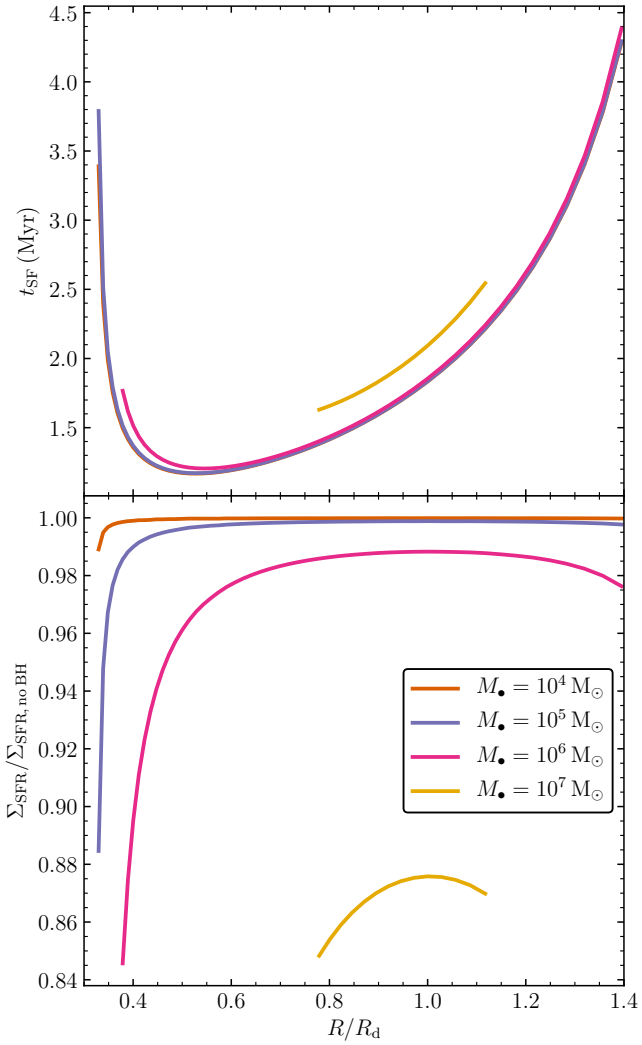

Figure 2.5 *The two panels show the following for a disc of mass* $M_{\rm d} = 1.02 \times 10^8\,{\rm M}_\odot$ *for different black hole masses: The top panel shows the star formation timescale versus radius for different black hole masses; the bottom panel shows the ratio of the star formation surface density profiles for with and without a black hole for different black hole masses.*

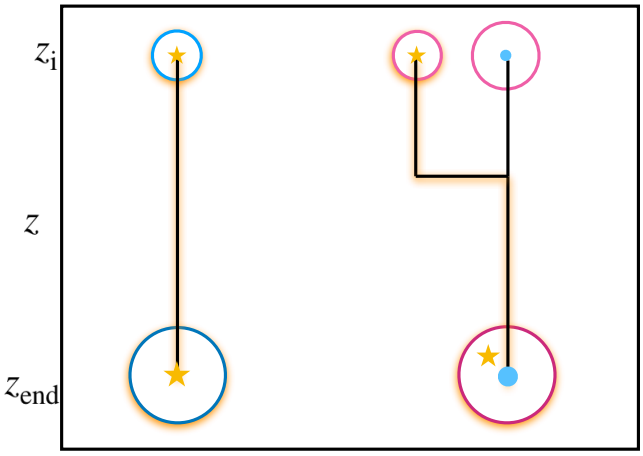

Figure 2.6 *A schematic diagram illustrating the cases investigated here for the evolution of DCBH hosting haloes. The blue case on the left is the isolated, growing halo case and the pink shows an in-falling halo case. The star symbol represents the DCBH hosting proto-galaxy/galaxy while the dots represent a separate, central galaxy.*

hole hosting dark matter haloes we will focus on two evolutionary paths reported in simulations (Agarwal et al. 2014) (see Figure 2.6): (1) an isolated, growing halo and (2) a halo that forms a black hole before it becomes a satellite at some later in-fall redshift, $z_{\rm infall}$. The main difference between these paths is the rate at which new baryons enter the proto-galaxy.

As mentioned above, the cooling in DCBH hosting haloes must be limited to occur via atomic hydrogen (Agarwal et al. 2012). This constrains the metallicity, virial temperature, and therefore the mass of the haloes. All modelled haloes therefore have $T_{\rm v} \gtrsim 10^4$ K and the gas is comprised of atomic hydrogen and helium. For simplicity it is assumed that the cooling timescale is very short and cooling occurs on a dynamical time of the halo, meaning gas accreted by the halo reaches the proto-galaxy on a halo dynamical time(Dekel et al. 2009; Khochfar & Silk 2011). An upper limit on the mass of such a proto-galaxy is therefore the baryonic mass fraction of the halo.

2.4.2 Halo growth

The time evolution is modelled here for the system composed of a gaseous disc, a stellar disc, a black hole and a dark matter halo. The evolving model follows the growth of a galactic disc within an isolated growing host halo after the formation of a massive black hole seed at some initial redshift, $z_{\rm i}$, down to redshifts where

SMBHs have been observed $z_{\rm end} \sim 6.0$ (Fan et al. 2006; Mortlock et al. 2011). The seed formation redshift for the fiducial model is $z_{\rm i} \sim 10$ (Agarwal et al. 2012) though a range of seed formation redshifts are possible (e.g. Begelman et al. 2006) which is investigated below as well. The evolution is followed for both isolated and in-falling DCBH hosting haloes (see Figure 2.6).

The total mass of the system, $M_{\rm tot}$, is made up of the dark matter (DM) halo and the baryons that make up the massive black hole and the galaxy disc. To fit with the conditions expected for the formation of a DCBH, the total initial mass, $M_{\rm tot,\,i}$, is calculated by estimating the mass of an atomic hydrogen cooling halo at $z_{\rm i}$ (Mo et al. 2010). The baryon fraction is assumed to follow the universal value of $f_{\rm b} = 0.17$. Initially, the black hole seed is given a mass in the range $M_{\rm seed} = 10^{4-6}\,{\rm M}_{\odot}$, and the remaining baryons make up the disc mass.

The total mass increases through cosmological accretion of mass onto the system. The following equation taken from Dekel et al. (2013) is used to calculate the growth of the system:

$$M_{\rm tot}(z) = M_{\rm tot,\,i}\,{\rm e}^{-\alpha(z-z_{\rm i})} \tag{2.17}$$

Two methods are used to calculate the halo growth parameter, α. In general, $\alpha = 3/2\,s\,t_1 = 0.806$ where $s = 0.030\,{\rm Gyr}^{-1}$(Dekel et al. 2013) and $t_1 = 2/3\,\Omega_m^{-1/2}\,H_0^{-1} \sim 17.9\,{\rm Gyr}$. As an alternative growth rate, $\alpha = 0.586$ was found by fitting an exponential to the median of the model growth histories for the host halo of the CR7 DCBH from Agarwal et al. (2016b, see their Figure 4).

The total mass is split into the dark matter halo $M_{200}(z) = M_{\rm tot}(z)\,(1 - f_{\rm b})$ and the baryons. The model assumes the disc and central black hole comprise all the baryons in the system and that accreted baryons go directly onto the disc, conserving mass. The equilibrium solutions are used here rather than allowing the accreted material to reach the disc over a dynamical time as the latter required an extra step in the calculation while having little baring on the disc mass at later times and, therefore, the redshift at which the disc became unstable. Hence, the mass of the disc at any given time is the difference between the total baryonic mass and the mass of the black hole.

When sufficient gas is available, the black hole is assumed to grow at a constant Eddington fraction, $f_{\rm Edd}$, leading to the following equation for the growth of the

black hole:

$$M_{\bullet}(t) = M_{\rm seed} \exp\left(f_{\rm Edd}\frac{t - t_{\rm i}}{t_{\rm Sal}}\right) \tag{2.18}$$

where $t_{\rm Sal} = 0.45\,\eta/(1-\eta)$ Gyr is the Salpeter timescale, $t_{\rm i}$ is the formation time and η is the radiative efficiency which is assumed throughout as $\eta = 0.1$ (King et al. 2008). The black hole is assumed to only accrete gas. With a high Eddington fraction the black hole accretion rate can exceed the baryonic growth rate of the halo at late times. This results in a decrease in the gas mass of the disc. If the gas mass drops to zero, the black hole accretion rate will be limited to the baryonic growth rate of the halo.

Note that the gas which feeds the growth of the proto-galaxy disc is assumed to be pristine i.e. with no metals. However, as the cosmological growth of the halo proceeds through mergers, the gas in the halo is likely to be enriched due to a companion galaxy having metals. The increase in metallicity would increase cooling rates, decreasing the gas temperature and inducing disc instabilities. This in turn would lead to higher star formation rates and potentially higher final stellar masses than those predicted by the model.

2.4.3 Star formation and stellar and gaseous disc

Initially, we assume a gaseous disc which is fed by the net accretion of gas resulting from the difference in the gas accreted onto the disc and the black hole. The growth of the disc translates into a growth in the gas surface density such that the central surface density becomes a function of time.

$$\Sigma_{\rm g,\,0}(t) = \frac{M_{\rm g}(t)}{2\pi R_{\rm d}(t)^2} \tag{2.19}$$

After the onset of star formation in the proto-galaxy, some of the gas is converted into stars. The SFR is calculated using the method discussed in section 2.2. For simplicity, stars are assumed to remain on circular orbits where they form in the disc. The stars therefore follow a different surface density profile to the gas and the total disc surface density is simply the sum of the stellar and gas surface

Table 2.3 *Table of model parameters.*

Parameter	Definition	Fiducial (Range)
$M_{\rm seed}$	black hole seed mass ($\rm M_{\odot}$)	10^6 (10^{4-6})
$f_{\rm Edd}$	Eddington fraction	0.25 ($0.0 - 1.0$)
α	Halo growth parameter	0.806 ($0.806, 0.586$)
$z_{\rm i}$	Seed formation redshift	10.0 ($20.0 - 10.0$)
$z_{\rm infall}$	In-fall redshift	0.0 ($10.0, 8.5, 7.0, 0.0$)

densities.

$$\Sigma_{\rm d}(R,t) = \Sigma_{\rm g}(R,t) + \Sigma_{\star}(R,t) \tag{2.20}$$

One aspect this model setup neglects is the formation and migration of star forming clumps. High redshift observations have revealed a population of disc galaxies which appear more clumpy than their local counterparts (van den Bergh et al. 1996; Elmegreen et al. 2005, 2007). These clumps grow from instabilities in galactic discs and the increased gas density results in an enhanced SFR from within the clump (Elmegreen et al. 2007; Agertz et al. 2009; Ceverino et al. 2010). As clump formation is expected in gravitationally unstable discs, the fixed disc profile of the model could result in an under-estimate in the SFR. However, inward clump migration may in fact enhance the growth of the central black hole (Bournaud et al. 2011), increasing the potential impact of AGN feedback. Therefore, it is unclear what impact clump formation and migration would have on the predictions from this model, such as the black hole-stellar mass relation (see Section 2.4.8).

For the purpose of the model one can neglect feedback from stars and the accreting black hole and note that the stellar mass is an upper limit on what could be expected. The velocity dispersion is assumed to be dominated by the sound speed of the gas ($c_{\rm s} \sim 10\,\rm km/s$ with $T_{\rm g} = 8000$ K). However, including feedback effects should lead to an increase in the velocity dispersion of $\sim 10\,\rm km/s$ (see, e.g. Wada et al. 2002; Dib et al. 2006; Agertz et al. 2009) due to supernovae after a few Myr (Schaerer 2002), driving outflows and suppressing star formation.

It is important to note that throughout this study we assume the growing galaxy disc is isolated and therefore does not experience any tidal forces from neighbouring galaxies. This assumption will hold initially, however, as DCBH formation is thought to occur in haloes nearby early star forming galaxies, the

DCBH formation site is likely to experience tidal forces which could disrupt the disc (Chon et al. 2016). The impact of tidal forces on the SFR is complex as tidal interactions can act on the disc in a number of ways. For example, tidal interactions can: heat the disc (Toth & Ostriker 1992), distort the disc to induce gravitational instabilities and enhance star formation (Li et al. 2008), or even destroy the disc entirely (Chon et al. 2016). A full consideration of environmental effects would therefore require the use of numerical simulations. Although, one can argue that as the DCBH host halo will likely have a more massive neighbour, the tidal interactions should be strong, making the destruction of the disc the more likely. Therefore, the isolated model star formation will provide an optimistic estimate of the stellar mass, with environmental effects negatively impacting star formation in DCBH hosts.

2.4.4 Fiducial case

Table 2.3 summarises the parameters discussed above with their fiducial values and the relevant ranges used. For the fiducial evolving model one can make comparisons between cases both with and without a black hole and with and without black hole accretion. For the growth of the halo and the disc we assume an accretion rate in line with Dekel et al. (2013). Using the lower accretion rate and a $T_{\rm v} \sim 10^4$ K halo at $z_{\rm i} = 10$ would result in a system where the disc was never massive enough to be unstable prior to $z = 6$, independent of the black hole mass[4]. The fiducial value for the seed mass is $M_{\rm seed} = 10^6\,M_{\odot}$ and it is assumed that the Eddington fraction is $f_{\rm Edd} = 0.25$ for the accreting black hole case.

Figure 2.7 shows the evolution with redshift of the mass of each component of the model for the three fiducial cases (no black hole, non-accreting black hole, accreting black hole). The stellar mass evolution varies between the different models. The case without the black hole has the largest stellar mass at all redshifts after the onset of star formation while the accreting black hole has the lowest. As the accreting case has the most massive black hole it will have the longest star formation timescales and the highest stable disc fraction, leading to lower star formation rates and hence lower stellar masses. Furthermore, the higher black hole mass leads to a delay in the onset of star formation. The higher black hole changes the Q_* profile such that $Q_{*,\,\rm min}$ is higher for a given disc mass

[4]At higher formation redshifts, $z_{\rm i} \sim 20$, a $T_{\rm v} \sim 10^4$ K halo can form a disc capable of becoming unstable at later times even for the assumed lower accretion rates.

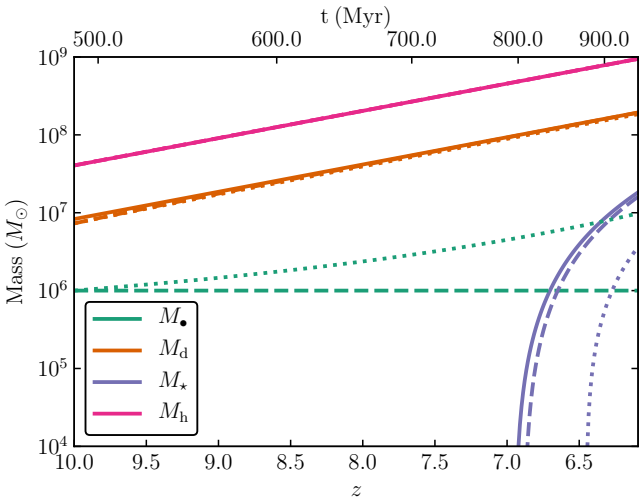

Figure 2.7 *The mass evolution of each of the system components for the fiducial cases. The solid line is the case with no black hole, the dashed line is for the case of a black hole with a constant mass of* $M_\bullet = 10^6\,M_\odot$*, and the dotted line is for the case with a black hole growing from an initial mass of* $M_\mathrm{seed} = 10^6\,M_\odot$ *with* $f_\mathrm{Edd} = 0.25$*.*

and therefore the critical mass of the disc required for it to become unstable is higher. In the constant black hole mass case, this higher critical mass requirement delays the time at which the disc is first unstable as each model has the same cosmological accretion rate. In fact this delay is further enhanced in the accreting black hole case as the net growth rate of the disc will be reduced.

2.4.5 Star formation rate surface density profile

The change in the Toomre and tidal parameter radial profiles due to the presence of a black hole has an affect on the SFR in the disc. Figure 2.8 shows how the SFR surface density evolves in the model with and without a black hole. The region where star formation takes place in the model is shifted outward in the cases with a black hole compared to the one without. Over time the SFR increases throughout the unstable region. This is expected in the model as the formation of stars in a region increases the stellar surface density while the corresponding decrease in gas density is spread out throughout the disc. Meanwhile more gas is accreted through cosmological accretion and R_d increases as the halo grows. This means even as the gas density profile is stretch out there is an overall increase in the total surface density in a region undergoing star formation and this increases the SFR in that region (see Equation 2.3). The lack of feedback effects or any

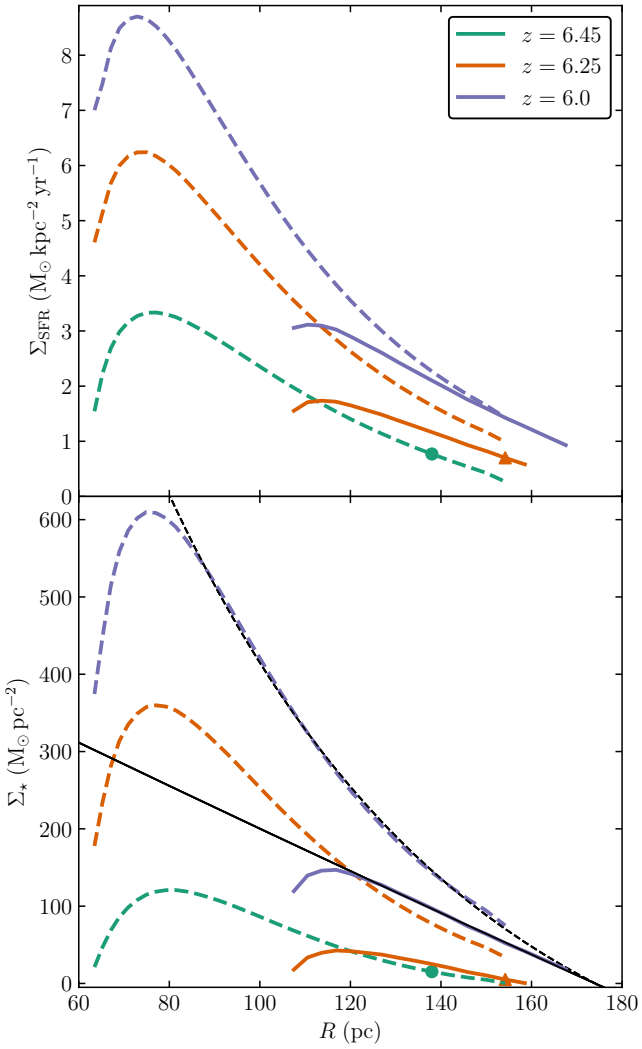

Figure 2.8 *The radial profiles of the SFR surface density and the stellar surface density at three snapshots during the evolution of two models of disc galaxies. The solid lines represent the fiducial model with a growing black hole and the dashed line is the case with no black hole. The first point in time ($z = 6.45$) is taken immediately prior to the onset of star formation in the black hole case and the final snapshot ($z = 6.0$) is at the end of the calculation. In most cases, all star formation is taking place within the scale radius of the disc. Where this is not the case a marker of the corresponding colour indicates the disc scale length. The disc scale radius at each point in time is as follows: $R_{\rm d} = 143.2$ pc for $z = 6.45$, $R_{\rm d} = 155.6$ pc for $z = 6.25$, and $R_{\rm d} = 167.6$ pc for $z = 6$. Exponential surface density profiles, $\Sigma_\star \propto \exp\left(-a\,R/R_{\rm d}\right)$, were fitted to the stellar surface density profiles at $z = 6$ (shown in black). At this redshift the fit parameter was found to be $a = 0.51$ (with a turn over starting at $r = 84$ pc) and $a = 15.1$ (with a turn over at $r = 124$ pc) in the black hole and no black hole cases respectively.*

momentum and mass transfer in the stellar disc results in runaway star formation. As the black hole is allowed to accrete gas there is further increase in the difference in the SFR at late times as the gas surface density is reduced. The differences in the stability profiles and gas density means the SFR and stellar mass surface densities are higher at each point in time and at each radius in the case without the black hole. Looking at the lowest redshift, the presence of the black hole has resulted in a decrease in the width of the annulus of the disc where stars can form by $\sim 1/3$. The resulting ring of stars occupies this same smaller region and the inner region is void of stars, effectively creating a hole in the galaxy stellar disc by enlarging the central region void of stars from ~ 64 pc to ~ 110 pc. The change in the Q_* profiles does result in a fractional increase (9%) in the outer radius of the star formation region but this only has a minor effect on the total SFR of the system.

We can test of whether the disc would remain stable enough to form such a stellar ring by investigating if stellar feedback effects could disrupt the disc. For example, Yajima et al. (2017) demonstrate how supernova feedback can destroy a disc and drive material out of star forming regions. The energy released through supernovae is roughly the energy released through each supernova ($\sim 10^{51}$ erg) multiplied by the number of supernovae events, $N_{\rm SN}$. We can estimate $N_{\rm SN}$ from the SFR by considering a characteristic PopIII stellar mass of $M_{\rm char} \sim 100\,{\rm M}_\odot$ with lifetimes of $t_{\rm life} < 10$ Myr (Schaerer 2002). This gives the energy released through supernovae at a given time of $E_{\rm SN} \sim 10^{51}\,({\rm SFR}\,t_{\rm life}/M_{\rm char})\,{\rm erg} \sim 10^{56}\,({\rm SFR}/{\rm M}_\odot\,{\rm yr}^{-1})\,{\rm erg}$. From the virial theorem, we know that the gravitational binding energy of the disc is roughly $E_{\rm b} \sim M_{\rm d}V_{\rm c}^2/2$ (Binney & Tremaine 2008). Within the region that will form the stellar ring, the binding energy at late times becomes $E_{\rm b} \sim M_\star V_{\rm c}^2/2$ and the ratio of this energy to the energy released through supernova is $E_{\rm SN}/E_{\rm b} \sim 10^4({\rm sSFR}/{\rm Gyr}^{-1})\,(V_{\rm c}/{\rm km/s})^{-2}\,{\rm erg}$. For the fiducial cases explored here this ratio is $E_{\rm SN}/E_{\rm b} \gtrsim 150$, suggesting that the stellar ring would be disrupted by supernova feedback. However, this assumes that none of the energy released through supernovae escapes through cooling radiation.

2.4.6 Evolution of the star formation rate

The radially integrated SFR in Figure 2.9 shows the difference in the total SFR over time. The SFR of the no black hole case is highest at all redshifts after the onset of star formation and the accreting black hole case results in the lowest.

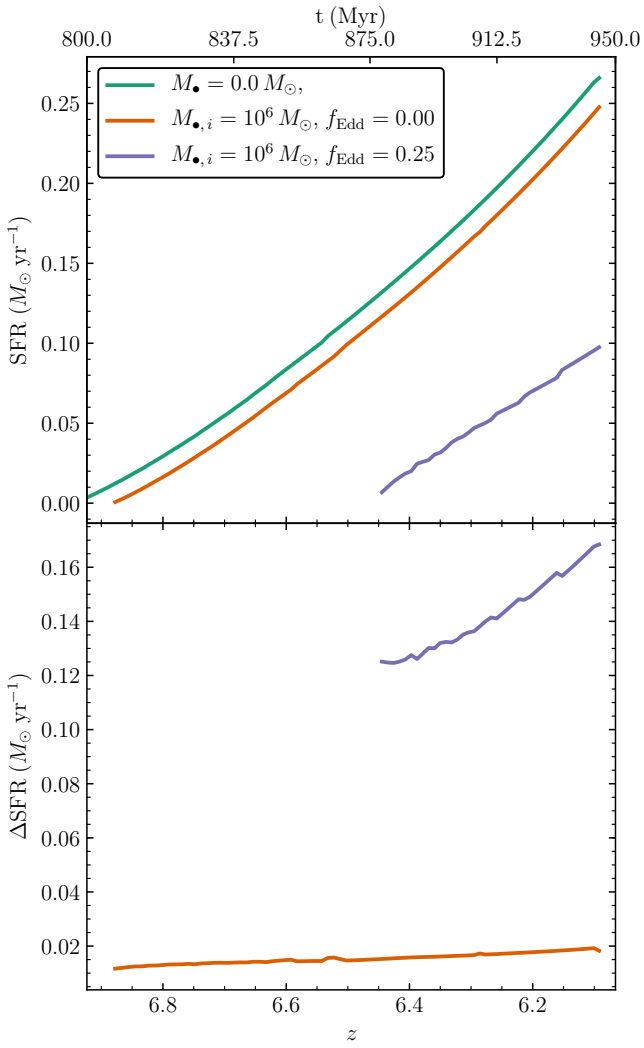

Figure 2.9 *The evolution of the star formation rate for the fiducial cases and the difference between the cases with and without a black hole.* $\Delta\mathrm{SFR} = \mathrm{SFR}_{\mathrm{no\,blackhole}} - \mathrm{SFR}$. *Note* $M_{\bullet,\mathrm{i}} \equiv M_{\mathrm{seed}}$.

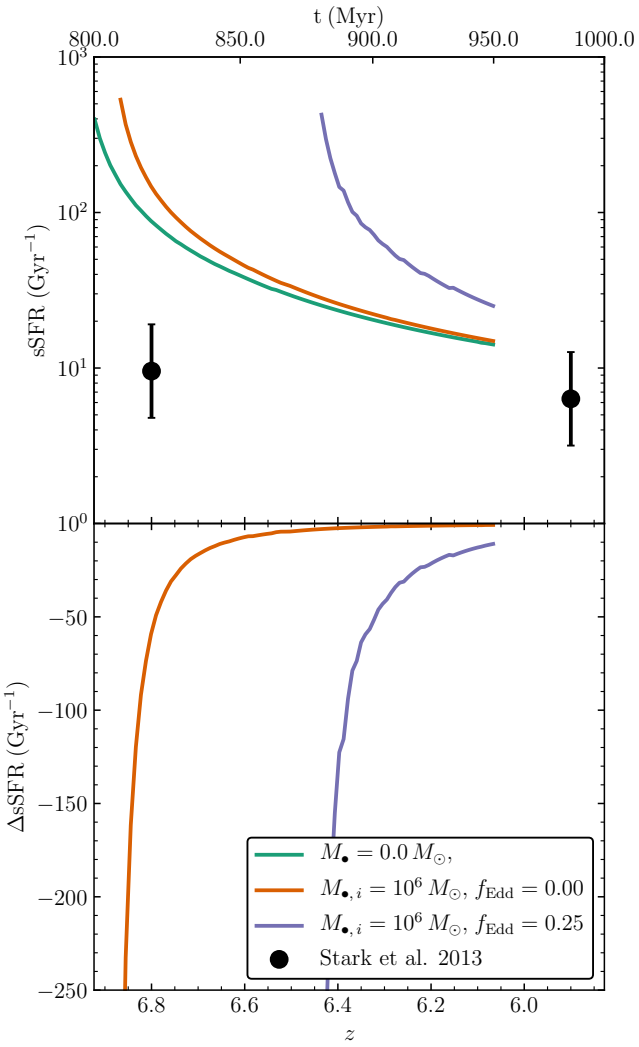

Figure 2.10 *The evolution of the specific star formation rate for the fiducial cases and the difference between the cases with and without a black hole.* $\Delta\mathrm{sSFR} = \mathrm{sSFR}_{\mathrm{no\,blackhole}} - \mathrm{sSFR}$. *Note* $M_{\bullet,\mathrm{i}} \equiv M_{\mathrm{seed}}$.

As we go forward in time we see that the difference between the SFRs increases. As the stellar density increases in the unstable region of the disc, the gas mass will continue to be spread across the total disc profile and the total density will increase within the unstable region, resulting in a local increase in the SFR (see Equation 2.3). As the model does not follow stellar migration, the stellar mass is not redistributed and the SFR simply increases the surface density and so on, leading to a run away effect until the gas density reaches the star formation threshold value. This means, within the model, once a galaxy has a higher SFR and stellar mass it becomes hard for another model to catch up, unless the gas is used up less efficiently due to the presence of a black hole.

The evolution of the specific star formation (sSFR) rate of each of the models

(Figure 2.10) shows interestingly that the sSFR is higher for the higher black hole mass cases. The rise in $Q_{\rm Toomre}$ and $Q_{\rm tidal}$ due to the black hole decreases the SFR and therefore a significant decrease in the stellar mass over time, resulting in an increase in the sSFR. Indeed, without the black hole the sSFR is lower at early times as the stellar surface density will be significantly larger due to the difference in the time at which star formation can first occur in the disc. As the system progresses the stellar masses become more comparable and the difference in the sSFR decreases.

When compared to observations (Stark et al. 2013), I find the model sSFR is greater by a factor of 10 at $z = 6.8$, though the lower mass black hole and no black hole cases appear to be following a trend which would agree with the $z = 5.9$ data point. However, the relationship between SFR and stellar mass has a large scatter and the slope varies with stellar mass (Whitaker et al. 2014), meaning large deviations from this median value in sSFR for individual galaxies is to be expected, particularly at low masses. Indeed, the findings of the model suggest DCBH hosting galaxies should generally have a higher sSFR, providing a possible tool for identifying candidate DCBH hosts.

2.4.7 Onset of star formation

The top panels of Figure 2.11 show how the redshift at which star formation first occurs in the model depends on the seed mass and the growth rate of the black hole for an atomic hydrogen cooling halo that forms a DCBH at $z = 10$ while the remainder of its baryonic mass goes into making a disc. For the case of Eddington limited accretion ($f_{\rm Edd} = 1$) even the lowest mass in the estimated range of the DCBH masses, $M_{\rm seed} = 10^4\ M_\odot$, results in a disc that will never undergo star formation. Yet, high accretion rates close to the Eddington limit are required for even the most massive DCBHs at $z \sim 10$ to reach the $M_\bullet \sim 10^9\,{\rm M}_\odot$ by $z \gtrsim 6-7$ as observed (Fan et al. 2006; Mortlock et al. 2011). This indicates DCBH formed and grew into SMBHs in separate progenitors from their eventual host galaxies, in order for these massive quasars to be observed within massive galaxies at $z \sim 6$. In fact, for the upper limit of the DCBH mass range, $M_{\rm seed} = 10^6\ M_\odot$, star formation is inhibited for the $f_{\rm Edd} = 0.5$ case and is delayed by ~ 100 Myr with $f_{\rm Edd} = 0.25$. Most notably at this formation redshift ($z_{\rm i} \sim 10$), any combination of seed mass and growth rate which leads to the growth of a $M_\bullet \sim 10^9\,{\rm M}_\odot$ SMBH by $z \sim 6$ inhibits star formation in the host.

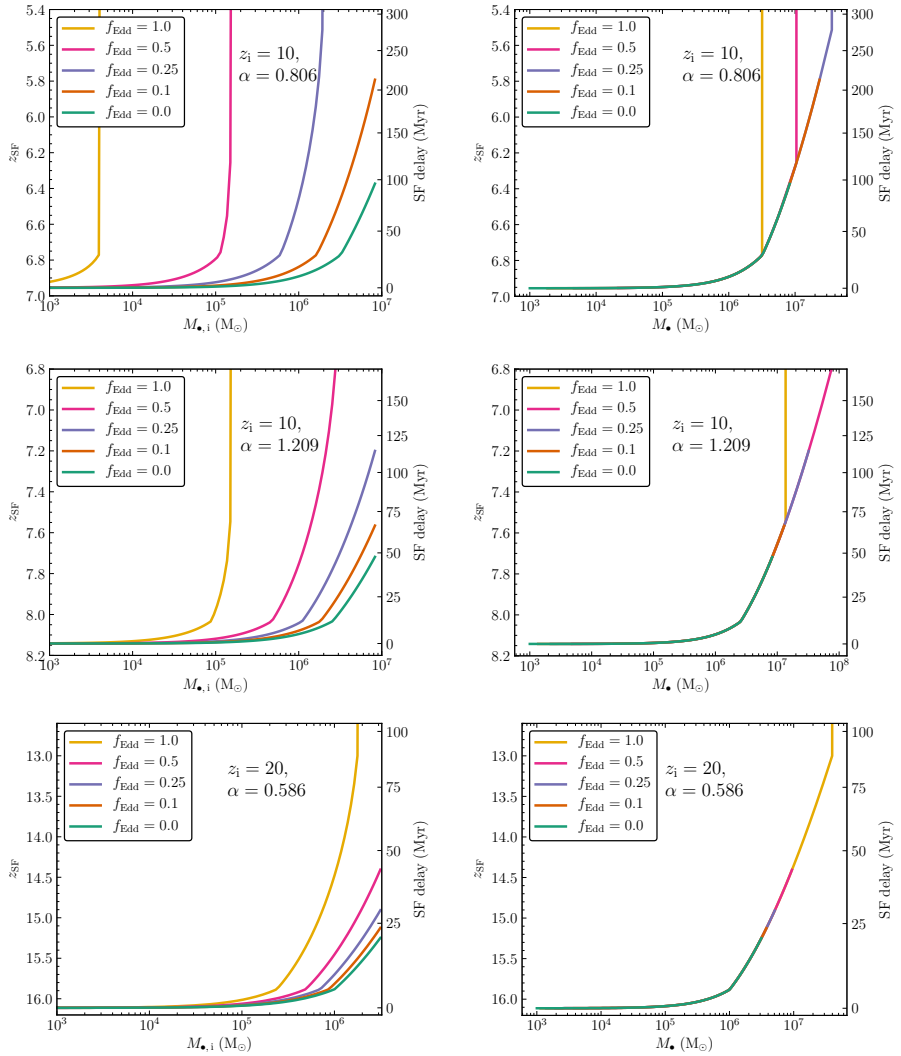

Figure 2.11 *The left panels show the redshift at which the modelled disc first becomes unstable (i.e. $Q_{*\,\rm min} = 1$) and is able to form stars ($z_{\rm SF}$) as a function of the initial black hole seed mass ($M_{\rm seed}$) for different fractions of the Eddington limit accretion rate ($f_{\rm Edd}$). The right panels show the same except with the black hole mass at $z_{\rm SF}$ on the x-axis. The time difference between the onset of star formation with and without a black hole is also shown on the right hand side to indicate the delay caused by the stabilising effect of the black hole. The upper limit of the initial black hole mass range is the total baryonic mass of the atomic hydrogen cooling halo at the DCBH formation redshift of $z \sim 10$ for the top two rows of panels and $z \sim 20$ for the bottom. The growth rate of the halo follows Equation 2.17 with $\alpha = 0.806$ for the top panels, $\alpha = 1.209$ for the middle and $\alpha = 0.586$ for the bottom. The $f_{\rm Edd} = 0.25 - 1$ lines in the top panels each reach a maximum seed mass above which the disc will never become unstable and be able to form stars. In the bottom panels this is only seen for the $f_{\rm Edd} = 1$ line.*

In the cases of no black hole growth and $f_{\rm Edd} = 0.1$, the disc will eventually undergo star formation, even when the black hole seed mass is at its maximum i.e. at the seed's formation it takes up the entire baryonic mass of the halo ($M_{\rm seed} = M_{\rm b} = 7.82 \times 10^6\ M_\odot$) and the disc mass is initially zero. The onset of star formation is delayed somewhat in these $M_{\rm seed} = M_{\rm b}$ seed cases, with $f_{\rm Edd} = 0.1$ leading to a delay by ~ 200 Myr which is significant as this is around a fifth of the age of the universe at this epoch. Note in all models the black hole mass never exceeds the total baryonic mass in the redshift range investigated in the models where $z_{\rm SF}$ is defined.

The growth rate of the halo and therefore the disc greatly influences this result. The lower the growth rate of the halo the more delayed star formation will be. As highlighted above, the growth rate modelled for the DCBH hosting halo of CR7 by Agarwal et al. (2016b) is sufficiently low that with $z_{\rm i} = 10$ the surface density of the disc is never high enough for stars to form over the redshift range investigated. However, at earlier formation times the role of the black hole decreases as the growth rate of the halo becomes higher at larger redshift. With a formation redshift of $z_{\rm i} = 20$, a black hole with an initial seed mass of $M_{\rm seed} = 10^6\,{\rm M}_\odot$ growing at the Eddington limit will be unable to prevent star formation, only delaying the onset by ~ 40 Myr (see bottom panels of Figure 2.11).

Similarly to increasing the formation redshift, increasing the growth rate of the halo decreases the influence of the black hole. Genel et al. (2008) find a scatter in the growth rate of DM haloes which they approximate as $\approx \left\langle \dot{M}_{\rm DM} \right\rangle (2.5/(1+z))^{0.2}$ where $\left\langle \dot{M}_{\rm DM} \right\rangle$ is the mean halo growth rate. Assuming the growth rate is a linear function of the halo mass, in line with Equation 2.17, leads to $\sigma_\alpha \approx \langle \alpha \rangle (2.5/(1+z))^{0.2}$. The middle panels of Figure 2.11 shows the case for a formation redshift of $z_{\rm i} = 10$ with a growth rate of $\alpha = 1.209$, $\times 1.5$ the fiducial rate and within the $1-\sigma_\alpha$ scatter at $z = 6$. With this case the disc rapidly becomes more massive than the fiducial case and therefore becomes unstable much earlier. The black hole mass required to keep the disc stable increases; it has to grow much faster to keep up with the disc and prevent star formation. This is illustrated by looking at a $M_{\rm seed} \sim 2 \times 10^5\,{\rm M}_\odot$ seed case. Growing at the Eddington limit, such a seed does prevent star formation, however, this is achievable at the same growth rate by a seed with a mass 20 times smaller at $M_{\rm seed} \sim 5 \times 10^3\,{\rm M}_\odot$ in the fiducial case. Furthermore, a $M_{\rm seed} \sim 2 \times 10^5\,{\rm M}_\odot$ seed in the fiducial case is capable of preventing the onset of star formation growing at half the black hole accretion rate.

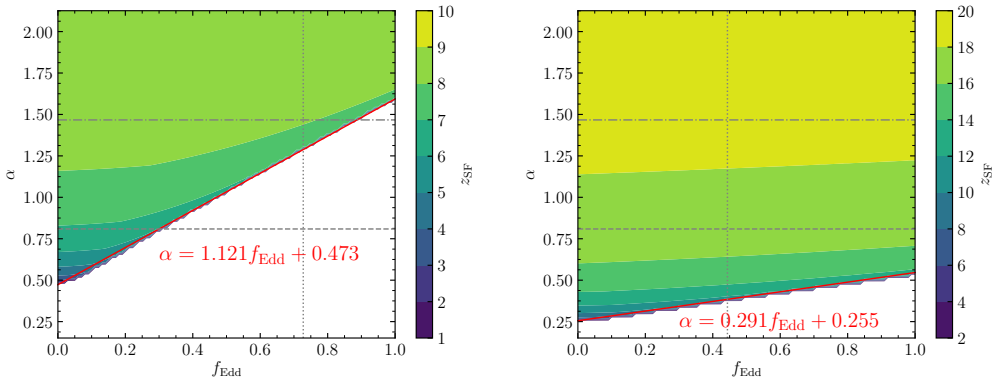

Figure 2.12 *The variation of $z_{\rm SF}$, the redshift at which star formation can first occur, with α and $f_{\rm Edd}$, the accretion rate parameter of the halo and the black hole Eddington fraction respectively. Where no value for $z_{\rm SF}$ is shown, the system will never undergo star formation. The initial seed mass is $M_{\rm seed} = 10^6\,{\rm M}_\odot$. The formation redshift is $z_{\rm i} = 10$ in the left panel and $z_{\rm i} = 20$ in the right panel. The range in α shown is from the lower $1{-}\sigma_\alpha$ limit to the upper $2{-}\sigma_\alpha$ limit at $z = 6$. The average halo accretion rate parameter, and the fiducial value, $\alpha = 0.809$ is shown as the grey, dashed line. The upper $1{-}\sigma_\alpha$ limit of $\alpha = 1.467$ is shown as the grey dot-dash line. The grey, dotted line represents the minimum Eddington fraction for which a $M_{\rm seed} = 10^6\,{\rm M}_\odot$ seed black hole will reach $M_\bullet = 10^9\,{\rm M}_\odot$ by $z = 6$. A best-fitting line for $f_{\rm Edd} > 0.01$ is shown in both cases for the critical values of α and $f_{\rm Edd}$ where the model transfers from becoming unstable at some redshift to never being able to form stars.*

The interplay of the halo and black hole growth rates is well summarised in Figure 2.12. The figure shows how the onset of star formation varies with the growth rate of the halo and the black hole and also depends on the formation redshift. z_{SF} is calculated as a function of the halo growth parameter, α, and Eddington fraction for the same seed mass of $M_{\rm seed} = 10^6\,{\rm M}_\odot$ at formation redshift $z_{\rm i} = 10$ and $z_{\rm i} = 20$. The range in α shown is from the lower $1{-}\sigma_\alpha$ limit to the upper $2{-}\sigma_\alpha$ limit at $z = 6$, where σ_α was calculated using the approximation from Genel et al. (2008) as outlined above. In the $z_{\rm i} = 10$ case, a significant fraction of the parameter space results in a model that is unable to ever form stars, particularly at higher Eddington fractions. Above the Eddington fraction at which the black hole reaches $M_\bullet = 10^9\,{\rm M}_\odot$ at $z = 6$ ($f_{\rm Edd} = 0.728$), a higher than average halo growth parameter is required for star formation to occur. At even higher black hole accretion rates, $f_{\rm Edd} \gtrsim 0.9$, only haloes growing more than $1{-}\sigma_\alpha$ faster than the average growth rate are sufficient. However, with $z_{\rm i} = 20$, only the models with a slower than average halo growth rate, $\alpha \lesssim 0.8$, have a significantly delayed onset of star formation.

2.4.8 Black hole-stellar mass relation

How strong an effect the black hole has on the galaxy will depend on the growth rate of both the black hole and the disc. Figure 2.13 shows the evolution of the black hole and stellar mass for different seed masses and accretion rates. The black hole mass is initially significantly more massive but as the SFR is significantly larger than the black hole accretion rate in these cases, the stellar mass quickly catches up with the black hole mass. However, by the end of the calculation at $z = 6$, only the lowest mass seed region reaches to the $M_\bullet \sim 10^{-3}\,M_\star$ line seen empirically at lower redshifts (Häring & Rix 2004; Kormendy & Ho 2013; Reines & Volonteri 2015). This implies a black hole cannot grow to lie on the black hole-stellar mass relation at this point in cosmic time if the halo grows with an average growth rate. Mergers, for example, with evolved galaxies hosting only small or no black holes are required to boost the stellar mass once the black hole has grown. Hence, it is likely that these seeds are generated in satellites prior to falling into their host galaxies to lie on the relation.

It is also thought that the empirical scaling relation of black hole and stellar mass is linked to the interaction of AGN and star formation; the feedback attributed to AGN helps regulate the SFR and vice-versa (see, e.g. Silk & Rees 1998; Gabor

et al. 2010; Silk 2013), producing this correlation. Here, the feedback from either the black hole or stars is not modelled, yet it is not clear that the inclusion of feedback would resolve the discrepancy of the results with the empirical relation. This model predicts black hole and galaxy masses that would place the model galaxies above the relation, meaning the black holes are too massive relative to their hosts. Yet the inclusion of feedback from stars to regulate the growth of black holes would be insufficient as the model black holes gain most of their mass prior to the onset of star formation.

One aspect which has not been considered here is the potential variation in the star formation efficiency. There is some evidence that suggests the normalisation of the Kennicutt-Schmidt relation evolves with redshift (e.g. Tacconi et al. 2013), indicating galaxies at higher redshift have higher star formation efficiencies. Applying a redshift dependent correction to the star formation efficiency used in equation 2.3 would result in an increase in the stellar mass, potentially resolving the discrepancy seen in Figure 2.13 between the models and the local relation.

The introduction of metals, either following the first generation of stars or through mergers with enriched galaxies, could also account for some of this discrepancy. With an increase in metallicity comes an increase in cooling rates, reducing the gas temperature and leading to further disc instabilities. This would then result in an increase in star formation rate and therefore the total stellar mass.

2.4.9 Infalling host halo

The infall of the seed black hole hosting halo to become a satellite of a more massive, central galaxy is modelled by cutting the growth of the halo. At a given redshift, $z_{\rm infall}$, the halo growth rate is set to zero and in turn accretion of fresh baryons stops. The disc mass only changes as the black hole continues to accrete the remaining gas.

If the in-fall event happens prior to the onset of star formation the disc will never become unstable, due to the halt in the growth of the disc mass. This would result in a massive black hole surrounded by a primordial gaseous disc, assuming the black hole is unable to accrete all the gas, and orbiting a central galaxy. For example, this would be true in the fiducial case if the in-fall occurs at a higher redshift than the onset of star formation at around $z \lesssim 7$. As the onset of star formation is delayed more by a more massive and rapidly-accreting black hole,

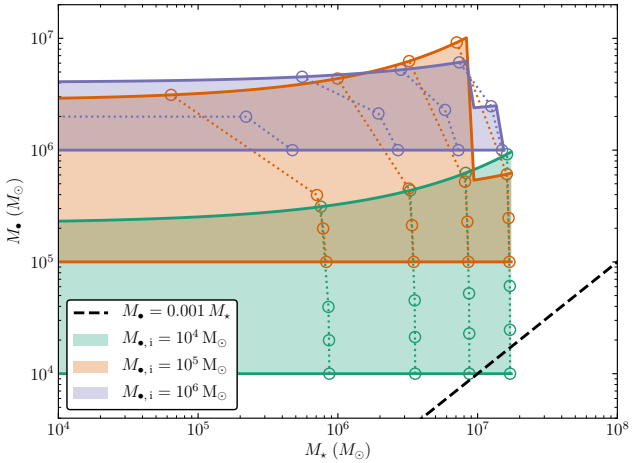

Figure 2.13 *The evolution of the total stellar mass and black hole mass was calculated for a range of growth rates ($f_{\mathrm{Edd}} = 0.0$, 0.1, 0.2, 0.5, 1.0; note $f_{\mathrm{Edd}} = 1.0$ cases are not shown) and seed masses ($M_{\mathrm{seed}} = 10^6\,\mathrm{M}_\odot$, $10^5\,\mathrm{M}_\odot$, $10^4\,\mathrm{M}_\odot$). Note $M_{\bullet,\mathrm{i}} \equiv M_{\mathrm{seed}}$. The coloured regions represent the spread in the evolution for different accretion rates given the same initial seed mass. Each model starts from the left hand side of the plot (with a stellar mass of zero) and once the onset of star formation is reached the evolution traces from left to right. The black hole accretion rates shown here are limited to $f_{\mathrm{Edd}} \leq 0.2$, $f_{\mathrm{Edd}} \leq 0.5$, and $f_{\mathrm{Edd}} \leq 0.5$ in the $M_{\mathrm{seed}} = 10^6\,\mathrm{M}_\odot$, $M_{\mathrm{seed}} = 10^5\,\mathrm{M}_\odot$, and $M_{\mathrm{seed}} = 10^4\,\mathrm{M}_\odot$ seed mass cases respectively as the higher accretion rates entirely prevent star formation. The dashed line represents $M_\bullet = 10^{-3}\,M_\star$ (see, e.g. Kormendy & Ho 2013) and the coloured dotted lines connect points at the same redshift for each seed mass case. From left to right the lines correspond to $z = 6.7$, 6.5, 6.3, 6.1.*

the more massive the black hole is the more likely an in-fall can occur prior to stars forming in the disc.

In general, the SFR is maintained by the influx of gas to the disc. Cutting off this supply by having an in-fall after the onset of star formation leads to a rapid decrease in the gas density as the gas is converted into stars and accreted by the black hole. The rate at which the SFR then decreases to zero will then depend on the stellar mass and the black hole accretion rate. Eventually, the stellar and black hole masses will each reach a maximum and stop growing, starved by the lack of gas. Depending on the system, the result will likely be a satellite galaxy with $M_\bullet/M_\star > 0.001$ (following from Figure 2.13) which could survive to lower redshifts.

A study by Agarwal et al. (2014) identified haloes where DCBHs formed within a cosmological, hydrodynamical simulation. I highlight two of the cases they identified with a DCBH formation redshifts of $z_\mathrm{i} \sim 10$. One where the seed forms in a site close to one dominant galaxy and another where the formation in a clustered environment. In first case the DCBH host falls in to its largest neighbour at $z \sim 8.5$, which is $\lesssim 200$ Myr after the formation of the seed. Within the model this would likely occur prior to the onset of star formation in the seed hosting halo. In the second case the seed hosting halo undergoes an in-fall at a later time, around $z \sim 6$, well after the likely onset of star formation from the model. However, the environment of the cluster may play a stronger role in this scenario.

2.5 Discussion & conclusions

I use an analytical model to investigate the effect of a DCBH seed on the stability of proto-galaxy discs and the resulting suppression of star formation. I look at how the Toomre and tidal stability parameters profiles of an exponential disc change due to the presence of a black hole in the centre of the system and link the stability of the disc to the star formation rate. I show how the black hole has a gravitationally stabilising effect on the inner region of the disc which increases the star formation timescale locally and limits the region of the disc where star formation can occur, decreasing the modelled SFR. I also estimate upper limits on the growth of a galaxy around a seed black hole by gas to investigate how the interplay of cosmological accretion, accretion onto the black

hole and the stabilizing effect of the black hole can be important in determining the circumstances under which stars can form.

After the initial onset of star formation, I find that the radial extent of the star forming region remains relatively constant. Under the assumption of stars staying on circular orbits and not migrating in the disc, the process of forming stars increases the local surface density ($\Sigma_{\rm g} + \Sigma_{\star}$). This increases the self-gravity of the disc locally and decreases the effect of tidal forces on the gas. Removing the support from the tidal shear against gravitational collapse then leads to the further formation of stars in this same region. Following a short period beginning at the onset of star formation (while the stellar mass is still negligible), all subsequent star formation in the disc is largely confined to the region where stars have already formed. As stability increases in the presence of a massive black hole, the radial extent of the region where stars can form narrows and the total SFR is reduced.

The radial extent of the region where stars can form in the model disc is small ($\sim$ 100 pc) due to the disc properties at $z = 6$, even in the absence of a black hole. For the evolving model with a formation redshift at $z_{\rm i} = 10$, I calculate the angular size of the stellar disc in the no black hole case at $z = 6$ to be $\theta < 0.02$ arcseconds and note this is less than the angular resolution of the James Webb Space Telescope (JWST), even at the shortest possible wavelengths. Resolved observations of such objects at this redshift would therefore by infeasible with current instruments.

The presence of a growing black hole seed can greatly affect the star formation history of its host galaxy, even preventing the formation of stars entirely. Increasing the mass of the black hole or the scale radius of the disc increases the stability of the disc, while increasing the disc mass decreases the stability. In the fiducial case, the disc becomes more unstable in the star forming region as the disc mass increases with the growth of the halo, resulting in SFR increasing with time. I find the sSFR in the model increases with higher black hole mass and that the calculated sSFR is higher than the observed median value at high redshift (Stark et al. 2013), particularly at times close to the onset of star formation. These results suggest that systems hosting DCBHs should occupy the upper envelope of the sSFR distribution for any given stellar mass. Indeed, high sSFR galaxies could potential be used for the identification of DCBH hosts. As the model evolves to lower redshifts, the discrepancy between the model sSFR and the observations decreases.

Increasing the accretion rate of the black hole leads to an increase in the stability of the disc at a given time as the black hole mass increases and the disc mass decreases. This can lead to a delay in the time where the disc first becomes unstable and forms stars. This delay in the onset of star formation is not only dependent on the black hole growth rate and seed mass but also the growth of the disc and halo. As halo growth rates are higher at high redshift, the delay is also a function of the formation redshift of the black hole. For a sufficiently high black hole accretion rate and seed mass, the disc can be prevented from ever forming stars. At the lowest halo growth rates and high black hole accretion rates, even models with early formation times have no stars forming. Such a low halo growth rate is typical of satellite galaxies (see, e.g. De Lucia et al. 2012). This suggests the chance of a SMBH forming with no stellar disc counterpart is more likely in satellite galaxies. Indeed, this would also occur if an in-fall event were to occur prior to the onset of star formation.

I find that the halo in which a seed is born at $z = 10$ is prevented from having significant star formation if the black hole grows at the Eddington limit. If a seed black hole is to grow at the rate required to increase in mass by $\gtrsim 3$ orders of magnitude between $z \sim 10$ and $z \sim 6$, star formation in its host is suppressed, placing such a system above the black hole-stellar-mass relation. This suggests that DCBH galaxies will move towards the local black hole-stellar mass relation via potential mergers with already evolved galaxies without massive black holes and not self-regulated co-evolution. Alternatively, this discrepancy can be resolved if either the formation of the DCBH is pushed to higher redshift ($z \sim 20$) or if the evolution of the black hole-galaxy system takes place in haloes with higher than average growth rates.

2.6 Appendix: Change in stability with disc scale radius

In the main body of this study the disc scale radius is calculated using Equation 2.5 with the mass of the system and the relevant redshift. Unless otherwise stated, the spin parameter of the halo is assumed as $\lambda = \bar{\lambda} = 0.05$ yet in nature λ varies between haloes (Mo et al. 1998), resulting in a range of possible scale radii for the disc.

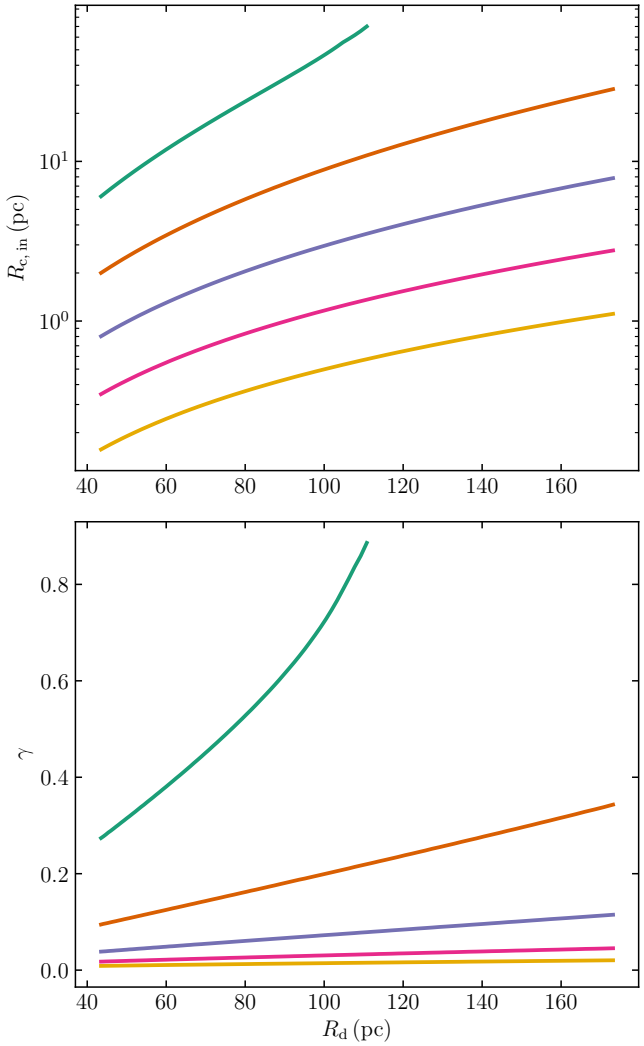

Figure 2.14 *How the stability of the disc varies as a function of disc scale radius for different disc masses. The top panel shows the inner critical radius and the bottom shows that stable fraction of the disc. The lower limit to the range in R_d corresponds to $\lambda = 0.025$ while the upper limit corresponds to $\lambda = 0.1$. The disc masses are the same as in Figure 2.4: $10^8\,M_\odot$ (green), $3.24 \times 10^8\,M_\odot$ (orange), $10^9\,M_\odot$ (purple), $3.24 \times 10^9\,M_\odot$ (pink) and $10^{10}\,M_\odot$ (yellow).*

Figure 2.14 shows how varying λ, and therefore $R_{\rm d}$, changes the inner critical radius ($R_{\rm c,\,in}$) and stable fraction of the disc (γ). One can see from the figure that the stability of the disc is strongly sensitive to $R_{\rm d}$, particularly in the lowest mass case (the green line). Increasing $R_{\rm d}$ decreases the surface density of the disc, raising the entire Q_* profile, which leads to an increase in inner critical radius and stable fraction. In the lowest mass case, doubling $R_{\rm d} \sim 43.3$ pc to $R_{\rm d} \sim 86.5$ pc increases $R_{\rm c,\,in}$ by a factor of $\sim$5 and roughly doubles the value of γ.

As increasing $R_{\rm d}$ or $M_\bullet$ each result in an increase in the stable fraction of the disc the significance of the stabilising effect of the black hole will vary with halo as the spin parameter varies and the resulting size of proto-galaxies vary.

Chapter 3

Mass transport in galaxy discs limits black hole growth to sub-Eddington rates

This chapter is composed of a paper published in MNRAS (Eastwood et al. 2019). Revisions have been made as requested by the allocated peer during the review process.

3.1 Introduction

Super-massive black holes (SMBHs) have been observed to power quasars at redshifts as high as $z \gtrsim 7$ (Fan et al. 2006; Mortlock et al. 2011; Bañados et al. 2018). In ΛCDM, the Universe is understood to be only ~ 800 Myr old at this epoch (Planck Collaboration et al. 2016) and yet these SMBHs with masses of $M_\bullet \sim 10^9$ $\mathrm{M}_\odot$ are abundant with comoving number densities of around $\phi \sim 1\,\mathrm{Gpc}^{-3}$ (Fan et al. 2003). If the remnants of the first generation of stars are the progenitors of SMBHs, they must have grown roughly seven orders of magnitude over extremely short timescales. The growth rates necessary for this are above the classical upper limit on the accretion of material, the Eddington limit (see however, Inayoshi et al. 2016; Pacucci et al. 2017).

Studies have looked to resolve this issue by introducing alternative black hole formation mechanisms with the capability of generating higher mass progenitors

for SMBHs, known as massive seed black holes (see Volonteri 2010, , for a review). A higher mass seed black hole has the advantage of requiring a lower average growth rate to become super-massive, given the same period in which to grow. One such alternative formation mechanism is the direct collapse of primordial gas in a $T_{\rm vir} \gtrsim 10^4$ K halo, prior to the formation of a galaxy, creating a single massive seed with $M_\bullet \sim 10^{4-6}$ $M_\odot$ (Bromm & Loeb 2003; Agarwal et al. 2012, 2014). Known as direct collapse black holes (DCBHs), these objects are thought to form in metal-free haloes (Begelman et al. 2006) with a local intensity of Lyman-Werner (LW) photons[1] high enough to photo-dissociate any H_2 molecules, along with a sufficient intensity of photons to photodetach any H^- (Shang et al. 2010; Agarwal et al. 2016a). In the absence of H_2 and H^-, the primordial gas cannot cool below the atomic cooling limit at $T_{\rm gas} \sim 8000$ K, avoiding fragmentation during the subsequent gravitational collapse (Spaans & Silk 2006; Dijkstra et al. 2008; Shang et al. 2010).

Even with the most optimistic seed masses, maintaining the necessary growth rate for seed black holes to become super-massive ($M_\bullet \sim 10^9$ $M_\odot$) is still a challenge (Dubois et al. 2015; Latif et al. 2018). Simulations of massive black holes traditionally use Bondi-Hoyle-Lyttleton accretion (Bondi & Hoyle 1944, Bondi 1952, Edgar 2004, see however, Hopkins & Quataert 2011, Anglés-Alcázar et al. 2015 and Beckmann et al. 2018), where the accretion rate is related to the properties of the local medium and the black hole mass, to calculate the growth rate of the black hole. Theoretically, this could result in super-Eddington growth rates. Indeed, there are indications that super-Eddington accretion could be viable through a number of scenarios (Ohsuga et al. 2005; Pacucci et al. 2015; Inayoshi et al. 2016; Pacucci et al. 2017; Takeo et al. 2019). However, high-resolution numerical simulations of massive black holes that account for the feedback from AGN and stars struggle to reach the Eddington accretion rate (Johnson et al. 2011; Dubois et al. 2015; Latif et al. 2018).

High intensities of LW photons are found in close proximity to massive galaxies with significant, early star formation, making haloes in the vicinity of the first galaxies ideal formation sites for DCBHs (Dijkstra et al. 2008; Agarwal et al. 2018). Indeed, cosmological simulations have shown that DCBH formation can occur throughout the Universe at $z \sim 10 - 20$, with such haloes particularly favoured as formation sites (Agarwal et al. 2012, 2014; Wise et al. 2019). The

[1]UV photons with energies of $11.2 - 13.6$ eV capable of dissociating H_2 molecules, though hereafter also used to loosely refer to photons with energies > 0.76 eV, capable of causing the photo-detachment of H^-.

growth histories of haloes within these simulations show that once a DCBH is formed, the subsequent merger of the DCBH host halo with a more massive central galaxy's halo is likely. This means that DCBH seeds are unlikely to remain isolated throughout their evolution and at least one major merger should occur following their formation (Dijkstra et al. 2008).

Merger events are known to drive strong starbursts in galaxies and are capable of feeding black hole growth (Hopkins et al. 2006; Li et al. 2007; Di Matteo et al. 2008). Furthermore, there is evidence that the galaxy-black hole scaling relations observed at lower redshifts (see, e.g. Kormendy & Ho 2013; Heckman & Best 2014) are likely reached through growth driven by mergers (Di Matteo et al. 2005; Schawinski et al. 2006; Hirschmann et al. 2010; Lamastra et al. 2010). In this scenario, mergers are thought to instigate bursts of star formation (Mihos & Hernquist 1996) and drive strong inflows of gas to feed quasar activity (Springel et al. 2005a). The resulting energy released by an active quasar heats and expels gas, quenching star formation while potentially enhancing further black hole growth (Di Matteo et al. 2005; Hopkins et al. 2006). However, the significance of mergers in driving the growth of SMBHs has more recently been called into question (see, e.g. Fanidakis et al. 2012; Hirschmann et al. 2012; Del Moro et al. 2016; Villforth et al. 2017; Hewlett et al. 2017; Steinborn et al. 2018). Observations have found no statistical evidence for an enhanced merger fraction in galaxies with AGN, and indicate the role of mergers in driving activity is, at best, secondary to other fuelling mechanisms (see, e.g. Villforth et al. 2017). Though, merger-driven activity is at least slightly more significant at higher redshift (Del Moro et al. 2016; Hewlett et al. 2017). These observational results are somewhat controversial due to AGN survey limitations (e.g. Juneau et al. 2013) and the challenges of observing evidence of merger-driven activity as a result of the long time delay between merger events and the subsequent AGN activity (Schawinski et al. 2010). However, recent simulations also find mergers are insignificant for driving black hole growth, except for $z \gtrsim 2$ where the expected higher merger rates come into play (Steinborn et al. 2018). With merger-driven black hole growth potentially more significant at higher redshift, the role of mergers in growing $z \sim 6$ quasars cannot be ignored.

The question of SMBH growth is further complicated when considering larger scale effects, such as the growth of the host halo itself and the potential co-evolution of the black holes with their host galaxies. Within halos where DCBHs are predicted to form, the conservation of angular momentum will result in the

formation of proto-galactic discs (Oh & Haiman 2002). These can then be fed by the accretion onto the host halo from cold gas streams (Dekel et al. 2009). Gas that is not depleted through star formation will still have to lose angular momentum efficiently to feed any black hole growth. As already stated, merger events can drive gas inflow through the efficient transport of angular momentum (Barnes & Hernquist 1996; D'Onghia et al. 2006; Hopkins et al. 2009). Processes internal to the disc can also result in gas inflow. Given the right circumstances, gravitational instabilities are thought to be capable of efficiently driving the inflow of material in self-gravitating discs (Toomre 1964; Rice et al. 2005). Indeed, different models of galactic discs have shown gravitational instabilities are capable of providing inflow which supports black hole growth (Lodato & Natarajan 2006; Devecchi et al. 2010; Hopkins & Quataert 2011; Anglés-Alcázar et al. 2015).

In this study I model the growth of a black hole and its host galaxy from the formation redshift of the seed black hole to $z \sim 6$. Building on the model discussed in Chapter 2 I investigate how the growth of seed black holes can be limited by the inflow of gas through a growing viscous (proto-)galactic disc. I model the inflow rate from a viscous disc and show how the flow is a function of overall gravitational stability of the disc. I neglect energetic feedback effects and focus on predicting upper limits to the possible feeding of black holes through viscosity driven gas inflow. I start in Section 3.2 by introducing the model and describing how the inflow rate of gas from the disc onto the black hole is estimated using the two extreme situations of a conservative and optimistic inflow rate in the viscous disc. Section 3.3 describes the consequences of the inflow rate on the growth of the black hole and investigates how the final mass of the black hole depends on the model parameters. In Section 3.4 I demonstrate how mergers can resolve the otherwise apparent discrepancy between observations and our upper estimate in the black hole mass at $z = 6$. Finally, I summarise the findings and discuss the implications for the sites of massive seed formation and the evolution of SMBHs hosts in Section 3.5.

3.2 Methodology

The methodology presented here builds on the model discussed in Chapter 2 which focuses on the growth of a proto-galaxy in an atomic cooling halo, modelled as an isothermal sphere, that is free of molecular hydrogen due to a high intensity LW-background and with a DCBH at the centre. Here we discuss briefly that

model and outline the changes made in undertaking this study.

3.2.1 Halo growth

The model initial conditions place a massive black hole ($M_\bullet = 10^{4-6}\,\mathrm{M}_\odot$) at the centre of a proto-galactic disc at some formation redshift, $z_\mathrm{i} \sim 20 - 10$, within a $T_\mathrm{vir} = 8000$ K dark matter halo. The disc mass is calculated at any point from the baryon mass of the halo once the black hole mass is subtracted, assuming the universal baryon fraction $f_\mathrm{b} = 0.17$ in the halo ($M_\mathrm{d}(t) = f_\mathrm{b}\, M_\mathrm{h}(t) - M_\bullet(t)$). The disc is assumed to be isothermal with a gas temperature of $T_\mathrm{g} = 8000$ K, consistent with the absence of molecular cooling in primordial gas. The system is then allowed to grow with the halo and disc growth being fed through cosmological accretion with halo growth rate parametrised by ζ.

$$\frac{dM_\mathrm{tot}}{dz} = -\zeta M_\mathrm{tot} \tag{3.1}$$

The mean halo growth rate from ΛCDM provides our fiducial value of $\langle\zeta\rangle = 0.806$ (Neistein & Dekel 2008). Using the scatter in the growth rate of dark matter halos from Genel et al. (2008), the standard deviation in ζ can be calculated as $\sigma_\zeta = \langle\zeta\rangle(2.5/(1+z))^{0.2} = 0.656$ at $z = 6$ by assuming the growth rate is a linear function of the halo mass. $\langle\zeta\rangle + \sigma_\zeta = 1.462$ is taken as an extreme upper bound. A further constraint is placed on the maximum growth rate of our model haloes from the known number density of massive quasars at $z \sim 6$ of around $\phi \sim 1\,\mathrm{Gpc}^{-3}$ (Fan et al. 2003). This number density corresponds to haloes with masses $M_\mathrm{tot} \geq M_\mathrm{tot,\,lim} \approx 10^{13}\,\mathrm{M}_\odot$ (Sheth et al. 2001; Murray et al. 2013). Thus we can calculate for a given z_i (and corresponding atomic cooling halo mass) the halo growth rate, $\zeta_\mathrm{max}\,(z_\mathrm{i})$, which will result in $M_\mathrm{tot} = M_\mathrm{tot,\,lim}$. At higher halo growth rates with $\zeta > \zeta_\mathrm{max}\,(z_\mathrm{i})$, the halo mass at $z = 6$ will be higher $M_\mathrm{tot} > M_\mathrm{tot,\,lim}$ and the abundance of such haloes would be lower than the abundance of SMBHs. As we are only considering the seeding of SMBHs, ζ_max provides a further upper constraint to the halo growth rate for earlier formation times ($z_\mathrm{i} \sim 20 - 15$). Note the direct mapping used between ζ and the total halo mass $M_\mathrm{tot}(z = 6)$ for a given z_i.

Agarwal et al. (2016b) modelled the growth history of DCBH host candidate, CR7 (Sobral et al. 2015; Bowler et al. 2017) and found mass assembly histories for the each of the subhaloes in the model. By fitting an exponential to the

median subhalo mass at each whole number redshift, we find a halo growth rate parameter of $\zeta_{\rm CR7} = 0.568$ which is taken as the lower bound.

3.2.2 Disc instability and inflow rates

Gravitational instabilities in discs can drive angular momentum transport and the inflow of material (Toomre 1964). Disc instability is often parametrised using the Toomre-Q parameter.

$$Q = \frac{\sigma\kappa}{\pi G\Sigma} \tag{3.2}$$

where σ is the velocity dispersion, which we assume in this study to be dominated by the gas sound speed, $c_{\rm s}$, and Σ is the total surface density given by the radial profile. For simplicity, the gas and stellar components are assumed to follow the same profile, $\Sigma(R) = \Sigma_0 \exp -R/R_{\rm d}$. As the dark matter halo profile is modelled as an isothermal sphere, the disc scale radius, $R_{\rm d}$, scales with the virial radius of the halo and the spin parameter, λ (Mo et al. 1998). Throughout this study $\lambda = 0.05$ is assumed, corresponding to the mean (Mo et al. 1998). The epicyclic frequency, κ, measures the differential rotation and is a function of the radial profile of the angular frequency, $\Omega(R)$. It can be expressed as the following:

$$\kappa = 2\Omega\sqrt{1 + \frac{1}{2}\frac{d\ln\Omega}{d\ln R}} \tag{3.3}$$

The star formation rate can be calculated using the same method as in the previous chapter (Chapter 2) in the region of the disc where $Q < 1$. However, rather than the stellar mass remaining where it forms in the disc, the stellar surface density is assumed to follow the exponential radial profile at all times. This does not significantly impact the total stellar mass of the disc however it will change how the stability of the disc varies with radius.

Generally, mass transport in discs is described using some viscosity, $\nu = \alpha_\nu c_{\rm s} H$, where $c_{\rm s}$ is the disc sound speed in the mid-plane, $H \sim c_{\rm s}/\Omega$ is the disc scale height, and α_ν is the viscosity parameter. α_ν acts as an efficiency parameter which must account for the physical mechanism behind the viscosity. The viscosity parameter has been determined through observations of discs in various physical scenarios (King et al. 2007) with a range of $0.1 \leq \alpha_\nu \leq 0.4$. Traditionally,

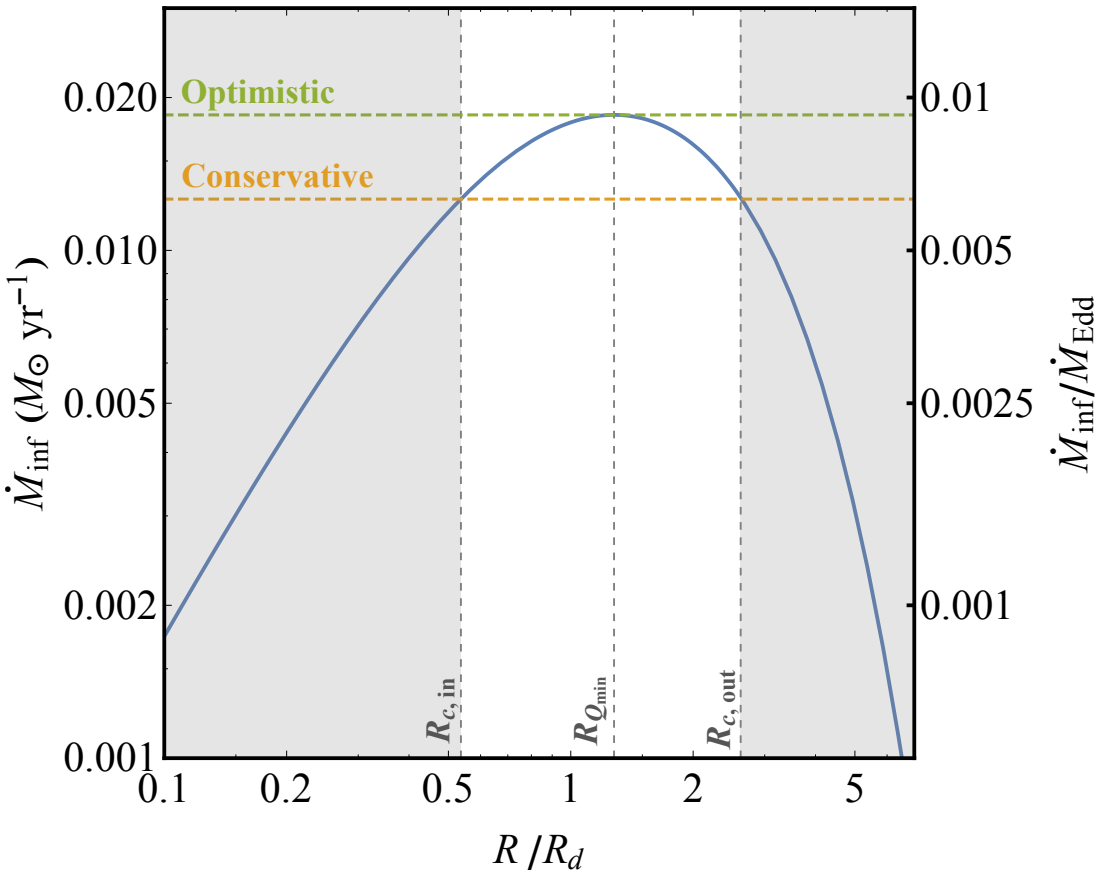

Figure 3.1 *The inflow rate of gas as a function of radius in a* $M_{\rm d} \sim 10^8\,{\rm M}_\odot$*, gaseous disc centred on a* $M_\bullet = 10^8\,{\rm M}_\odot$ *black hole. The radius is shown as a fraction of the disc scale radius (*$R_{\rm d} = 40$ *pc). The greyed out regions show the portions of the disc where* $Q > 1$*. The blue line shows the inflow rate while the horizontal, green and orange dashed lines show the optimistic and conservative inflow rates respectively. The vertical dashed lines from left to right indicate the radii where* $Q = 1$*,* $Q = Q_{\rm min}$*, and again* $Q = 1$*. The right hand vertical axis shows the inflow rate as a fraction of the Eddington growth rate onto the black hole.*

this parameterisation is used when considering viscosity driven by magneto-hydrodynamic instabilities (Shakura & Sunyaev 1973). However, it is unclear whether the required magnetic fields are prevalent in the first galaxies (however see, Koh & Wise 2016). Some have argued that when considering self-gravitating discs, the viscosity comes from gravitational instability driven turbulence (Lin & Pringle 1987, 1990; Lodato 2007). Studies of self-gravitating discs suggest inflow with $\alpha_\nu \gtrsim 0.06$ should result in the formation of clumps and the disruption of the transport of mass inwards (Rice et al. 2005; Lodato & Natarajan 2006). Previously, studies of Mestel discs ($\Sigma(R) = \Sigma_0$) have related α_ν to the global Toomre-Q parameter (Lodato 2007; Devecchi & Volonteri 2009; Devecchi et al. 2010). Here, an exponential profile is centred on our point mass black hole, both resulting in κ and Q being functions of R. The relationship between a global α_ν and $Q(R)$ in this setting becomes unclear as Q is now a local quantity. For purposes of this study, I investigate a range of $\alpha_\nu = 0.001 - 0.4$, bearing in mind that a decrease in α_ν will only act to decrease the inflow rate.

The inflow rate of gas in the disc as a result of this viscosity is defined as,

$$\dot{M}_{\rm inf} = \frac{\alpha_\nu c_{\rm s}^2 \pi \Sigma_{\rm g}}{2\Omega} \left| \frac{d \ln \Omega}{d \ln R} \right| \tag{3.4}$$

where $\Sigma_{\rm g}$ is the gas surface density. For a gaseous disc, this can then be rearranged to be a function of the Toomre-Q parameter:

$$\dot{M}_{\rm inf} = \frac{\alpha_\nu c_{\rm s}^3}{G} \frac{1}{Q_{\rm g}} \left| \frac{d \ln \Omega}{d \ln R} \right| \sqrt{1 + \frac{1}{2} \frac{d \ln \Omega}{d \ln R}} \tag{3.5}$$

As the inflow rate described by equations 3.4 and 3.5 has a radial dependence (see Figure 3.1), to avoid calculating the full evolution of the disc profile we must make an estimate for the inflow rate from the disc to centre of the galaxy. Though the gradient of the angular frequency ($d \ln \Omega / d \ln R$) does vary with radius and $M_\bullet / M_{\rm d}$, it remains $\sim \mathcal{O}(-1)$ with $-2/3 \gtrsim d \ln \Omega / d \ln R \gtrsim -3/2$ for our setup. The largest contribution to the radial variation therefore comes from the profile of $Q_{\rm g}$. This leads to the inflow rate peaking at a radius roughly equivalent to the radius at which the stability parameter is minimised, i.e. where the disc is most unstable. If the effective inflow rate of the disc is determined to be the value of $\dot{M}_{\rm inf}$ where Q is minimised with respect to R, this is roughly an upper limit on the rate at which a central gas reservoir can be fed from accretion in the galaxy

Table 3.1 *Table of model parameters varied in this study.*

Parameter	Definition	Fiducial (Range)
α_ν	viscosity parameter	0.06 $(0.06 - 0.4)$
$M_{\rm seed}$	black hole seed mass	10^6 (10^{4-6}) $M_\odot$
$z_{\rm i}$	seed formation redshift	20.0 $(20.0 - 10.0)$
ζ	halo growth rate	0.806 (0.586, 0.806, 1.462) [2]

disc. We take $\dot{M}_{\rm inf}(R_{Q_{\rm min}})$ to be an estimate for the upper limit on the inflow rate and therefore refer to it as the optimistic inflow rate. This is indeed an upper limit estimate as a full calculation of the profile where Equation 3.5 is used to calculate $\dot{M}_{\rm inf}(R)$ would result in a flattening of the surface density profile in the unstable region (as the mass flows inwards), raising Q and lowering the inflow rate.

Inflow is calculated within the region where the disc is unstable to the gravitational instabilities which are driving the viscosity (i.e. for R where $Q < 1$). For gas to reach the centre of the disc, the inflow needs to continue down to $R << R_{\rm d}$. As the full evolution of the disc profile is not calculated here, it is assumed that inflow is able to continue at smaller radii by maintaining an equilibrium of sorts, whereby the inflow rate at the inner $Q = 1$ radius is balanced by the inflow rate into the gravitational sphere of influence of the black hole. We can therefore use the inflow rate at the inner radius where $Q = 1$, $R_{\rm c,in}$, as our conservative inflow rate. This is a conservative lower limit estimate as only lower inflow rates would be determined if $\dot{M}_{\rm inf}(R \sim R_\bullet)$ was used (though $R = R_\bullet$ is outside of the $Q < 1$ region). Note this does not influence the main findings of this study for which the focus is more on the optimistic inflow rate. The optimistic and conservative estimates of the inflow rate are shown on Figure 3.1 by the green and orange dashed lines respectively.

3.2.3 Black hole growth

The black hole is fed by gas from a reservoir with mass, $M_{\rm res}$, which is itself fed from the inflow of the disc. The mass of the reservoir is thus determined by the

[2] A further constraint on the growth rate comes from requiring the halo mass at $z = 6$ corresponds to a number density higher than 1 $\rm Gpc^{-3}$ on the halo mass function. This constraint depends on $z_{\rm i}$.

balance of the inflow rate and the accretion rate of the black hole, $\dot{M}_\bullet$, giving:

$$\dot{M}_{\rm res} = \dot{M}_{\rm inf} - \dot{M}_\bullet \tag{3.6}$$

The reservoir is assumed to be under the direct gravitational influence of the black hole. With this, the accretion rate of the black hole can be calculated from the mass available in the gas reservoir via,

$$\dot{M}_\bullet = {\rm Min}\left[\frac{M_{\rm res}}{t_{\rm acc}} = \varepsilon\frac{M_{\rm res}}{t_{\rm dyn}},\ \dot{M}_{\rm Edd}\right] \tag{3.7}$$

where $\dot{M}_{\rm Edd} = M_\bullet/t_{\rm Sal}$ is the Eddington limit accretion rate, $t_{\rm Sal} \sim 0.05$ Gyr is the Salpeter timescale with 10% radiative efficiency (King et al. 2008), and $t_{\rm acc} = t_{\rm dyn}/\varepsilon$ is the accretion timescale with the efficiency parameter $\varepsilon < 1$. The value of ε is largely unknown but note that generally it does not determine the growth history of the black hole which is largely controlled by the inflow rate feeding the reservoir (see below). The timescale is determined at the radius of the sphere of influence of the black hole, $R_\bullet$, i.e. $t_{\rm dyn} = 1/\Omega\left(R_\bullet\right)$, where Ω is the angular velocity. Inside this radius the mass of the black hole will dominate the potential and any material will eventually be accreted onto the black hole subject to the loss of angular momentum[3]. $R_\bullet$ is calculated as the radius at which the gravitational potential due to the black hole balances that of the halo and the thermal energy of the disc,

$$R_\bullet = \frac{GM_\bullet}{c_{\rm s}^2 + V_{C,\,h}^2} \tag{3.8}$$

where $c_{\rm s}$ is the sound speed of the gas in the disc and $V_{C,\,h}$ is the circular velocity due to the gravitational potential of the halo.

If no limit is imposed on the growth of the black hole, such as Eddington limit in Equation 3.7, one can take advantage of the short accretion timescale to make a simplification to the model. The black hole is able to grow via an accretion disc which exists within the sphere of influence of the black hole. The scale of the accretion disc is therefore significantly smaller than galactic disc scales,

[3] $R_\bullet$ does not significantly affect our findings as $R_{\rm c,in} >> R_\bullet$ (see Chapter 2), and thus the inflow that feeds the reservoir, which primarily determines the evolution of the black hole (see Section 3.3), will occur over longer timescales and is independent of $R_\bullet$.

and the inflow of material from gravitational instabilities in the galactic disc are not directly feeding the black hole. However, to stringently test the capability of viscosity driven inflow to feed the growth of massive black holes, it can be assumed that the inflow from the disc is able to directly feed the black hole (i.e. $\dot{M}_\bullet = \dot{M}_{\rm inf}$). With this simplification, one can calculate an upper limit on black hole growth fed via viscosity driven inflows. As the accretion timescale is much shorter than the infall timescale, using the simplification $\dot{M}_\bullet = \dot{M}_{\rm inf}$ will not significantly impact the growth of the black hole in the model.

I stress this simplification cannot be made where the accretion timescale from the reservoir would be longer than the inflow timescale, such as when limiting the growth by the Eddington rate or for very small values of ε. As the focus is on calculating an upper limit for black hole growth this does not affect the main findings, however, whenever the Eddington limit is imposed in a model, the reservoir is included in the calculation.

3.3 Results

3.3.1 Inflow rate in the disc

The inflow rate is strongly dependent on both the absolute and relative masses of the disc and black hole. Figure 3.2 shows the optimistic and conservative inflow rate estimates as a function of the disc and black hole masses. The dark matter halo mass scaled with the total baryon mass ($M_{\rm b} = M_{\rm d} + M_\bullet$) so that the baryon fraction $f_{\rm b} = 0.17$ holds. The optimistic inflow rate estimate (top left panel of Figure 3.2) strongly depends on the disc mass while the conservative is more dependent on the black hole mass (top right). On each panel, the dashed black line shows where $Q_{\rm min} = 1$; below this line the disc is fully stabilised and no inflow can occur. At high black hole masses ($M_\bullet \gtrsim M_{\rm d}$), the disc becomes influenced by the gravitational potential of the black hole and is therefore more stable. This means the mass of the disc required for inflow to be possible is higher at high black hole masses. Indeed the optimistic inflow rate becomes more dependent on the black hole mass at higher black hole masses. However, as the inflow rate is defined at $R = R_{Q_{\rm min}} \sim R_{\rm d}$ and the black hole's sphere of influence is generally small ($R_\bullet << R_{\rm d}$), the disc mass largely determines the inflow rate. The conservative inflow rate estimate is more dependent on the black hole mass

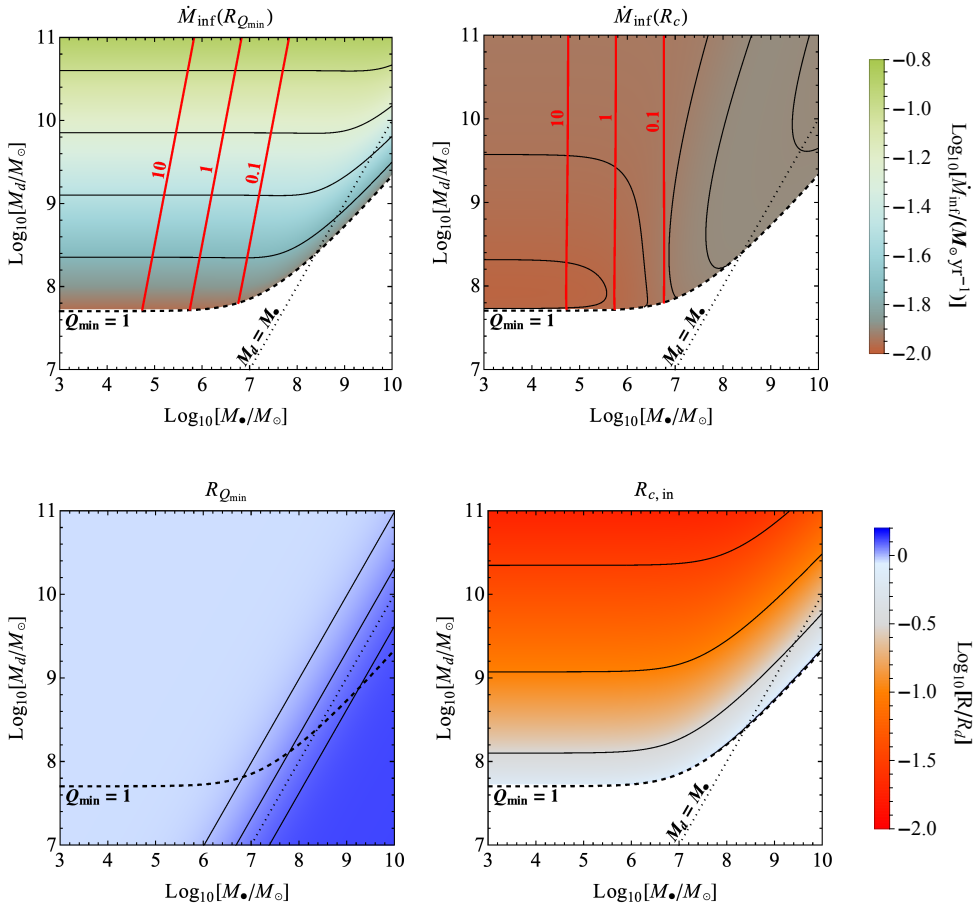

Figure 3.2 *As a function of disc and black hole mass each panel shows the following: the top row shows the inflow rate of gas from the disc onto the reservoir of gas which feeds the black hole (the red lines indicate different values of* $\dot{M}_{\rm inf}/\dot{M}_{\rm Edd}$ *as indicated by the red labels, i.e. the* $\dot{M}_{\rm inf}/\dot{M}_{\rm Edd} = 1$ *line shows where the inflow rate goes from super-Eddington to sub-Eddington from left to right). The top left panel shows the optimistic inflow rate i.e. the rate where the disc is most unstable (at* $R = R_{Q_{\rm min}}$*). The top right panel shows the conservative inflow rate i.e. the rate where the disc is only marginally unstable (at* $R = R_{Q=1}$*). The bottom left and right show the values for these radii. In each case the dark matter halo mass scales with the baryon mass (*$M_{\rm b} = M_{\rm d} + M_\bullet$*) so that* $f_{\rm b} = 0.17$ *and* $R_{\rm d}$ *scales with the virial radius of the halo (Mo et al. 1998). The inflow rate is determined using the fiducial value for the viscosity parameter* $\alpha_\nu = 0.06$ *(note this is just a constant factor in* $\dot{M}_{\rm inf}$*). The thick dashed line shows where* $Q_{\rm min} = 1$*, i.e. above this line the disc is partly unstable and inflow can occur. Note, that the slight dependence of the conservative accretion rate on the black hole mass is a result of the small variation in* $d\ln\Omega/d\ln R$*. The dotted line on each panel indicates the* $M_{\rm d} = M_\bullet$ *line.*

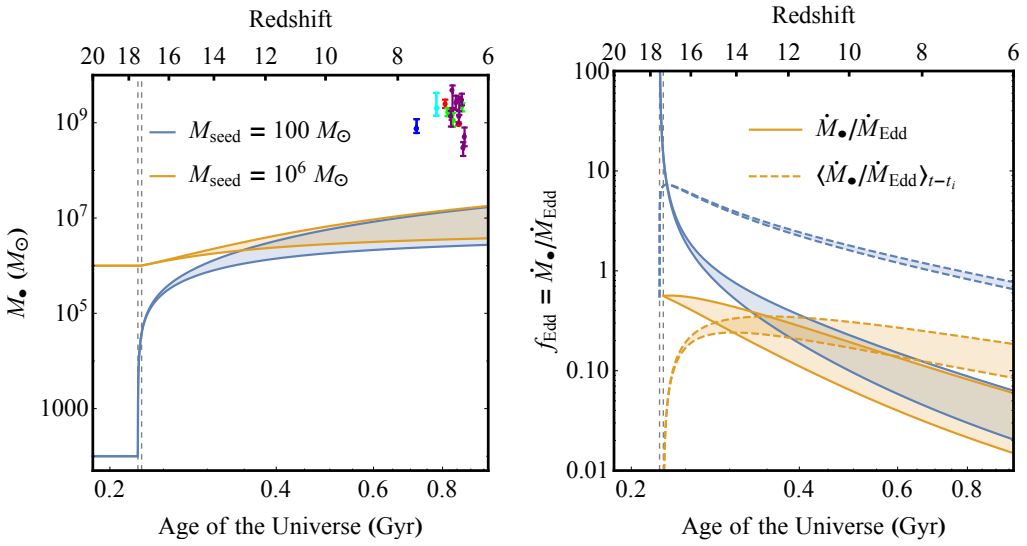

Figure 3.3 *The growth history of the black hole and the gas reservoir which feeds the black hole for the fiducial model with seeds of initial masses* $M_{\rm seed} = 10^6\,{\rm M}_\odot$ *and* $M_{\rm seed} = 100\,{\rm M}_\odot$*, which form at* $z_{\rm i} = 20$*. The other model parameters are set to their fiducial (see Table 3.1) and the black hole accretion rate was not capped by the Eddington limit. The possible growth histories are shown as the shaded regions between the curves calculated using* $\dot{M}_{\rm inf}(R_{Q_{\rm min}})$ *and* $\dot{M}_{\rm inf}(R_{\rm c,\,in})$ *as the upper and lower estimates for the inflow rate onto the gas reservoir respectively. Each panel shows the following: Left: The evolution of the mass of the black hole. The coloured data points are from observations of high-redshift quasars (cyan: Mortlock et al. (2011), red: De Rosa et al. (2014), purple: Mazzucchelli et al. (2017), blue: Bañados et al. (2018), green: Reed et al. (2019)). The vertical dotted lines indicate the times at which the disc first becomes unstable (*$Q_{\rm min} < 1$*). In the lower seed mass case this is reached marginally earlier. Right: The evolution of the growth rate onto the black hole as a fraction of the Eddington limit. The Eddington fraction averaged over the time since formation,* $t - t_{\rm i}$ *(see Equation 3.9), is also shown using the regions bound by the dashed curves.*

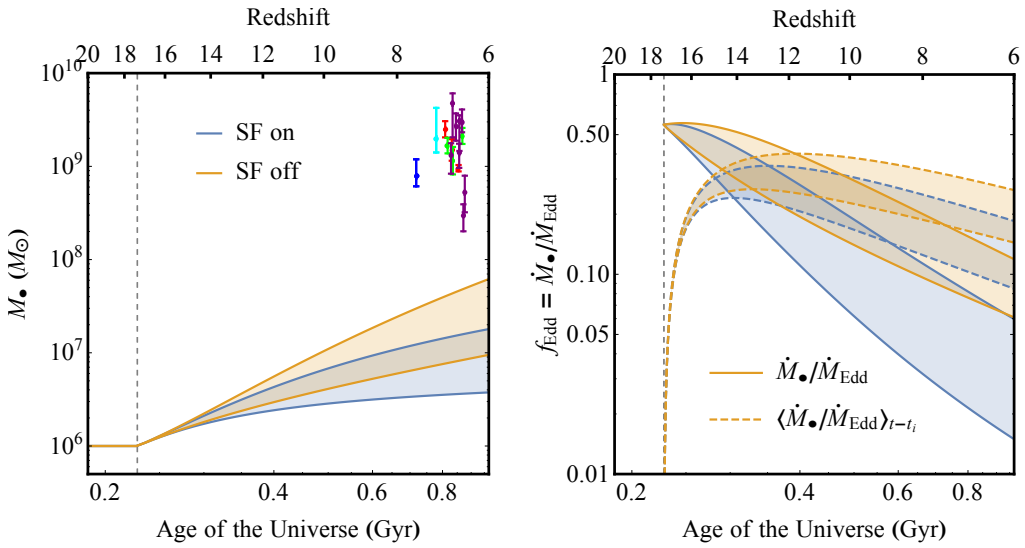

Figure 3.4 *As in Figure 3.3 except the evolution for a* $M_{\rm seed} = 10^6\,{\rm M}_\odot$ *seed is shown for both with and without star formation included in the model (corresponding to SF on and SF off, respectively). The other model parameters are set to their fiducial values (see Table 3.1).*

as the radius $R_{\rm c,in}$ is closer to the black hole and thus more influenced by the central mass.

The red lines in the top panels of Figure 3.2 show where the disc inflow rate is equal to 0.1, 1, and 10 times the Eddington accretion limit of the black hole. To the left of the $\dot{M}_{\rm inf}/\dot{M}_{\rm Edd} = 1$ line the inflow rate is greater than the Eddington limit. To the right, the inflow rate is lower than the Eddington limit and thus supply to the reservoir the limiting factor in the growth of the black hole. Indeed, if a system is consistently to the right of the Eddington limit line (as will be the case for massive seeds with $M_{\rm seed} \sim 10^6\,{\rm M}_\odot$), the Eddington limit will not be reached during the evolution. For lower mass seeds ($M_{\rm seed} \sim 10^3\,{\rm M}_\odot$), the system will initially be to the left of this line but as the black hole will become more massive at later times, its growth will also be eventually limited by the growth of the reservoir. This indicates that for higher black hole accretion rates ($\dot{M}_\bullet \gtrsim \dot{M}_{\rm Edd}$) the inflow rate onto the gas reservoir is the more significant factor in determining the growth of a seed black hole, rather than the black hole accretion timescale.

3.3.2 Black hole seed masses

Figure 3.3 shows the evolution of the fiducial model but with two different black hole seed masses $M_{\rm seed} = 10^6\,{\rm M}_\odot$ and $M_{\rm seed} = 100\,{\rm M}_\odot$. In each case the growth of the black hole is not capped at the Eddington rate and the growth rate of the black hole is effectively independent of the initial seed mass. Indeed, the black hole masses are roughly comparable following an initial period of super-Eddington accretion in the case with the lower mass seed. It is important to note in this case that, had the Eddington limit been implemented, it would not have changed the final black hole mass at $z = 6$. The time-averaged Eddington fraction is calculated using the following:

$$\langle \dot{M}_\bullet / \dot{M}_{\rm Edd} \rangle_{t-t_{\rm i}} = \ln \left[\frac{M_\bullet}{M_{\rm seed}} \right] \frac{t_{\rm Sal}}{t - t_{\rm i}} \tag{3.9}$$

In both cases, $\langle \dot{M}_\bullet / \dot{M}_{\rm Edd} \rangle_{t-t_{\rm i}} < 1$ at the end of the calculation (shown by the dashed-line bounded regions in Figure 3.3c). As feedback effects are not modelled, this means the final black hole masses at $z = 6$ would have been the same had the black hole growth been capped at the Eddington limit.

The black hole seed mass does not play a role in determining the long term growth history of the black hole in our model. However, this ignores the effects of AGN feedback. With feedback effects included, the growth of the black hole would be more stunted due to the resulting outflows (Johnson et al. 2011; Latif et al. 2018). This could be particularly dramatic in the lower mass seed case as relatively more rapid growth is required and this would drive more energetic feedback.

3.3.3 Star formation

Star formation has the effect of slowing down the growth of the black hole. Though feedback effects are not modelled, star formation and black hole growth are both fed from the gas content of the disc and they are therefore in competition over the same gas supply. Figure 3.4 shows how the black hole growth in our fiducial case is changed when star formation is not included. When star formation is "turned off", the final mass of the black hole increases as the higher gas fraction means the total mass that reaches the black hole is higher. After the initial onset of star formation in the fiducial case, the case with no star formation

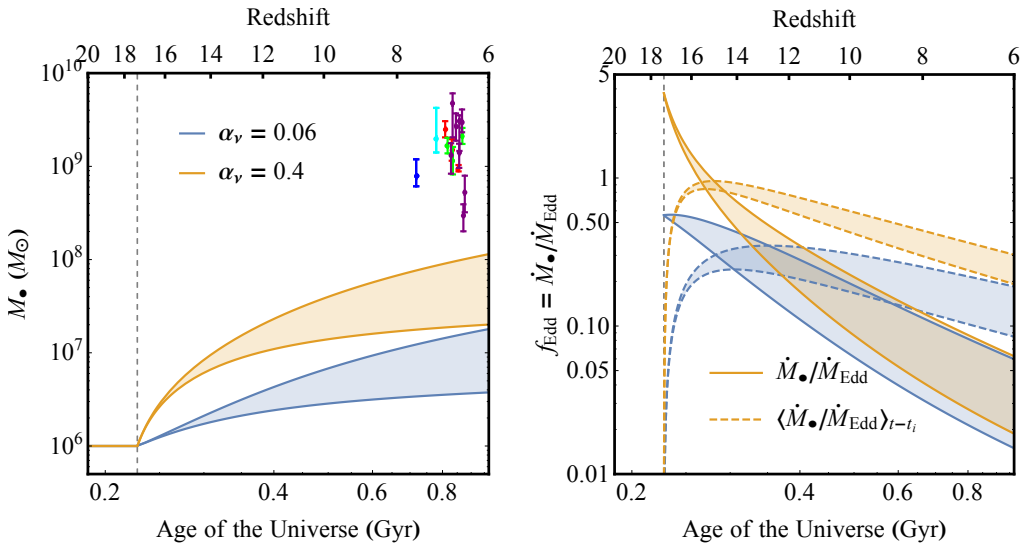

Figure 3.5 *As in Figure 3.3 except the evolution for a* $M_{\rm seed} = 10^6\,{\rm M}_\odot$ *seed is shown with two values for the disc viscosity parameter,* $\alpha_\nu = 0.06$ *and* $\alpha_\nu = 0.4$*, which determines the inflow rate onto the gas reservoir. The other model parameters are set to their fiducial values (see Table 3.1).*

maintains a higher black hole growth rate. This difference in the growth rate is first noticeable around $z = 15$ and as the model evolves it increases as the stellar disc fraction in the fiducial case increases to its highest value at $z = 6$ of around $M_\star/M_{\rm d} \sim 0.9$. Even in the absence of star formation the final black hole mass is only $M_\bullet = 6.18 \times 10^7\,{\rm M}_\odot$. The stellar mass (and stellar disc fraction) at $z = 6$ varies with the growth rate of the halo (see Chapter 2). When considering the extreme case where star formation is turned off in the model and the remaining parameters are chosen to create a best case scenario for black hole growth (taking the maximum inflow rate with $\alpha_\nu = 0.4$ with the earliest DCBH formation redshift $z_{\rm i} = 20$ and the corresponding maximum halo growth rate $\zeta = 0.940$), the black hole reaches a final mass of $M_\bullet = 6.95 \times 10^8\,{\rm M}_\odot$ with $\langle \dot{M}_\bullet/\dot{M}_{\rm Edd} \rangle_{t-t_{\rm i}} = 0.42$.

3.3.4 Viscosity limited black hole growth

With the optimistic inflow rate in our fiducial case, the final black hole mass at $z = 6$ is $M_\bullet = 1.80 \times 10^7\,{\rm M}_\odot$, more than 50 times smaller than the $M_\bullet \approx 10^9\,{\rm M}_\odot$ target.

Increasing the viscosity parameter of the disc does increase the inflow rate and thus black hole growth rate. Figure 3.5 compares the evolution of the black hole

masses for two values of the viscosity parameter, $\alpha_\nu = 0.06$ and $\alpha_\nu = 0.4$. With the higher disc viscosity the black hole is fed more rapidly and therefore can reach a higher mass estimate of $M_\bullet = 1.14 \times 10^8\,\mathrm{M}_\odot$. However, as discussed above, it is not clear that this higher viscosity parameter is applicable for galaxy discs as clumps are expected to form for $\alpha_\nu > 0.06$. Again in this scenario the Eddington limit does not affect the final mass of the black hole as $\langle \dot{M}_\bullet / \dot{M}_{\mathrm{Edd}} \rangle_{t-t_\mathrm{i}} < 1$ at the end of the calculation (shown by the dashed-line bounded regions in the right panel of Figure 3.5) for either value of α_ν.

Figure 3.6 shows how the final mass of the black hole varies with α_ν for three different halo growth rates ($\zeta = 0.568$, $\zeta = 0.806$, and $\zeta = \zeta_{\mathrm{max}}$), two seed masses ($M_{\mathrm{seed}} = 10^4\,\mathrm{M}_\odot$ and $M_{\mathrm{seed}} = 10^6\,\mathrm{M}_\odot$), and two seed formation redshifts ($z_\mathrm{i} = 20$ and $z_\mathrm{i} = 10$). ζ_{max} varies with the seed formation redshift so that the $\zeta_{\mathrm{max}} = 0.940$ for $z_\mathrm{i} = 20$ and $\zeta_{\mathrm{max}} = 1.462$ (1-σ above the average halo growth rate at $z = 6$) for $z_\mathrm{i} = 10$. At low values of the viscosity parameter ($\alpha_\nu < 0.005$), there is a significant difference in the final black hole mass for the different initial seed masses. This is simply because the growth of the black holes is weak, in the case of the highest initial seed mass, the seed takes up a significant fraction of that final black hole mass. This difference disappears in the higher halo growth rate case as the inflow rates are much higher. At higher α_ν the final mass is independent of the seed mass as the higher inflow rate means that the total mass accreted onto the reservoir (and then onto the black hole) is much greater than the initial mass of the black hole for either seed.

In the case with the lowest halo growth rate no $z_\mathrm{i} = 10$ curves are shown as the disc is never unstable in this scenario and therefore no inflow occurs. At higher halo growth rates ($\zeta = 0.806$, $\zeta = 0.940$ and $\zeta = 1.462$) the seed formation redshift is important in determining the maximum mass to which the black hole can grow. The final mass of the black hole is much lower for the $z_\mathrm{i} = 10$ cases. This is not only because there is much less time for the black hole to grow but, significantly, the halo mass at $z = 6$ decreases for lower z_i and thus the growth rate of the disc decreases. This comes from the halo mass at the seed formation redshift being set as the mass of an atomic-cooling halo with $T_{\mathrm{vir}} = 8000$ K at that epoch before growing at the rate determined by Equation 3.1.

The red region on each panel in Figure 3.6 indicates the range of masses of the quasars observed at $z > 6$ and the pink line indicates the average of these masses (Mortlock et al. 2011; De Rosa et al. 2014; Mazzucchelli et al. 2017; Bañados et al. 2018; Reed et al. 2019). In all cases the model cannot reach the observed

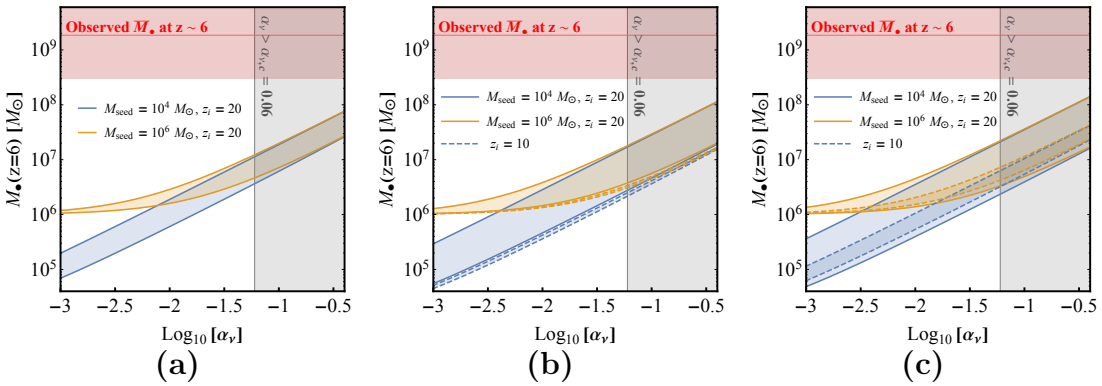

Figure 3.6 *The mass of the black hole at $z = 6$ as a function of the disc viscosity parameter, α_ν. Each panel shows the case for a different halo growth rate parameter, ζ (a) $\zeta = 0.568$, (b) $\zeta = 0.806$, and (c) $\zeta = \zeta_{\rm max}$ ($\zeta_{\rm max} = 0.940$ for $z_{\rm i} = 20$ and $\zeta_{\rm max} = 1.462$ for $z_{\rm i} = 10$). The possible final black hole masses are shown as the shaded regions between the curves calculated using the upper and lower estimates for the inflow rate onto the gas reservoir. The solid and dashed lines indicate the cases where the seed formation redshift is $z_{\rm i} = 20$ and $z_{\rm i} = 10$ respectively. The greyed out region at $\alpha_\nu > 0.06$ indicates the region where disc instabilities will limit the inflow rates significantly (Rice et al. 2005). The red region indicates the range of black hole mass observed at $z > 6$ with the solid pink line indicating the average of these masses (based on data from Mortlock et al. (2011), De Rosa et al. (2014), Mazzucchelli et al. (2017), Bañados et al. (2018) and Reed et al. (2019)). The remaining model parameters are set to their fiducial values (see Table 3.1).*

mass range, even with $\alpha_\nu = 0.4$.

3.3.5 Cosmic accretion limited growth

The growth rate of the halo determines the rate at which the disc can grow. Increasing the halo growth rate parameter will increase the accretion rate onto the disc. This in turn will increase the disc mass, making the disc more unstable and increase the resulting inflow rate in the disc. For a given formation redshift, $z_{\rm i}$, increasing the halo growth rate will increase the final halo mass at $z = 6$. Figure 3.7 shows evolution of the black hole and gas reservoir for two different values of the halo growth rate parameter, $\zeta = 0.586$ and $\zeta = 0.940$. In the $\zeta = 0.586$ case the lower halo growth results in a more stunted growth of the black hole with the maximum black hole mass estimate (using the optimistic inflow rate) at $z = 6$ is $M_\bullet = 1.22 \times 10^7 {\rm M}_\odot$. With a lower halo growth rate the star formation is less significant and therefore the conservative black hole

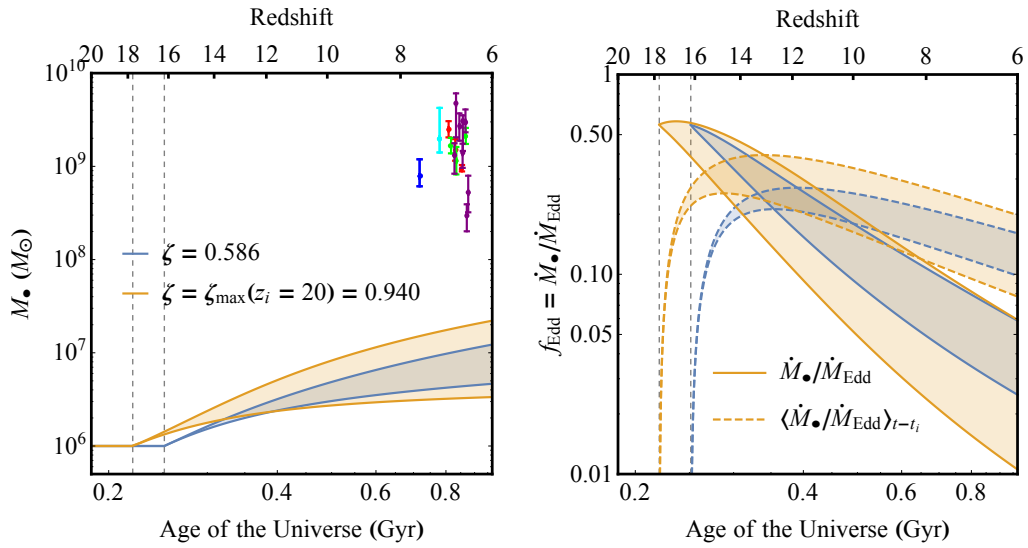

Figure 3.7 *As in Figure 3.3 except the evolution for a* $M_{\rm seed} = 10^6\,{\rm M}_\odot$ *is shown for two halo growth rate parameters,* $\zeta = 0.586$ *and* $\zeta = 0.940$*. The lower value of* ζ *mimics the growth rate of modelled DCBH hosting subhaloes (Agarwal et al. 2016b). The upper value corresponds to the growth rate required to grow atomic cooling haloes at the formation redshift* $z_{\rm i} = 20$ *into* $M \sim 10^{13}\,{\rm M}_\odot$ *haloes at* $z = 6$*. Haloes with this mass or above at* $z = 6$ *have an abundance of* $\phi \sim 1\,{\rm Gpc}^{-3}$ *(Sheth et al. 2001; Murray et al. 2013), matching the SMBH abundance (Fan et al. 2003). The other model parameters are set to their fiducial values (see Table 3.1).*

estimate is not as significantly stunted. At $\zeta = 0.940$, the disc mass grows more rapidly resulting in a higher inflow rate onto the reservoir and a higher growth rate of the black hole. The resulting maximum black hole mass estimate at $z = 6$ is larger at $M_\bullet = 2.21 \times 10^7 {\rm M}_\odot$.

The difference in minimum black hole mass estimates (corresponding to the conservative inflow rate) in Figure 3.7 is a result of the different stellar disc fractions. Increasing the growth rate of the halo will increase the disc mass at a given time, however, as the inflow rate does not change dramatically with the disc mass, the inflow rate does not change significantly other than due to the difference in the stellar disc fraction. As this fraction is lower in the lower growth rate case the minimum black hole growth rate is higher.

3.3.6 Halo growth rate versus viscosity parameter

The left panel of Figure 3.8 shows for the case of the optimistic estimate of inflow rate how the final mass of the black hole at $z = 6$ varies with α_ν and ζ for a $M_{\rm seed} = 10^6\,{\rm M}_\odot$ formed at $z_{\rm i} = 20$. As discussed previously, the final black hole mass increases with both α_ν and ζ. This results in a maximum value for $\zeta < 0.940$ of $M_\bullet = 1.42 \times 10^8\,{\rm M}_\odot$ ($M_\bullet = 6.95 \times 10^8\,{\rm M}_\odot$ without star formation).

The right hand panel of Figure 3.8 shows the time-averaged Eddington fraction for the black hole to grow from its seed mass to the final mass shown in the left hand panel. For $\zeta < 0.940$, this fraction is has a maximum of $f_{\rm Edd} \sim 0.32$ ($f_{\rm Edd} \sim 0.42$ without star formation), indicating that the final mass is limited by the total mass accreted onto the reservoir rather than the Eddington limit or efficiency of the black hole growth.

Within the range of the parameters for halo growth and inflow rates investigated here, there are no cases (with star formation implemented) where the black hole mass at $z = 6$ reaches the observed range of masses at this redshift with an average of $\bar{M}_\bullet = 1.85 \times 10^9\,{\rm M}_\odot$ (Mortlock et al. 2011; De Rosa et al. 2014; Mazzucchelli et al. 2017; Bañados et al. 2018; Reed et al. 2019). Note that if one neglects to include star formation and choses model parameters which create a best case scenario for black hole growth (taking the maximum, super-critical inflow rate with $\alpha_\nu = 0.4$, the earliest DCBH formation redshift $z_{\rm i} = 20$, and the corresponding maximum halo growth rate $\zeta = 0.940$), the black hole reaches a final mass of $M_\bullet = 6.95 \times 10^8\,{\rm M}_\odot$. If we ignore the upper limit placed on the halo mass at $z = 6$ by the observed SMBH abundance and use a halo growth rate parameter of $\zeta = 1.462$, the black hole reaches a maximum mass of $M_\bullet = 2.63 \times 10^8\,{\rm M}_\odot$. Note this extreme case is only mentioned here to illustrate the limitations on black hole growth in the model and should not be considered physically viable as the halo becomes overly massive. That is, it reaches a mass of $\sim 10^{16}\,{\rm M}_\odot$, while only $\mathcal{O}(1)$ halo with a mass $> 10^{13.2}\,{\rm M}_\odot$ should exist in the observable universe at $z = 6$.

3.4 Merger driven black hole growth

DCBHs are thought to form in close neighbours of massive star forming galaxies (see, e.g. Agarwal et al. 2014; Wise et al. 2019) that subsequently become

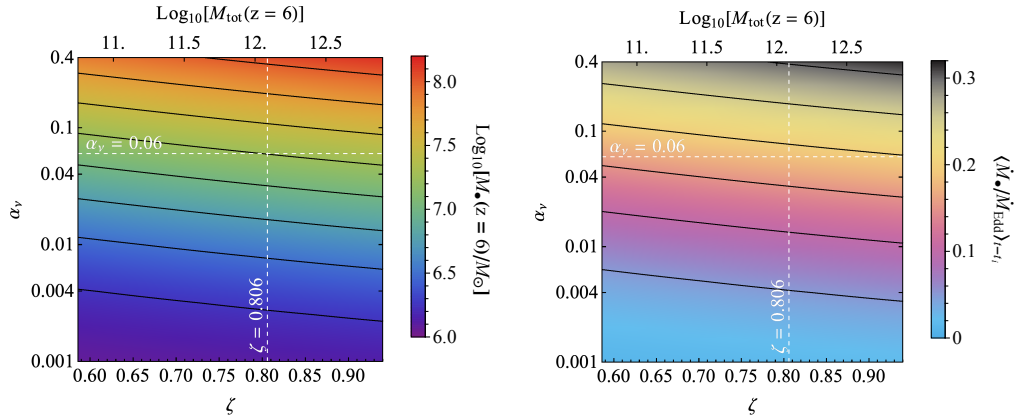

Figure 3.8 *The left panel shows the mass of the black hole at $z = 6$ as a function of the halo growth rate parameter, ζ, and the viscosity parameter, α_ν. The initial seed, with mass $M_{\rm seed} = 10^6\,{\rm M}_\odot$ forms at $z = 20$ and is fed using the optimistic inflow rate. The right panel shows the mean Eddington fraction required for the black hole to grow to the final mass indicated by the left panel. The horizontal and vertical, white, dashed lines correspond to the critical viscosity value $\alpha_\nu = 0.06$ (Rice et al. 2005) and the average halo growth rate parameter value $\zeta = 0.806$ (Neistein & Dekel 2008).*

satellites. This proximity means the DCBH host will eventually undergo a merger with a neighbouring halo, having a major impact on the evolution of the black hole (Dijkstra et al. 2008).

Galaxy merger events can be a major driver of angular momentum transport and therefore accretion (D'Onghia et al. 2006). Such events could therefore be responsible for driving gas accretion. Here the aim is to estimate the maximum capability of mergers to feed black holes.

Hopkins et al. (2009) argue that merger driven bar instabilities could cause the efficient loss of angular momentum for gas within the radius

$$\frac{R_{\rm mer}}{R_{\rm d}} \lesssim (1 - f_{\rm gas})\, f_{\rm disc}\, \frac{2\mu}{1+\mu}\, F(\theta, b, \mu) \tag{3.10}$$

$$F(\theta, b, \mu) \equiv \frac{\left(1 + (b/R_{\rm d})^2\right)^{-3/4}}{\left(1 + (b/R_{\rm d})^2\right)^{3/4} - \sqrt{2(1+\mu)}\cos\theta} \tag{3.11}$$

where μ is the merger mass ratio, b is the pericentric distance on the relevant final passage, θ is the inclination of the orbit relative to the disc plane, $f_{\rm disc}$ is the disc

mass fraction of the total mass enclosed in $R_{\rm d}$ and $f_{\rm gas}$ is the gas fraction in the disc. The dependence of $R_{\rm mer}$ on the merger orbital parameters, $F(\theta, b, \mu)$, varies strongly. As θ and b are not determined by our model, we take the mean value of $F(\theta, b, \mu) \sim 1.2$ from Hopkins et al. (2006) to calculate a typical disruption effect of a merger and as a maximum we assume the entire gas disc is disrupted (this scenario can be reached for different values of θ, b, and μ).

The gas enclosed in $R_{\rm mer}$ will become unstable and collapse efficiently towards the centre of the system with some fraction going into growing the reservoir which feeds the black hole. Here we take the extreme case where this fraction is unity and there is no starburst following the merger to give an upper limit on the possible black hole growth.

When a merger event occurs, $R_{\rm mer}$ is calculated using equations 3.10 and 3.11 and the gas mass inside this radius is taken from the disc and added to the gas reservoir over a dynamical time (taken as $t_{\rm dyn} = 1/\Omega$ at $R_{\rm d}$). During this time no star formation may occur.

For the parameter space investigated here, the stellar component of the disc reaches a maximum fraction of the disc mass of $f_\star \sim 0.9$. In this case the radius inwards of which the disc is disrupted by a typical merger event is small $R_{\rm mer}/R_{\rm d} \lesssim 0.2$. As a fraction of the total disc mass, the mass disrupted is only $\sim 1\%$ (giving a survival fraction of the disc of $f_{\rm sur} = 0.99$). However, the disruption radius is strongly dependent on the merger orbital parameters, θ and b, and the entire disc can be disrupted ($f_{\rm sur} = 0$) in one $1:1$ merger event. Figure 3.9 shows the evolution of the black hole mass for the two cases of mergers. For the typical merger, the disruption causes a jump in the available mass in the reservoir and the black hole mass rapidly increases by at least and order of magnitude to $M_\bullet \sim 10^8\,{\rm M}_\odot$. In the $f_{\rm sur} = 0$ case, however, the jump is much more dramatic with the black hole mass reaching $M_\bullet \sim 10^{10}\,{\rm M}_\odot$ if the growth is not limited by the Eddington rate. If the Eddington limit is introduced, the black hole mass at $z = 6$ is estimated between $M_\bullet \sim 1.5 \times 10^9\,{\rm M}_\odot$ and $M_\bullet \sim 5 \times 10^9\,{\rm M}_\odot$. This is an extreme case and is only shown to illustrate how a strong merger event can efficiently drive the growth of SMBHs.

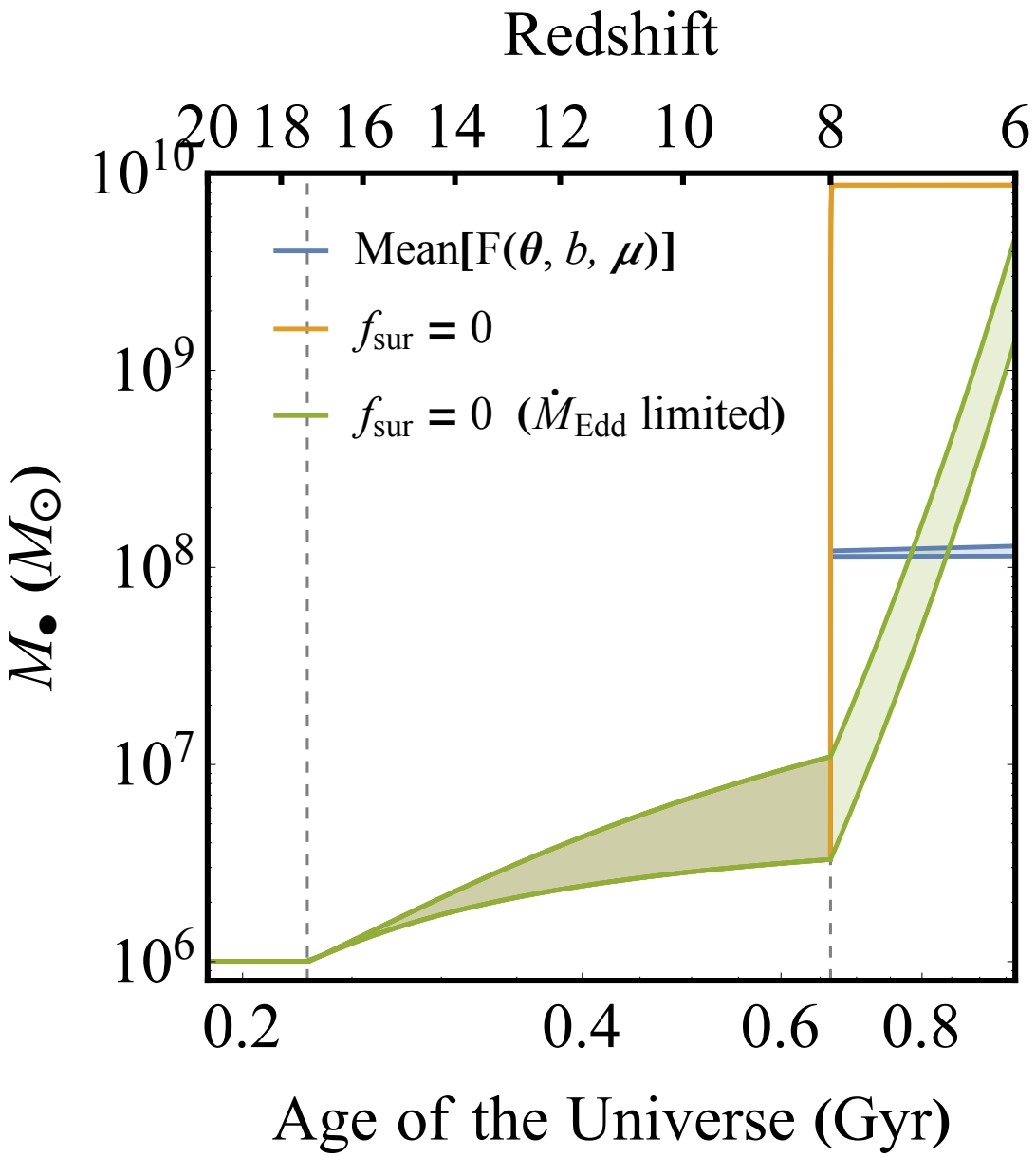

Figure 3.9 *The mass evolution of the black hole for the two merger events modelled here. The orange region shows the case where the disc is fully disrupted (i.e. the survival fraction of the disc is $f_{\rm sur} = 0$). The green region is the same ($f_{\rm sur} = 0$) except with the black hole growth limited at the Eddington rate. The blue region shows the case with the typical value for $F(\theta, b, \mu)$ (see Equations 3.10 and 3.11). In each case the merger is set to occur at $z = 8$. The black hole masses are shown as the shaded regions between the curves calculated using $\dot{M}_{\rm inf}(R_{Q_{\rm min}})$ and $\dot{M}_{\rm inf}(R_{\rm c,in})$ as the upper and lower estimates for the inflow rate onto the gas reservoir respectively. The vertical dashed lines represent, from left to right, the time when $Q_{\rm min} = 1$ and the time of the merger event. The model parameters in Table 3.1 are set to their fiducial values.*

3.5 Discussion & Summary

In this study I analytically model the idealised growth of massive seed black holes via the inflow of gas from growing proto-galactic discs. The inflow rate of gas in the disc is a function of the disc gravitational stability (Equation 3.5) and thus depends on the masses of both the disc and the black hole (Figure 3.2). I find that for a typical host halo, black hole growth is limited by the inflow rate, and that even in the absence of feedback effects high Eddington ratios ~ 1 will not be reached. Indeed, for the fiducial case I find an upper black hole mass estimate of $M_\bullet = 1.80 \times 10^7\,\mathrm{M}_\odot$ (Figure 3.3), indicating that viscosity driven accretion is too inefficient to feed the growth of seeds into $M_\bullet \sim 10^9\,\mathrm{M}_\odot$ SMBHs within the first billion years of the Universe.

If the growth rate of the black hole is not manually capped by the Eddington limit, the initial seed mass of the black hole has limited to no bearing on the mass the black hole can reach by $z \sim 6$ (Figure 3.3). However, in this calculation we have ignored the effects of feedback which drives outflows and can stunt black hole growth (Johnson et al. 2011; Dubois et al. 2015; Latif et al. 2018). With the inclusion of feedback effects and the resulting lower black hole accretion rate, the difference in the final mass of different seeds would likely be more significant.

I find that SMBHs can grow more easily in faster growing haloes, where the more massive discs that form are more gravitationally unstable and therefore inflow is stronger. Higher halo growth rates are expected in large σ-fluctuations of the cosmic density field in the Universe. However, the host halo masses in which a seed can grow to $M_\bullet \sim 10^9\,\mathrm{M}_\odot$ are less abundant than SMBHs at $z \sim 6$. When taking the $\phi \sim 1\,\mathrm{Gpc}^{-3}$ abundance of SMBHs (Fan et al. 2003) into account in matching the corresponding host halo mass, I find a maximum black hole mass at $z = 6$ of only $M_\bullet = 1.42 \times 10^8\,\mathrm{M}_\odot$ (with $\alpha_\nu = 0.4$ and $z_\mathrm{i} = 20$, see Figure 3.6). This strongly implies that the observed population of SMBHs at $z = 6$ did not grow steadily within isolated halos, and are not fed solely through viscosity driven inflow. Indeed, the physical process of black hole growth at high redshift is more complex. DCBHs are expected to form in haloes which will later become satellite subhaloes and will therefore likely experience low accretion rates. More rapid black hole growth should be expected during and following the merger of the DCBH host with a central galaxy. Major mergers provide the most promising avenue for SMBH growth through efficiently dissipating angular momentum and driving gas towards the black hole.

The inflow rate within the disc is modelled as viscosity driven accretion. The viscosity parameter, α_ν, was assumed to be a constant for each calculation, rather than calculating α_ν as a function of the gravitational stability of the disc (see, e.g. Devecchi et al. 2010). However, the fiducial value of $\alpha_\nu = 0.06$ should be seen as an upper limit as higher values lead to disc fragmentation (Rice et al. 2005). Our estimates of the inflow rate due to viscosity (and as a result black hole growth rates and final black hole masses) can therefore be considered conservatively large.

The inflow rates calculated here could be further overestimated as I do not directly consider the role of star formation in consuming the unstable fraction of the gas. If the inflow rate is above a critical value, the resulting fragmentation would lead to some fraction of the inflowing gas collapsing to form stars rather than feeding the black hole accretion (Lodato & Natarajan 2006; Devecchi et al. 2010). This has the potential then to limit the inflow onto the gas reservoir which feeds the black hole. The growth of the black hole is therefore potentially over-estimated.

An alternative to viscosity driven inflow is to model the torque exerted on a galactic disc from gravitational instabilities within the disc (Hopkins & Quataert 2011; Anglés-Alcázar et al. 2015). Hopkins & Quataert (2011) compared both the viscosity and gravitational torque driven accretion models to galaxy major merger simulations and found that inflow rates calculated using the viscosity model were under-estimated, while the gravitational torque model matched the simulations more closely. Calculating the inflow rate using the gravitational torque model would increase the accretion rate of the black hole however, this would depend more directly on the star formation calculation. The gravitational torque model successfully recreates the black-hole-galaxy scaling relations at lower redshift (Anglés-Alcázar et al. 2013; Davé et al. 2019).

Throughout this study I have modeled an isothermal disc. Decreasing the gas temperature either globally or locally would decrease the sound speed and the overall stability of the disc. As the model evolves, increasing gas densities and star formation will result in the introduction of more coolants to the gas, such as H^-, H_2, and metals. The gas can then cool efficiently to $T_{\rm gas} \sim 100$ K, leading to a decrease in the disc stability. The inflow rate goes as $\dot{M}_{\rm inf} \propto c_{\rm s}^2$ (see Equation 3.4) and as such the decrease in temperature would decrease the model inflow rate. Note however, the isothermal disc assumption would likely be no longer valid following the formation of these additional coolants.

In this study I have focused on haloes at the atomic cooling limit ($T_{\rm vir} \sim 10^4$

K). This provides the model with an initial halo mass at the redshift where the seed is assumed to have formed. However, if the formation were to take place at earlier times, $z_{\rm i} > 20$, a lower halo growth rate would be sufficient to reach the same halo mass at $z = 6$ or, similarly, with the same average growth rate a higher final halo mass would be reached. With higher halo masses, the model would find more massive discs, and potentially higher inflow rates feeding black hole growth. However, increasing the formation redshift does more to feed star formation than black hole growth. For example, with a formation redshift of $z_{\rm i} = 30$, an average halo growth rate ($\zeta = 0.806$) and a maximum viscosity ($\alpha_\nu = 0.4$), the black hole reaches only $1.93 \times 10^8\,{\rm M}_\odot$ by $z = 6$. This is ignoring the upper limit on the possible halo mass at $z = 6$ from the abundance of SMBHs, which is independent of the formation redshift. Furthermore, pushing the formation to higher redshifts would not be consistent with the DCBH formation mechanism. The high intensity LW-background necessary for DCBH formation is not available prior to the formation of the first luminous galaxies at around $z \sim 20 - 15$ (Springel et al. 2005b; Lacey et al. 2011; Agarwal et al. 2014). Indeed, studies have shown PopII stars are required to generate the required intensity of LW-background (see, e.g. Agarwal et al. 2012), pushing formation to lower redshifts.

Chapter 4

The dynamical heating of halo gas through the infall of massive black hole seed systems

4.1 Introduction

As we have discussed throughout the previous chapters of this thesis, direct collapse black holes (DCBHs) are strong candidates for the seeds of super-massive black holes (SMBHs) in the early universe at $z > 6$ (see review, Volonteri 2010). These massive seeds form from the isothermal collapse of pristine gas in haloes limited to atomic hydrogen cooling (Bromm & Loeb 2003; Begelman et al. 2006; Agarwal et al. 2012). With the absence of metals, a high-intensity of background UV photons can prevent gas from cooling below $T_{\rm gas} = 8000$ K by photo-dissociating any H_2 molecules and photo-detaching H^- ions, limiting gas fragmentation during the collapse to form a massive seed black hole (Shang et al. 2010; Agarwal et al. 2016a).

All of this makes haloes in close proximity to massive star forming galaxies in the early universe the ideal candidates for the hosts of DCBHs (Agarwal et al. 2014; Wise et al. 2019). This initial proximity means that any given DCBH host will likely become a satellite of their more massive neighbour (Dijkstra et al. 2008), leading to the infall of the DCBH host and the eventual galaxy merger.

Mergers are thought to potentially play a role in black hole growth at high

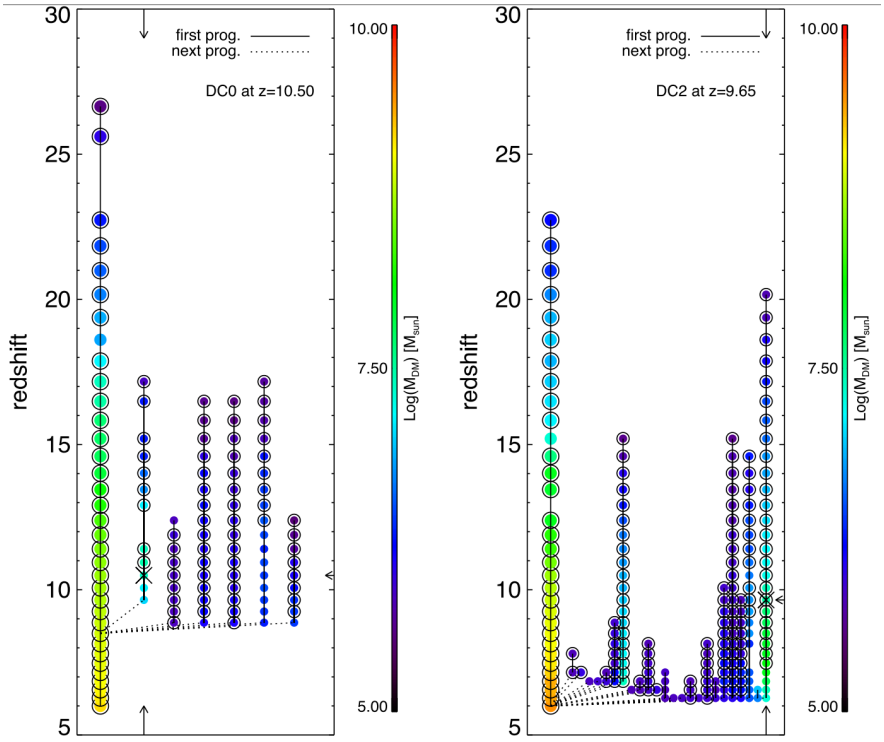

Figure 4.1 *Merger trees for two DCBH candidate haloes which proceed merge with more massive haloes, taken from Agarwal et al. (2014). "DCBH candidate haloes marked by the cross (use arrows to guide the eye). The left-branch represents the main progenitor branch of the halo with which the direct collapse candidate merges. On the right of this branch, we plot the merger history of the main progenitor halo with which the direct collapse candidate merges. Enclosing circles imply that the halo is the most massive halo within its friend of friends group. The haloes are colour coded by their dark matter mass."*

redshift and the development of the scaling relations observed in the local universe between black holes and their host galaxies (see, e.g. Di Matteo et al. 2005; Hopkins et al. 2009; Kormendy & Ho 2013). Indeed, studies have shown that the picture of isolated self-regulated growth (through feedback effects and/or the competition for gas from both black hole growth and star formation) can struggle to produce massive enough black holes to re-create the observed relations (Johnson et al. 2011; Latif et al. 2018; Smith et al. 2018, see also previous Chapters 2 and 3), while this discrepancy can be resolved by mergers (Lamastra et al. 2010, again see also Chapter 3). This indicates that massive black holes initially form in haloes where they dominate the baryonic mass before merging with their eventual host galaxies (see, e.g. Dijkstra et al. 2008; Agarwal et al. 2014) to potentially reach the observed scaling relations.

The time at which a DCBH host halo should fall in and eventually merge with

one of its more massive neighbours is unclear. The DCBH must form at $z_{\rm seed} \sim 10-20$, after the required background intensity of UV radiation has been provided by early star forming galaxies (e.g., Agarwal et al. 2012), but also prior to the infall at a lower redshift. The merger trees of the DCBH hosts from Agarwal et al. (2014) show the infall can occur at any time following DCBH formation (Figure 4.1, taken from Agarwal et al. 2014). In the two examples shown the infall occurs shortly after formation at $z \sim 9$ and at $z \sim 6$, where the authors end the calculation. The time of infall will strongly depend on the relative positions and velocities of the DCBH host and its neighbours.

Once the DCBH host reaches the virial radius of a more massive neighbour, it becomes a satellite halo and the infall process begins. The infall is driven by dynamical friction acting on the satellite from the gas and dark matter in the central halo. For near circular orbits, this gravitational drag force acts as a torque, decreasing angular momentum and causing the DCBH host to spiral inwards. At the same time, this friction will heat the surrounding central halo gas and dark matter halo (Ostriker 1999; Kim & Kim 2009). As I will show, the total energy released through dynamical friction throughout the infall process will be the change in the potential energy of the infalling subhalo with mass $M_{\rm p}$ as it moves from the virial radius, r_{200} to some final radius, $r_{\rm end}$, $\Delta E_{\rm DF} = \Delta E_{\rm pot} = V_{\rm c}^2 M_{\rm p} \ln\left(r_{200}/r_{\rm end}\right)$, where the circular velocity of the central halo, $V_{\rm c} \sim \mathcal{O}(100\,{\rm km/s})$ varies with the mass. If $r_{\rm end}$ is where the central galaxy density equals the average gas density then $\ln\left(r_{200}/r_{\rm end}\right) \sim \mathcal{O}(2)$. Compare this with the energy released in growing a black hole to a mass $M_\bullet$ through accretion (with a negligible seed mass), $\Delta E_{\rm acc} = \epsilon c^2 M_\bullet$ where c is the speed of light and $\epsilon \sim 0.1$ is the radiative efficiency. The black hole mass follows $M_\bullet = f_{\rm b} f_\star f_\bullet M_{\rm p}$, where the baryon fraction of the halo is less than the overall baryon fraction $f_{\rm b} \lesssim 0.17$ (Qin et al. 2017), the fraction of baryons that are stars varies with the age of the system $f_\star \sim 0.9 - 0.1$ (e.g. McGaugh & de Blok 1997), and the black hole to stellar mass ratio is $f_\bullet \sim 0.001$ (Kormendy & Ho 2013; Reines & Volonteri 2015). The ratio of the two energies is,

$$\frac{\Delta E_{\rm acc}}{\Delta E_{\rm pot}} = \frac{\epsilon\, c^2 f_{\rm b} f_\star f_\bullet}{V_{\rm c}^2 \ln\left(r_{200}/r_{\rm end}\right)} \tag{4.1}$$

The exact value of Equation 4.1 can vary greatly. With the rough values mentioned above this can be $\sim \mathcal{O}(100-1)$. If we consider that during an infall event, a black hole may only grow a small fraction of its mass, there could be a

period where the halo is heated primarily through dynamical friction.

In this study, we analytically model the infall of a DCBH host from the virial radius of a massive central halo to the point of merging with its eventual host galaxy. We investigate how the timescale over which this infall takes place and the energy released depend on the redshift at which infall takes place and the relative masses of the DCBH host subhalo and the central halo. We compare the energy generated through dynamical friction to the luminosity from the growth of the DCBH to study the significance of this heating. Finally, we comment on whether this picture of the merging of DCBH hosts with close-by massive galaxies can recreate the observed scaling relations in the local universe.

4.2 Model setup

The aim of this study is to follow the infall of a perturber onto massive, central halo to investigate the role of dynamical friction heating. We investigate two cases of a perturber: a DCBH host subhalo and a naked black holes. Here I summarise how the properties used as the initial conditions of the infall calculation, such as the masses and sizes of the haloes, are determined.

4.2.1 Black hole growth

The process of dynamical friction driven infall depends on, amongst other properties, the mass of the infalling perturber. For the case of a naked black hole (see below) we can model black hole growth to determine its mass at the time when infall occurs. In the case where the perturber is a DCBH-hosting subhalo, the black hole mass does not influence the process of infall. However, to test the significance of dynamical friction heating, we can compare it to heating through black hole accretion.

After the DCBH seed formed with a mass in the range of $M_{\rm seed} \sim 10^{4-6}\,{\rm M}_{\odot}$ at some earlier redshift, $z_{\rm i} \sim 20 - 10$, the black hole, and its host halo, are free to evolve in isolation until the infall begins at $z_{\rm infall}$. The mass growth of the black hole $M_{\bullet}(z)$ and its host $M_{\rm tot}(z)$ between $z_{\rm i}$ and $z_{\rm infall}$ can be modelled as shown in Chapters 2 and 3. Figure 4.2 shows the evolution of the black hole mass as a fraction of the total host mass for three models: Eddington limited

growth (as in Chapter 2, Equation 2.18 with $f_{\rm Edd} = 1$), viscosity driven inflow (as in Chapter 3, Equations 3.4 and 3.7), and gravitational torque driven inflow (Hopkins & Quataert 2011).

The first two models have already been discussed in the previous chapters of this thesis and it sufficient to note here that the Eddington limited growth model provides the strongest growth of the models shown here. Indeed, as the model assumes the black hole only accretes baryons, the mass ratio in the Eddington limited case is in fact limited here by the baryon fraction of the host after $z \sim 9$. The viscosity-driven inflow model, on the other hand, takes into account that the black hole growth is limited by the supply of gas which available for accretion. That is, the gas in the halo must lose enough angular momentum to reach the sphere of influence of the black hole for the black hole to grow. With the disc viscosity parameter of $\alpha_\nu = 0.06$, this limits the modelled $M_\bullet/M_{\rm tot}$ ratio dramatically as the black hole grows less efficiently and a stellar galactic disc is maintained.

The viscosity-driven accretion model has an advantage over purely Eddington limited accretion in that the growth rate depends on the properties of the system. However, as I have shown in the previous Chapter, viscosity driven growth is too in-efficient to feed the growth of SMBHs and it is therefore important to compare alternative models. The gravitational torque model first introduced for use in semi-analytic models and simulations by Hopkins & Quataert (2011), has been shown to effectively recreate the observed black hole-galaxy scaling relations (Anglés-Alcázar et al. 2013, 2017; Davé et al. 2019). Hopkins & Quataert (2011) showed that the gravitational torque model better matched the inflow rate in simulations where the viscosity model was under-estimating the inflow rate. In this model the growth of the black hole is assumed to be fed through the inflow of material from the host galaxy disc. This inflow is driven by torques acting on the disc from gravitational instabilities which are growing in the disc itself. The inflow on sub-parsec scales is modelled based on the larger scale properties of the host galactic disc, making the model an attractive sub-grid prescription for cosmological simulations (see, e.g. Davé et al. 2019). In a simulation, the inflow rate towards the black hole can be expressed as a function of galaxy properties

within some aperture, R_0 (Hopkins & Quataert 2011),

$$\dot{M}_{\rm Torque} = \alpha_{\rm T} f_{\rm d}^{\frac{5}{2}} \left(\frac{M_\bullet}{10^8\,{\rm M}_\odot}\right)^{\frac{1}{6}} \left(\frac{M_{\rm d}(R_0)}{10^9\,{\rm M}_\odot}\right) \left(\frac{R_0}{100\,{\rm pc}}\right)^{-\frac{3}{2}} \left(1+\frac{f_0}{f_{\rm g}}\right)^{-1} {\rm M}_\odot\,{\rm yr}^{-1}, \tag{4.2}$$

where,

$$f_{\rm d} \equiv M_{\rm d}(R_0)/(M_{\rm g}(R_0) + M_\star(R_0)), \tag{4.3}$$

$$f_{\rm g} \equiv M_{\rm g}(R_0)/M_{\rm d}(R_0), \tag{4.4}$$

$$f_0 \approx 0.31 f_{\rm d}^2 (M_{\rm d}(R_0)/10^9\,{\rm M}_\odot)^{-1/3}. \tag{4.5}$$

$M_{\rm d}(R_0)$, $M_\star(R_0)$ and $M_{\rm g}(R_0)$ are the total mass enclosed in $R < R_0$ for the disc, stars and gas respectively. In a simulation, the normalisation factor $\alpha_{\rm T} \approx 5$ parametrises the dependence of the inflow rate on unresolved star formation (Hopkins & Quataert 2011). This work uses an analytic approach and as such there is no unresolved star formation and both the gas and stars are modelled as following $\Sigma(R) = \Sigma_0 \exp(-R/R_{\rm d})$. Instead, to find an upper estimate of the inflow rate, and the black hole growth, the scale radius is chosen as $R_0 = R_{\rm d}$. At this scale, the inflow rate is roughly at a maximum (the exact radius varies with the relative masses of the components of the system). This also takes advantage of the model's dependence on the larger scale, disc properties in determining the inflow rate. As no galactic bulge is considered here, this choice of radius means Equations 4.3, 4.4 and 4.5 are simplified so that $f_{\rm d} = 1$, $f_{\rm g} = M_{\rm g}/M_{\rm d}$ and $f_0 \approx 0.48\,(M_{\rm d}/10^9\,{\rm M}_\odot)^{-1/3}$.

By assuming that this torque driven inflow feeds the black hole with an efficiency, $\epsilon_{\rm m}$, the black hole growth rate becomes,

$$\dot{M}_\bullet = \epsilon_{\rm m} \dot{M}_{\rm Torque}, \tag{4.6}$$

This efficiency is also known as the mass retention rate onto the black hole. Simulations calibrated to black-hole-galaxy scaling relations find the mass retention rate is roughly $\epsilon_{\rm m} \sim 0.1 - 0.05$ (Anglés-Alcázar et al. 2013, 2015, 2017; Davé et al. 2019) which roughly agrees with observations (King et al. 2013) and

theoretical predictions (Yuan et al. 2012). There is however, some degeneracy with the $\alpha_{\rm T}$ parameter. To compare the torque driven and viscosity driven growth rates, I add the criterion that the disc must be gravitationally unstable for inflow to occur ($Q < 1$ in Equation 3.2). As shown in Chapter 2 the minimum value of Q depends both on the black hole and disc mass; increasing the black hole mass increases $Q_{\rm min}$ while increasing the disc mass will decrease $Q_{\rm min}$. Note, however, the proportionality $\dot{M}_{\rm Torque} \propto M_{\bullet}^{1/6}$ in Equation 4.2. This is due to the dependence of $\dot{M}_{\rm Torque}$ on the size of the black hole's sphere of influence (Hopkins & Quataert 2011). Increasing the black hole mass increases the size of the sphere of influence of the black hole which, in turn, increases the gas supply which feeds the black hole according to $\dot{M}_{\rm Torque}$. The black hole mass therefore has two impacts on the growth rate: (1) determining the value of Q and the overall stability of the disc and (2) enhancing the accretion rate onto the black hole.

After inflow kicks in (i.e. the disc first becomes unstable) around $z \sim 17$, the black hole growth rate from torque-driven inflow model lags behind the viscosity model until $z \sim 7$. Note, to keep the viscosity model consistent with the upper limit case investigated in Chapter 3, Figure 4.2 shows the viscosity model for the black hole accretion balancing the inflow rate so that $\dot{M}_{\bullet} = \dot{M}_{\rm inf}$ where the inflow rate is defined as,

$$\dot{M}_{\rm inf} = \frac{\alpha_{\nu} c_{\rm s}^2 \pi \Sigma_{\rm g}}{2\Omega} \left| \frac{d \ln \Omega}{d \ln R} \right| \tag{4.7}$$

where $\Sigma_{\rm g}$ is the gas surface density, $c_{\rm s}$ is the sound speed, and $\Omega(R)$ is the angular velocity.

For a fair comparison between the torque- and viscosity-driven inflow models, a second case is shown for the viscosity model with the black hole accreting with the same mass retention rate as the torque model, $\epsilon_{\rm m} = 0.1$. From $z \gtrsim 7$, the torque model fed black hole makes up a more significant fraction of the total DCBH host halo mass than the viscosity model, even compared to the upper viscous disc case with $\epsilon_{\rm m} = 1$. Note that the torque driven model reaches $M_{\bullet}/M_{\rm d} = 0.00084$ at $z = 0$ and as the stellar fraction of the disc is $M_{\star}/M_{\rm d} = 0.98$, this corresponds to $M_{\bullet}/M_{\star} = 0.00085$. This ratio of black hole to stellar mass is roughly in line with the observed scaling relations with $M_{\bullet}/M_{\star} \sim 0.001$ (Kormendy & Ho 2013; Reines & Volonteri 2015). However, this is strongly dependent on the halo growth rate.

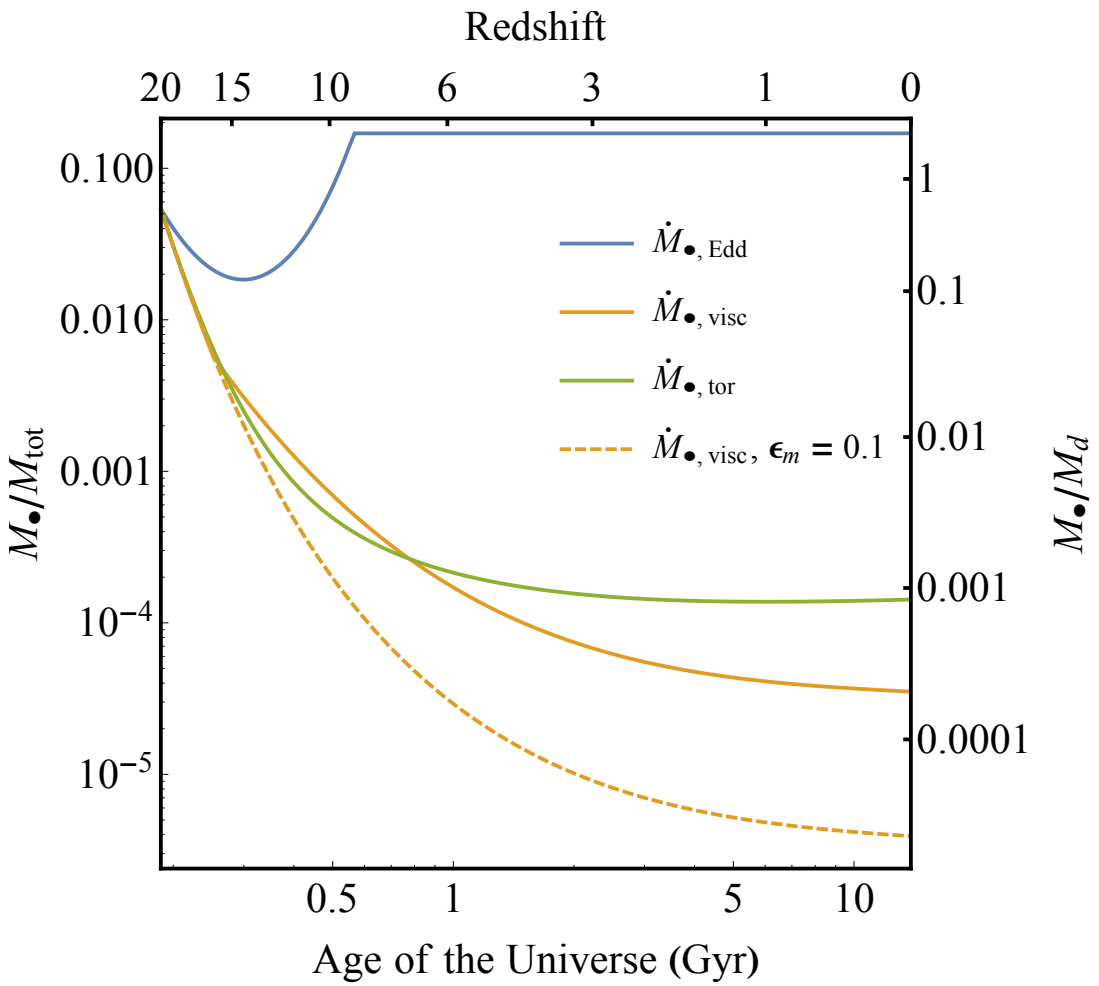

Figure 4.2 *The mass of the black hole as a fraction of the mass of an isolated halo for three black hole growth models: Eddington limited growth (blue line), with a maximum of* $M_\bullet/M_{\rm tot} = f_{\rm b}$*; Viscosity driven inflow (orange lines); and gravitational torque driven inflow (green line). The dashed orange line shows the viscosity model with the only 10 % of the material that reaches the black hole being accreted (as is the case in the torque model). The halo growth rate is set to* $\zeta = \zeta_{\rm CR7} = 0.586$.

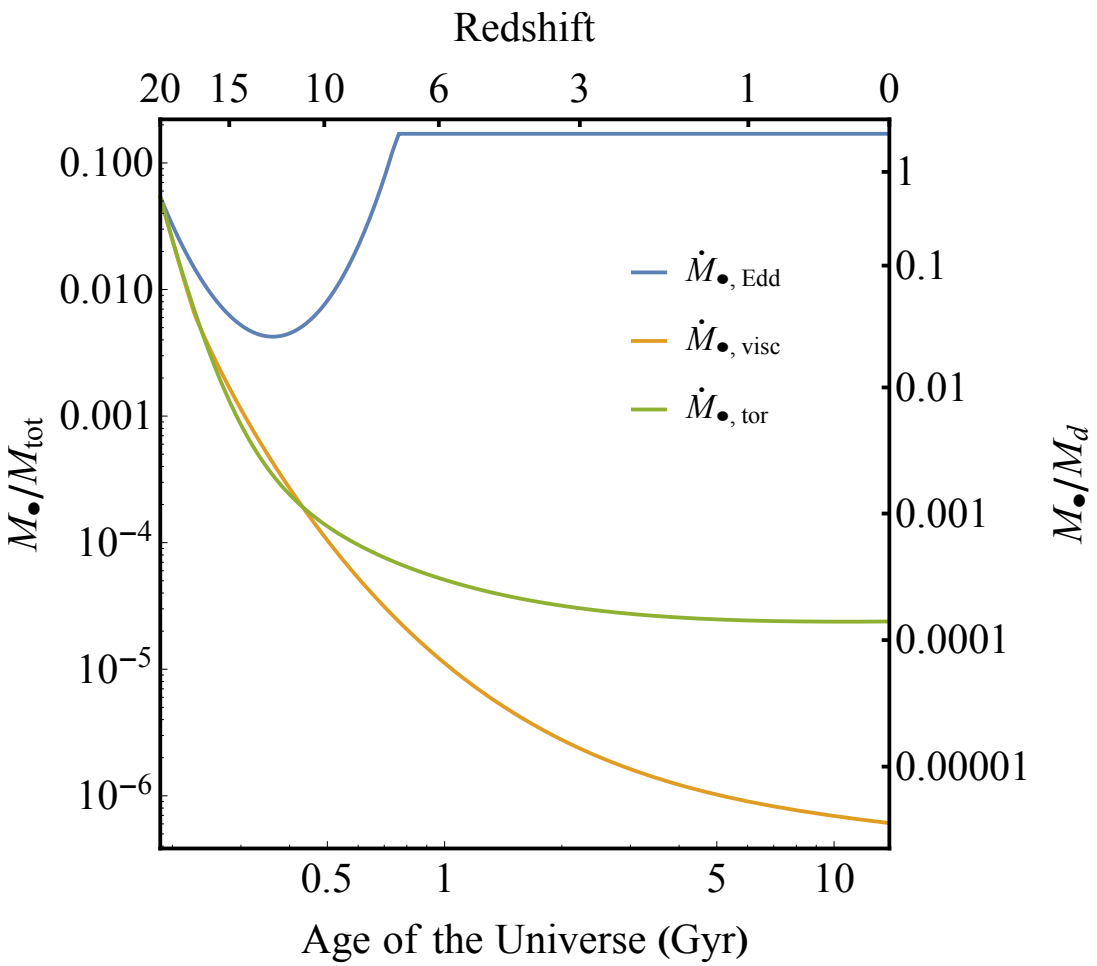

Figure 4.3 *The same as in Figure 4.2 but with a higher halo growth rate, $\zeta = \langle\zeta\rangle = 0.806$. The mass of the black hole as a fraction of the mass of an isolated halo for three black hole growth models: Eddington limited growth (blue line), with a maximum of $M_\bullet/M_{\mathrm{tot}} = f_{\mathrm{b}}$; Viscosity driven inflow (orange lines); and gravitational torque driven inflow (green line).*

4.2.2 Halo growth

In each case shown in Figure 4.2 the halo growth follows,

$$\frac{dM_{\mathrm{tot}}}{dz} = -\zeta M_{\mathrm{tot}} \tag{4.8}$$

where ζ is the halo growth rate parameter. In Figure 4.2 $\zeta = \zeta_{\mathrm{CR7}} \equiv 0.586$ (see Chapters 2 and 3) while $M_{\mathrm{d}} + M_\bullet = f_{\mathrm{b}} M_{\mathrm{tot}}$.

Figure 4.3 shows the same comparison between the three black hole growth models but with the halo growth rate set to the average, $\zeta = \langle\zeta\rangle \equiv 0.806$ (Neistein &

Dekel 2008). In all cases, other than the Eddington limited black hole growth where the black hole reaches the maximum of $M_\bullet/M_{\rm tot} = f_{\rm b}$, the higher growth rate results in the black hole becoming a much smaller fraction of the total mass of the halo. As $M_{\rm tot}$ is larger this is not surprising however, one may naively expect the black hole to keep pace with the other components of the growing system. Indeed, the higher disc masses should drive higher inflow rates and therefore grow the black hole more efficiently. However, the black hole growth lags behind as the inflow rate is not solely dependent on the disc mass. At $z = 0$ the torque-inflow-fed black hole is only a small fraction of the stellar disc mass $M_\bullet/M_\star \sim M_\bullet/M_{\rm d} = 0.00014$ (with $M_\star/M_{\rm d} = 0.99$), nearly an order of magnitude below the $\zeta_{\rm CR7}$ case.

The mass of the black hole and along with properties of its host such as the stellar mass are strongly dependent on the halo growth rate parameter. The lower value of $\zeta_{\rm CR7} = 0.586$ is used for the purposes of this study to reflect the environment in which DCBHs form (see Chapter 1). This growth rate comes from fitting the empirically-motivated model growth history for DCBH candidate CR7 (Sobral et al. 2015; Agarwal et al. 2016a).

As shown in Figures 4.2 and 4.3, the relative masses of the black hole, disc and halo also depend strongly on the black hole growth model. Due to the success of the torque-driven inflow model (Anglés-Alcázar et al. 2013, 2015; Davé et al. 2019) and as it provides black hole masses which generally lie between the other two models used here, I will use this as a fiducial case. For a specified growth model, the black hole and halo mass can be determined at infall, providing both $M_\bullet(z_{\rm infall})$ and $M_{\rm tot}(z_{\rm infall})$.

The size of the halo at a given redshift can be determined by estimating the virial radius. For an infalling DCBH host halo acting as a perturber on the density of the central halo, the size of the perturber, $r_{\rm s}$, is taken to be the virial radius of the infalling subhalo.

4.2.3 Naked black holes

A black hole without a dark matter subhalo is termed as a naked black hole. The existence of such an object is questionable, however, one can envisage a physical process through which a black hole could be separated from its host.

One such mechanism could be through tidal disruption from a major merger event or repeated close encounters, stripping away or destroying the host (Governato et al. 1994; van den Bosch et al. 2008; Condon et al. 2017; van den Bosch 2017). Governato et al. (1994) suggested "wandering" SMBHs could exist, whereby a forming galaxy is completely disrupted before it can fully coalesce, leaving an isolated black hole for a few billion years. At $z \gtrsim 6$, this timescale is longer than the age of the universe and the isolated SMBH could remain separated from its parent halo at the point of infall onto a more massive neighbour.

Alternatively, the black hole host could be disrupted as part of the dynamical friction experienced during the infall of the host into a more massive halo (Condon et al. 2017). However, the timescale over which this disruption could deplete the host will depend significantly on the parameters of the satellite's orbit (e.g. Hopkins et al. 2006).

For a naked black hole, its size as a perturber is the Bondi radius $r_{\rm s} = r_{\rm B} \equiv 2GM_{\bullet}/c_{\rm s}^2$ (Kim & Kim 2009). Inside of $r_{\rm B}$ the escape velocity is greater than the sound speed and the gravitational influence of the black hole begins to dominate. Any gas inside of this radius is therefore considered to be detached from the bulk flow.

4.2.4 Central halo

Other than assuming that the central halo mass follows $M_{\rm cen} > M_{\rm sat}$, the mass of the central host is treated as a free parameter. As part of this study, I aim to explore the influence the central halo's mass has on the infall process.

The central halo is modelled as an isothermal sphere with the density profile,

$$\rho(r) = \frac{V_{\rm c}^2}{4\pi G r^2} \tag{4.9}$$

where $V_{\rm c}^2 = GM_{\rm cen}/r_{200}$ is the circular velocity of the central halo. The infall begins with the infalling body (which I will refer to as the perturber) at the virial radius of the central halo $r = r_{200}$ on a circular orbit so that $V = V_{\rm c}$.

Within the central halo, the hot gas is assumed to follow the same density profile as the dark matter. In the previous chapters (Chapters 2 and 3), the aim for the model was to obtain upper limits on inflow and star formation and

therefore the model used the most massive disc case, i.e. where all the baryons went into forming the black-hole-disc system. In reality, a significant fraction of the baryonic content of haloes is taken up by hot gas which exists beyond the central galaxy (see, e.g. Henley et al. 2010, and references therein). As we are not following the evolution of the central galaxy, we no do not make the same assumption for the central halo as was used in the DCBH host model.

If we assume that the central halo is in virial equilibrium, $T_{\rm vir} \approx T_{\rm gas}$. Using the ideal gas law, the gas temperature can be expressed as a function of the sound speed ($c_{\rm s}$), the mean molecular weight (μ), and the adiabatic index ($\gamma = 5/3$ for mono-atomic gas),

$$T_{\rm gas} = \frac{\mu m_{\rm H}}{\gamma k_{\rm B}} c_{\rm s}^2 \tag{4.10}$$

where $k_{\rm B}$ is the Boltzmann constant and $m_{\rm H}$ is the hydrogen mass. The virial temperature for an isothermal sphere can be expressed as (Mo et al. 2010),

$$T_{\rm vir} = \frac{1}{2} \frac{\mu m_{\rm H}}{k_{\rm B}} V_{\rm c}^2 \tag{4.11}$$

Using $T_{\rm vir} \approx T_{\rm gas}$ and Equations 4.10 and 4.11, we can get an expression for the ratio between the circular velocity and the sound speed $V_{\rm c}/c_{\rm s}$. As the perturber moves at the circular velocity this ratio is $\mathcal{M} = V/c_{\rm s}$, the Mach number of the perturber,

$$\mathcal{M} = \frac{V_{\rm c}}{c_{\rm s}} \approx \sqrt{\frac{2}{\gamma}} \approx 1.095 \tag{4.12}$$

As the baryonic component of the central halo will have formed a galaxy prior to infall, there will be a scale below which the overall density no longer follows the isothermal sphere profile (Equation 4.9). The spin parameter of the halo λ determines the relative size of the central galaxy to the virial radius of its host halo (Mo et al. 1998). Assuming the galaxy forms into a disc in hydrostatic equilibrium such that the scale height follows $H = c_{\rm s}^2 / (\pi G \Sigma)$, we can determine the disc density in the mid-plane $\rho_{\rm d}(R)$ as a function of cylindrical radius, R. The ratio of this density to the isothermal sphere density at a given radius is mainly a function of the relative sizes and masses of the galaxy disc and halo, but also varies with the gas temperature and thus can be expressed as a function

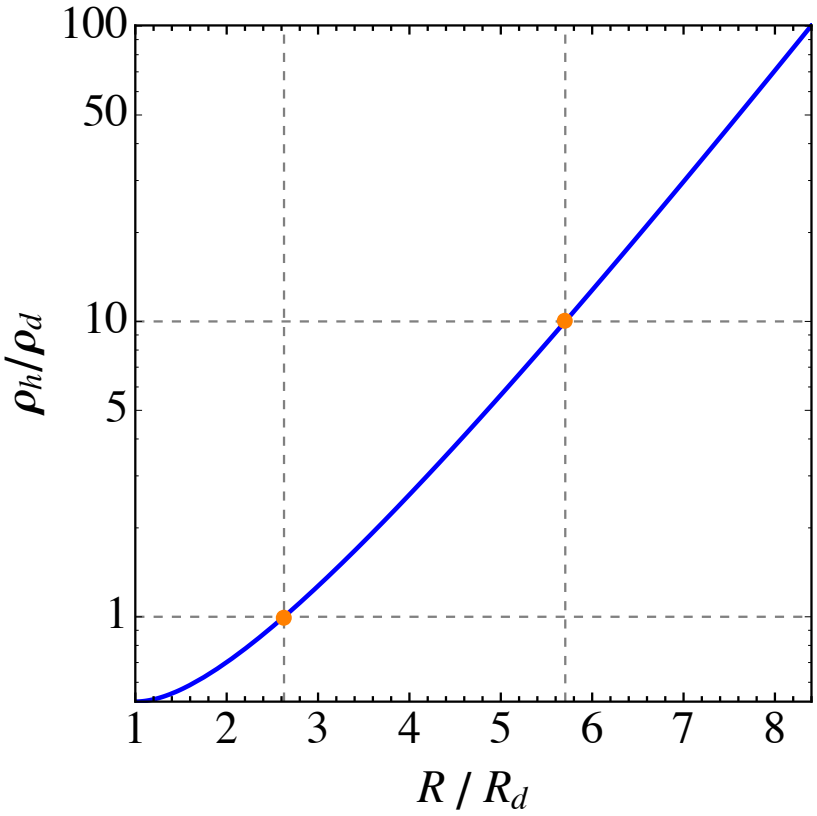

Figure 4.4 *The ratio of the halo density to the density of the disc within the midplane. The orange dots indicate two radii: firstly, at which the densities are equal ($R = 2.628$) and the secondly where the density within the halo is 10 times higher than the disc density, ($R = 5.706$). The parameters of the halo are as follows: $\gamma = 5/3$ ($\mathcal{M} = 1.095$), $\lambda = 0.05$, and $f_\mathrm{b} = 0.17$.*

of $\mathcal{M}$. Figure 4.4 shows the density ratio as a function of radius for $\gamma = 5/3$ ($\mathcal{M} = 1.095$), $\lambda = 0.05$ ($R_\mathrm{d}/r_{200} = 0.05/\sqrt{2}$), and $f_\mathrm{b} = 0.17$ (which roughly gives M_d/M_{200}). For these parameter values we can calculate numerically the critical radius where $\rho_\mathrm{iso} = \rho_\mathrm{d}$ as $x_\mathrm{end} = r_\mathrm{end}/r_{200} = 2.628R_\mathrm{d}/r_{200}$.

Inside of r_end on the disc mid-plane, the galaxy provides a larger contribution to the density than the halo. It is therefore beyond the limits of the equations used in the sections below to follow the evolution to smaller scales and all calculations are halted when the perturber reaches this radius.

4.3 Analysis

4.3.1 Gravitational drag force

In this subsection I will refer to the radius r and cylindrical coordinates R and z. Unlike the rest of this chapter where the frame of reference is centred on the central halo, these coordinates are all in reference to positions relative to the perturber.

The dynamical friction force acting on a point mass perturber of mass $M_{\rm p}$ moving at a constant speed V through a uniform gas of density ρ_0 can be calculated approximately using linear perturbation theory (Ostriker 1999),

$$F_{\rm DF} = -I\frac{4\pi\left(GM_{\rm p}\right)^2\rho_0}{V^2} \tag{4.13}$$

where I depends on the Mach number of the perturber, $\mathcal{M} = V/c_{\rm s}$, and can be split into sub- and super-sonic parts,

$$I = \begin{cases} \frac{1}{2}\ln\left(\frac{1+\mathcal{M}}{1-\mathcal{M}}\right) - \mathcal{M} & \mathcal{M} < 1 \\ \frac{1}{2}\ln\left(1-\frac{1}{\mathcal{M}^2}\right) + \ln\left(\frac{Vt}{r_{\rm min}}\right) & \mathcal{M} \geq 1 \end{cases} \tag{4.14}$$

The minimum radius, $r_{\rm min}$, is introduced to avoid the potential singularity at $r = 0$ and represents the point where the wake begins. Kim & Kim (2009) showed numerically that $r_{\rm min} = 0.35\mathcal{M}^{0.6}r_{\rm s}$ provides a good analytic approximation, where $r_{\rm s}$ is the size of the perturber.

The process of deriving Equation 4.13 is outlined in Ostriker (1999). In the remainder of this subsection I summarise the derivation of the super-sonic case. The author begins by using the linearized wave equations for a perturbed density $\rho = \rho_0(1 + \alpha(\mathbf{x}, t))$ to find an expression for the perturbation, $\alpha(\mathbf{x}, t)$. Ostriker (1999) shows that if the perturbation begins at $t = 0$ and the perturber is a point mass moving through an otherwise uniform gas at a constant velocity the

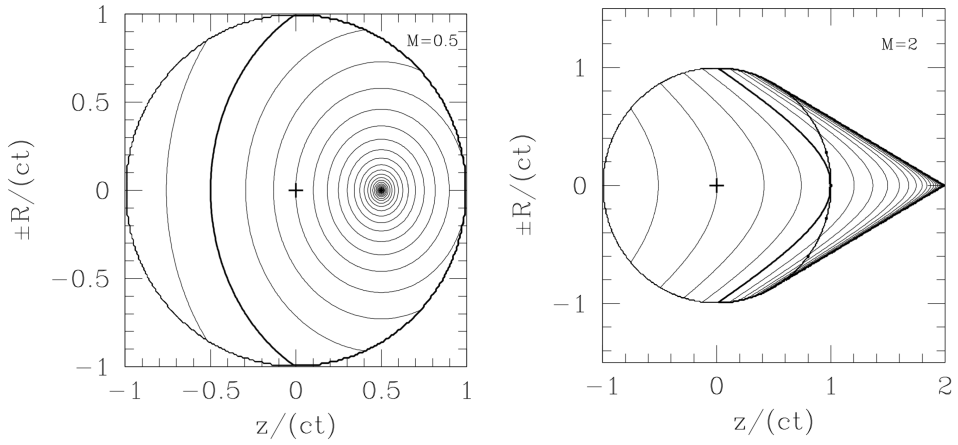

Figure 4.5 *The two panels are taken from Ostriker (1999), they show a slice of the perturbed region for both the sub- and super-sonic cases ($\mathcal{M} = 0.5$ on the left and $\mathcal{M} = 2$ on the right) with the density perturbation indicated by the contours. "Contours show isosurfaces of* $\log(\tilde{\alpha}) = \log(\alpha) - \log\left(GM_{\rm p}/(tc_{\rm s}^3)\right)$ *in intervals of 0.1 [where α is defined in Equation 4.15]. Density increases toward the perturber [which in the super-sonic case is] at the apex of the Mach cone. The heavy contour indicates the surface with $\tilde{\alpha} = 1$. There is a density jump with $\Delta \log \alpha = \log 2 = 0.301$ at the surface $R^2 + z^2 = (c_{\rm s}t)^2$ The plus symbol indicates the initial position of the perturber."*

perturbed density becomes,

$$\alpha(t) = \frac{G\,M_{\rm p}/c_{\rm s}^2}{\sqrt{s^2 + R^2(1-\mathcal{M}^2)}} \times \begin{cases} 1 & R^2 + z^2 < (c_{\rm s}\,t)^2 \\ 2 & \mathcal{M} > 1, R^2 + z^2 > (c_{\rm s}\,t)^2, \\ & \qquad s/R < -\sqrt{\mathcal{M}^2 - 1}, \\ & \qquad\qquad \text{and } z > c_{\rm s}\,t/\mathcal{M} \\ 0 & \text{otherwise} \end{cases} \tag{4.15}$$

Each of the cases in Equation 4.15 correspond to different sections of the perturbed region shown in Figure 4.6. The first region signifies the sphere with a radius of $c_{\rm s}t$, drawn out as the wake moves in all directions at $c_{\rm s}$ over the time, t, since the perturbation began with the perturber initially at $R = 0$, $z = 0$. The second case is the Mach cone which is only there for the super-sonic cases (e.g. compare the panels in Figure 4.5) where the perturber itself is moving faster than the sound speed so that it extends beyond the $c_{\rm s}t$ bubble.

The perturbed density exerts a gravitational force on the perturber which acts

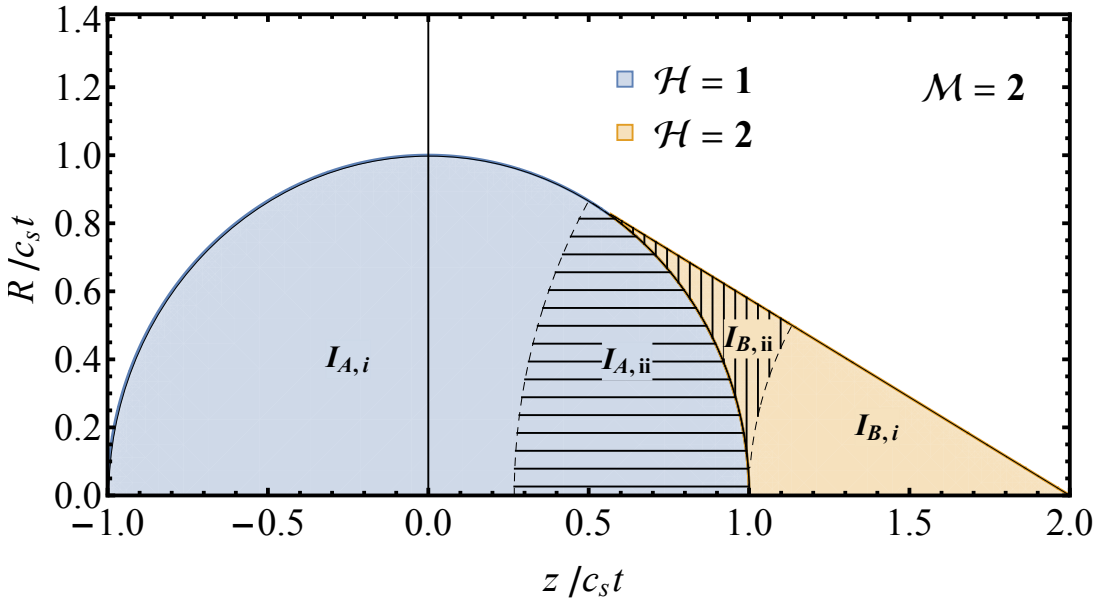

Figure 4.6 *A slice similar to the right hand panel of Figure 4.5, this time showing the different regions of the Mach cone. The colour signifies the different values given to the contribution to α. The four labelled regions ($I_{\mathrm{A,i}}$, $I_{\mathrm{A,ii}}$, $I_{\mathrm{B,i}}$, and $I_{\mathrm{B,ii}}$) indicate the separate sections over which one must integrate to find the total force shown in Equations 4.13 and 4.14.*

as a drag, pointing in the opposite direction from the velocity vector. The total force between the perturber and the wake can be found be solving the following integral,

$$F_{\mathrm{DF}} = 2\pi G M_{\mathrm{p}} \rho_0 \int\int ds\, dR\, R \frac{\alpha(t) s}{\left(s^2 + R^2\right)^{3/2}} \tag{4.16}$$

Note the 2π from the azimuthal convolution to get the full 3-D shape. Also note the factor of $\hat{s} = s/\left(s^2 + R^2\right)^{1/2}$ in the integral as we only care about the component in the s direction with the R components cancelling-out.

Equations 4.16 and 4.15 can also be expressed in polar coordinates $(r,\, \theta)$, centred on the perturber with $R = r \sin\theta$ and $s = r\cos\theta$, and simplified using $\mu_\theta = \cos\theta$ and $x = r/c_{\mathrm{s}}t$. This gives Equation 4.13, hiding the not-yet-solved equation in the definition of I,

$$I = -\frac{1}{2} \int \frac{dx}{x} \int d\mu_\theta \frac{\mu_\theta \mathcal{M}^2 \mathcal{H}}{\left(1 - \mathcal{M}^2 + \mu_\theta^2 \mathcal{M}^2\right)^{1/2}} \tag{4.17}$$

$\mathcal{H}$ is the value shown as the cases in Equation 4.15. The limits and correct value of $\mathcal{H}$ must be chosen correctly to isolate each region as indicated in Figure 4.6. For $I_{\mathrm{B,\,i}}$, one must integrate from $\mu_\theta = -1$ to $\mu_\theta = \mu_\mathcal{M}$ and from $x = r_{\min}/c_\mathrm{s}t$ to $x = \mathcal{M} - 1$. Where $\mu_\mathcal{M} = -\sqrt{\mathcal{M}^2 - 1}/\mathcal{M}$ corresponds to the angle of the Mach cone boundary. For $I_{\mathrm{B,\,ii}}$ the limits are from $\mu_\theta = \mu_\mathrm{C}$ to $\mu_\theta = \mu_\mathcal{M}$ and from $x = \mathcal{M} - 1$ to $x = \sqrt{\mathcal{M}^2 - 1}$. Where the boundary of the circle is a function of x which follows $\mu_\mathrm{C} = (1 - \mathcal{M}^2 - x^2)/(2x\mathcal{M})$. In both $I_{\mathrm{B,\,i}}$ and $I_{\mathrm{B,\,ii}}$ the perturbed density normalization is $\mathcal{H} = 2$. For the $\mathcal{H} = 1$ region, the integral is also split. $I_{\mathrm{A,\,i}}$ is found by integrating $\mu_\theta = -1$ to $\mu_\theta = \mu_\mathrm{C}$ and from $x = \sqrt{\mathcal{M}^2 - 1}$ to $x = \mathcal{M} + 1$. Finally $I_{\mathrm{A,\,ii}}$ can be calculated by integrating from $\mu_\theta = -1$ to $\mu_\theta = \mu_\mathcal{M}$ for $x = \mathcal{M} - 1$ to $x = \sqrt{\mathcal{M}^2 - 1}$ and subtracting $I_{\mathrm{B,\,ii}}/2$. The factor of $1/2$ comes from the different value of $\mathcal{M}$. This gives the following expressions for each region:

$$I_{\mathrm{A,\,i}} = \frac{1}{2}\ln\left(\mathcal{M}^2 - 1\right) - \ln(\mathcal{M} + 1) + \mathcal{M} - \sqrt{\mathcal{M}^2 - 1} \tag{4.18}$$

$$I_{\mathrm{A,\,ii}} = \ln(\mathcal{M} - 1) - \frac{1}{2}\ln\left(\mathcal{M}^2 - 1\right) + \mathcal{M} - \sqrt{\mathcal{M}^2 - 1} \tag{4.19}$$

$$I_{\mathrm{B,\,i}} = 2\left[\ln\left(\frac{r_{\min}}{c_\mathrm{s}t}\right) - \ln(\mathcal{M} - 1)\right] \tag{4.20}$$

$$I_{\mathrm{B,\,ii}} = 2\left[\sqrt{\mathcal{M}^2 - 1} - \mathcal{M}\right] \tag{4.21}$$

Combine each expression as $I_\mathrm{super} = -(I_{\mathrm{A,\,i}} + I_{\mathrm{A,\,ii}} + I_{\mathrm{B,\,i}} + I_{\mathrm{B,\,ii}})/2$ results in the following,

$$I_\mathrm{super} = \frac{1}{2}\ln\left(1 - \frac{1}{\mathcal{M}^2}\right) - \ln\left(\frac{Vt}{r_{\min}}\right) \tag{4.22}$$

This is equivalent to the super-sonic case in Equation 4.14.

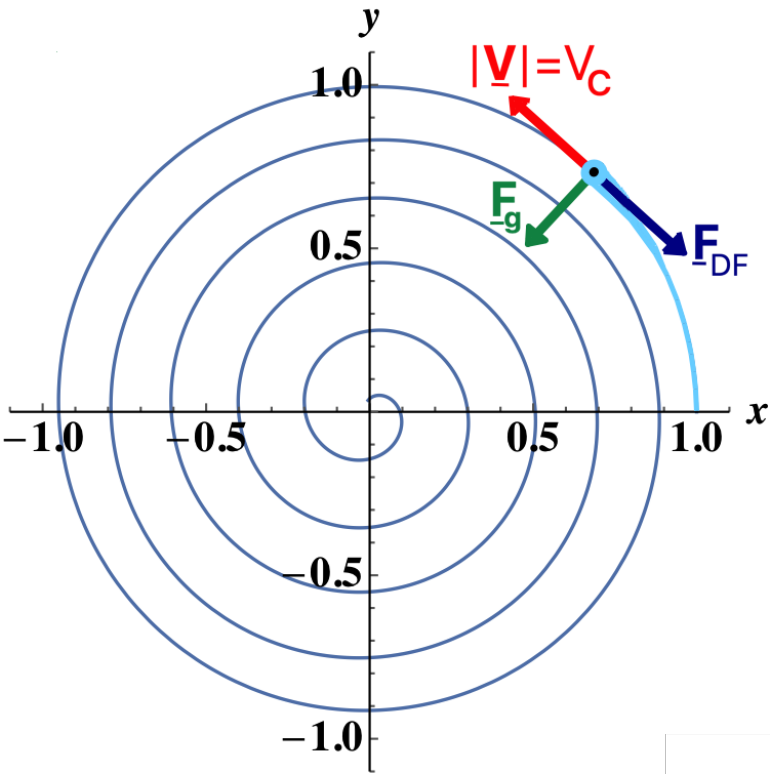

Figure 4.7 *A sketch diagram of the decaying orbit of the infalling satellite halo with the forces acting on it. The x and y coordinates of the orbital plane are shown in units of the virial radius of the central halo. The sketched wake is not shown to scale but is shown to illustrate why assuming $F_{\rm DF}$ and the velocity vector are always anti-parallel is not fully accurate.*

4.3.2 Dynamical friction driving infall

For the case of an infalling perturber in an isothermal sphere, we assume the radial velocity is negligible (compared to the total speed of the perturber) and that the velocity is the circular velocity of the central halo, $V = V_{\rm c} = GM_{\rm cen}/r_{200} = \text{const.}$ The density profile of the isothermal sphere is approximately constant over the wake from the perturber. We can therefore replace $\rho_0 = \rho(r) = V_{\rm c}^2/(4\pi G r^2)$ and Equation 4.13 becomes,

$$F_{\rm DF} = -I\frac{GM_{\rm p}^2}{r^2} \tag{4.23}$$

By assuming that the perturber remains on a near-circular orbit throughout infall, we can say that the drag force is always acting in the tangential direction, applying a torque and decreasing angular momentum (see Figure 4.7). The gravitational

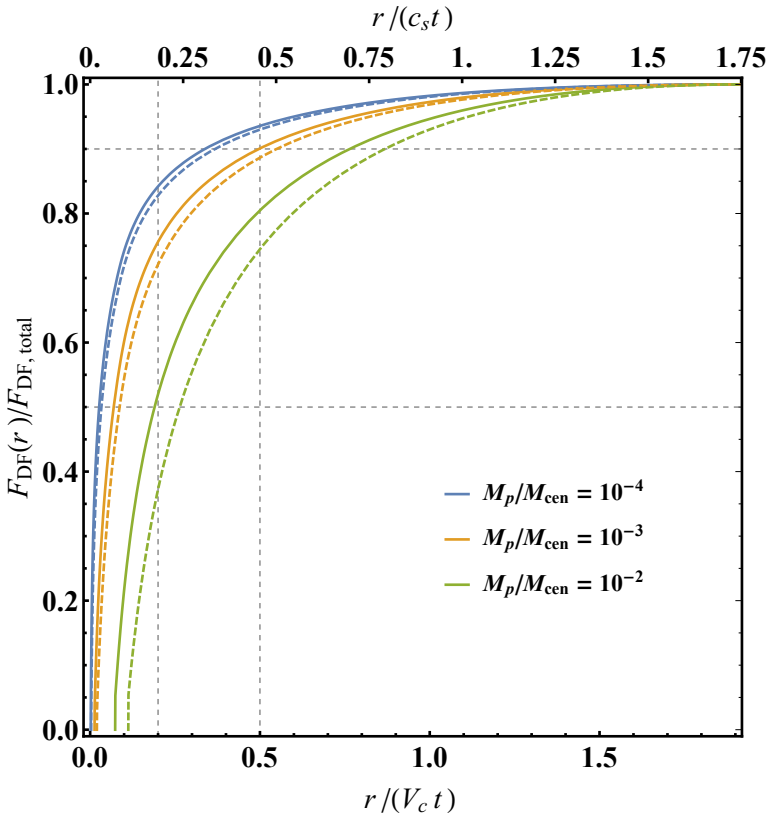

Figure 4.8 *The fraction of the drag force acting on the perturber from the wake inside of the distance r from the perturber. The solid and dashed lines show the cases for the satellite halo ($r_{\rm s} = r_{\rm sat}$) and naked black hole ($r_{\rm s} = r_{\rm B}$) perturbers respectively.*

attraction between the central halo and the perturber acts as the restoring force maintaining the orbit. In reality the wake would trace the orbit of the perturber and the drag force would not act solely in the direction tangential to the orbit.

Figure 4.8 shows what fraction of the drag force is due to the wake inside of a radius, r, from the perturber. One can see that the largest contribution to the drag force comes from the material closest to the perturber. The fractional contribution from inside a given value of $r/(V_{\rm c}t)$ varies significantly with the mass ratio of the perturber to the central halo, $M_{\rm p}/M_{\rm cen}$. For a higher $M_{\rm p}/M_{\rm cen}$ ratio, the fractional contribution to the drag force at a given $r/(V_{\rm c}t)$ decreases. For example, at $r/(V_{\rm c}t) = 0.2$, of the three cases shown with $r_{\rm s} = r_{\rm sat}$, $F_{\rm DF}(r)/F_{\rm DF,\,total}$ is largest for $M_{\rm p}/M_{\rm cen} = 10^{-4}$ at $F_{\rm DF}(0.2V_{\rm c}t)/F_{\rm DF,\,total} \sim 0.84$ (0.83 for $r_{\rm s} = r_{\rm B}$), while $F_{\rm DF}(0.2V_{\rm c}t)/F_{\rm DF,\,total} \sim 0.5$ (0.4 for $r_{\rm s} = r_{\rm B}$) in the $M_{\rm p}/M_{\rm cen} = 10^{-2}$ case. For low mass ratios $M_{\rm p}/M_{\rm cen} << 1$, the region closest to the perturber ($r \sim 0.2V_{\rm c}t$) provides the largest contribution to the total drag force and the component of dynamical friction in the direction of the centre of the halo from

the perturber will be small. I make the approximation that $F_{\rm DF}$ acts solely in the direction tangential to the orbit but note this will not hold for large mass ratios $M_{\rm p}/M_{\rm cen} \gtrsim 0.01 - 0.1$.

By equating the change in angular momentum to the dynamical friction force and assuming the perturber's mass and velocity do not change, we can gain an expression for the radial velocity over the period of infall.

$$\frac{d}{dt}\left(rM_{\rm p}V_{\rm c}\right) = rF_{\rm DF} = -I\frac{GM_{\rm p}^2}{r} \tag{4.24}$$

$$V_{\rm c}\frac{dr}{dt} = -V_{\rm c}^2\,\frac{r_{200}}{r}\,\frac{M_{\rm p}}{M_{\rm cen}}I \tag{4.25}$$

$$\frac{dr}{dt} = -I\,\frac{r_{200}}{r}\,\frac{M_{\rm p}}{M_{\rm cen}}V_{\rm c} \tag{4.26}$$

By integrating Equation 4.26 we can find the full infall evolution $r(t)$ to determine properties such as the total time required for the perturber to reach the central galaxy from the virial radius of the central halo, $t_{\rm merge}$. This can only be done numerically as I varies with the time since the perturbation began.

4.4 Infall evolution calculation

Figure 4.9 shows the evolution of the radial position of the perturber, $r(t)$, for four different mass ratios. Figure 4.10 shows the change in the radial velocity (as a fraction of $V_{\rm c}$ for the same mass ratios. Two cases are shown, one for each of the two different perturbers investigated here: An infalling satellite halo and a naked black hole. In both cases an increase in the mass ratio leads to a more rapid infall with the perturber reaching the final radius (where the central galaxy disc density becomes comparable to the halo density).

The differences between $r(t)$ in the two cases of perturber comes from the difference in the perturber size and the onset of infall. The size of the perturber, $r_{\rm s}$ provides a minimum radius for the gravitational drag calculation ($r_{\rm min} = 0.35 r_{\rm s}\mathcal{M}^{0.6}$ Kim & Kim 2009). The wake therefore has to be larger than $r_{\rm min}$ for there to be any drag acting on the perturber to cause the infall. Therefore for a larger perturber, there is a slight delay in the onset of the infall. This difference in the time to complete the infall may increase slightly more over the infall due to

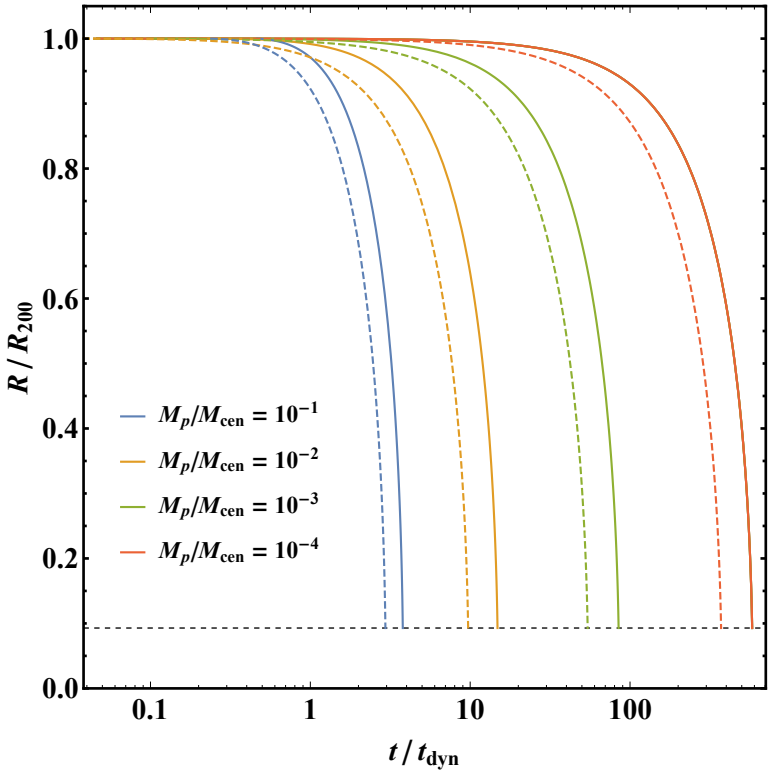

Figure 4.9 *Position of the infalling perturber relative to the centre of the central halo for four different mass ratios* $M_{\rm sat}/M_{\rm cen} = 10^{-4}$, 10^{-3}, 10^{-2}, *and* 10^{-1} *(as represented by the red, green, orange, and blue lines respectively). The solid lines show the infalling satellite case while the naked black hole is shown using the dashed lines. The horizontal dashed line indicates the final radius,* $r_{\rm end}$, *where the density profile of central galaxy becomes significant.*

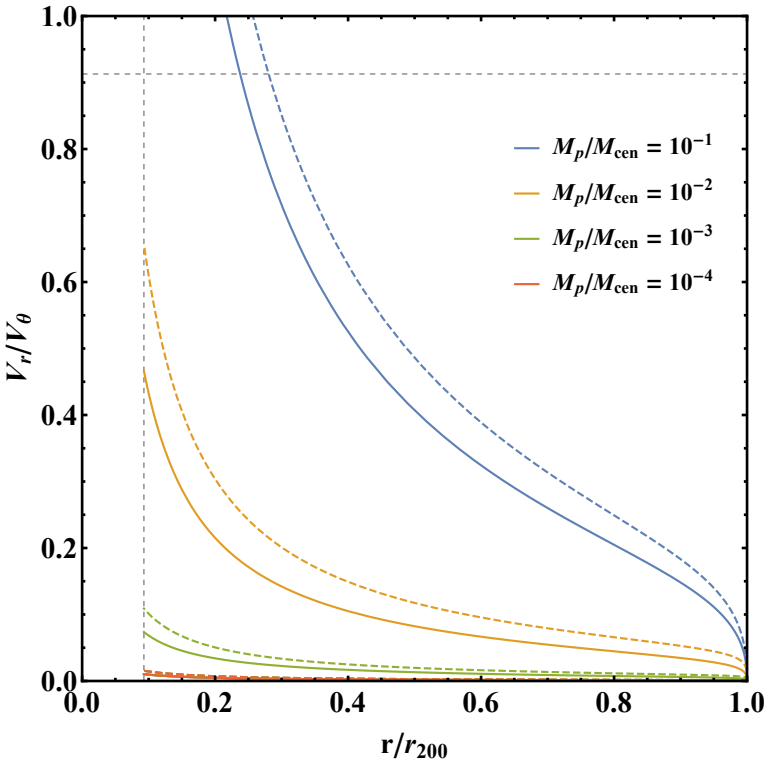

Figure 4.10 *The ratio of the radial and tangential velocities as a function of the position of the infalling satellite halo relative to the centre of the central halo for four different mass ratios* $M_{\rm sat}/M_{\rm cen} = 10^{-4}$, 10^{-3}, 10^{-2}, *and* 10^{-1} *(as represented by the red, green, orange, and blue lines respectively). The tangential velocity is simply* $V_\theta = V_{\rm c} = {\rm const}$. *The vertical dashed line indicates the final radius,* $r_{\rm end}$, *where the density profile of central galaxy becomes significant. The horizontal dashed line shows the sounds speed.*

the wake being slightly smaller with a larger $r_{\rm min}$. The perturbed density is at a maximum at $r_{\rm min}$ and therefore an increase in $r_{\rm min}$ can reduce the force from the wake significantly. However, the difference in the onset of the infall provides the most significant difference in the total time for the perturber to reach $r_{\rm end}$. Note, in this case we are comparing the two perturber cases with the same mass relative to the central halo. Of course, the infalling halo is likely to be more massive than a naked black hole and therefore the timescale for the infall to complete would be more dependent on the difference in the masses

The radial velocity increases as the perturber is brought closer to the center and reaches a maximum at the end of the calculation. In the low mass ratio cases $M_{\rm p}/M_{\rm cen} = 10^{-3}$ and 10^{-4}, $V_{\rm r}$ remains an insignificant fraction of the azimuthal velocity, with $V_{\rm r}/V_\theta \lesssim 0.1$. For $M_{\rm p}/M_{\rm cen} = 0.1$ the radial velocity component is more significant, reaching $\sim 0.5V_\theta$ and $\sim 0.7V_\theta$ for the two perturber sizes. With the smaller perturber, the radial speed is larger for each mass ratio, due to the difference in the wake minimum radius.

In the $M_{\rm p}/M_{\rm cen} = 0.1$ case the radial motion becomes supersonic around $r \sim 0.25r_{200}$ and reaches $V_{\rm r} \sim 2.75V_\theta$ at the end of the calculation. In this case the assumptions of the model do not hold. A significant dynamical friction force would be acting on the perturber in the radial direction which is not taken into account in the calculation. For mass ratios above $M_{\rm p}/M_{\rm cen} \sim 0.01$ the assumption that the radial velocity is insignificant does not hold.

4.5 Infall timescale

From $r(t)$, one can determine the merging time, $t_{\rm merge}$, the time it takes for the infalling perturber to reach the radius where the densities of the halo and central galaxy disc are equal, $r = r_{\rm end}$. This is roughly the radius where the perturber would begins to merge with the central galaxy. Figure 4.11 shows $t_{\rm merge}$ as a function of the mass ratio of the perturber to the central halo $M_{\rm p}/M_{\rm cen}$ for the two cases of $r_{\rm s} = r_{\rm B}$ and $r_{\rm s} = r_{\rm sat}$. Except for the the highest mass ratios, $t_{\rm merge}$ decreases with $M_{\rm p}/M_{\rm cen}$ and the smaller perturber size $r_{\rm s} = r_{\rm B}$ has a shorter $t_{\rm merge}$ for the same given mass ratio. As the relative perturber size, $r_{\rm s}/r_{200}$, scales more steeply with the mass ratio in the $r_{\rm s} = r_{\rm B}$, at higher mass ratios the naked black hole perturber ($r_{\rm s} = r_{\rm B}$) is in fact larger (for $M_{\rm p}/M_{\rm cen} > 0.269$, see Figure 4.12). Note that at these mass ratios each of the perturber sizes become

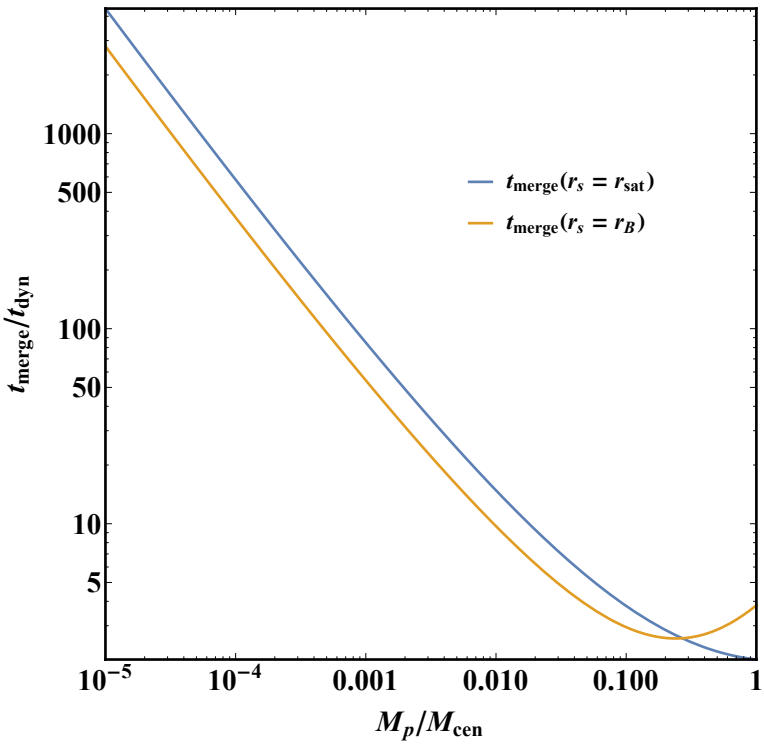

Figure 4.11 *$t_{\rm merge}$, the time it takes for the infalling perturber to reach the final radius, $r = x_{\rm end} r_{200}$, as a function of the mass ratio between the perturber and the central halo. The blue and orange lines show*

a significant fraction of the virial radius of the central halo. In this regime the linear perturbation calculation used in deriving Equation 4.13 (Ostriker 1999) does not hold. Furthermore, the approximation that $\rho_0 \approx \rho(r)$ (in going from Equation 4.13 to Equation 4.23) will not hold.

The minimum in the merging time in Figure 4.11 comes from the increasing $r_{\rm s}$ in both cases. For large $r_{\rm s}$ the delay in the onset of dynamical friction ($t \sim r_{\rm s}/V_{\rm c}$) becomes significant and this delay begins to dominate the $t_{\rm merge}$. This results in the merging time beginning to *increase* for very large mass ratios. As stated already, the assumptions used for this calculation break down in this regime ($M_{\rm p}/M_{\rm sat} \gtrsim 0.01$), as well as the applicability of the dynamical friction calculation.

For low mass ratios ($M_{\rm p}/M_{\rm cen} < 0.001$) the merging time is very large. For example at $z \sim 8$, the dynamical time, $t_{\rm dyn} \sim 0.1$ Gyr, and $t_{\rm merge}(M_{\rm p}/M_{\rm cen} = 0.001) = 8.46$ Gyr, > 12 times the age of the universe at this redshift. Figure 4.13 shows $z_{\rm merge}$, the redshift at which the perturber reaches the final radius, as function of the mass ratio for a section of infall redshifts. For the low mass ratio, the large $t_{\rm merge}$ pushes the end of the calculation to lower redshifts. For an infall

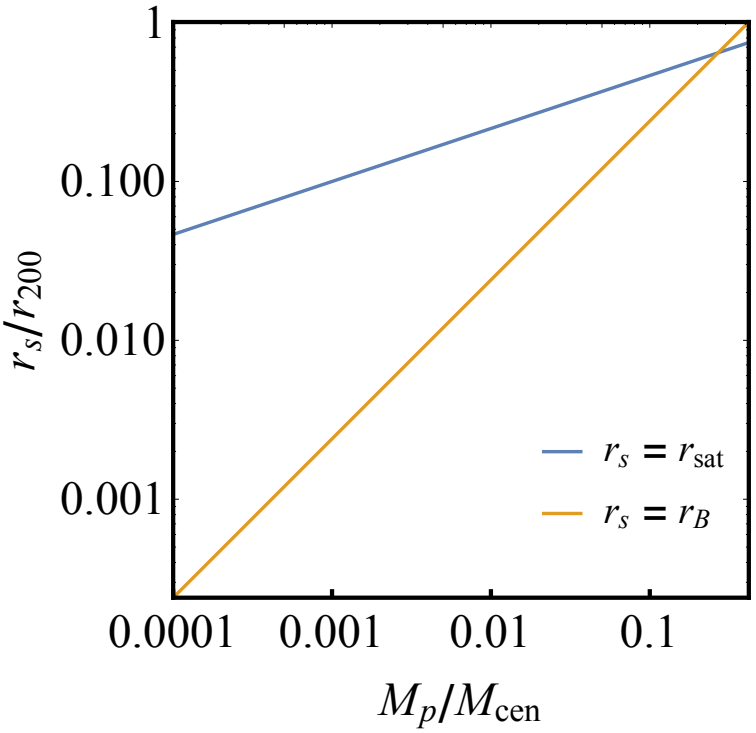

Figure 4.12 *For both $r_{\rm s} = r_{\rm B}$ (orange line) and $r_{\rm s} = r_{\rm sat}$ (blue line), $r_{\rm s}/r_{200}$ scales with the mass ratio of the perturber. In most cases $r_{\rm B}/r_{200} < r_{\rm sat}/r_{200}$, however at $M_{\rm p}/M_{\rm cen} > 0.269$, the higher mass fraction results in $r_{\rm B}/r_{200} > r_{\rm sat}/r_{200}$.*

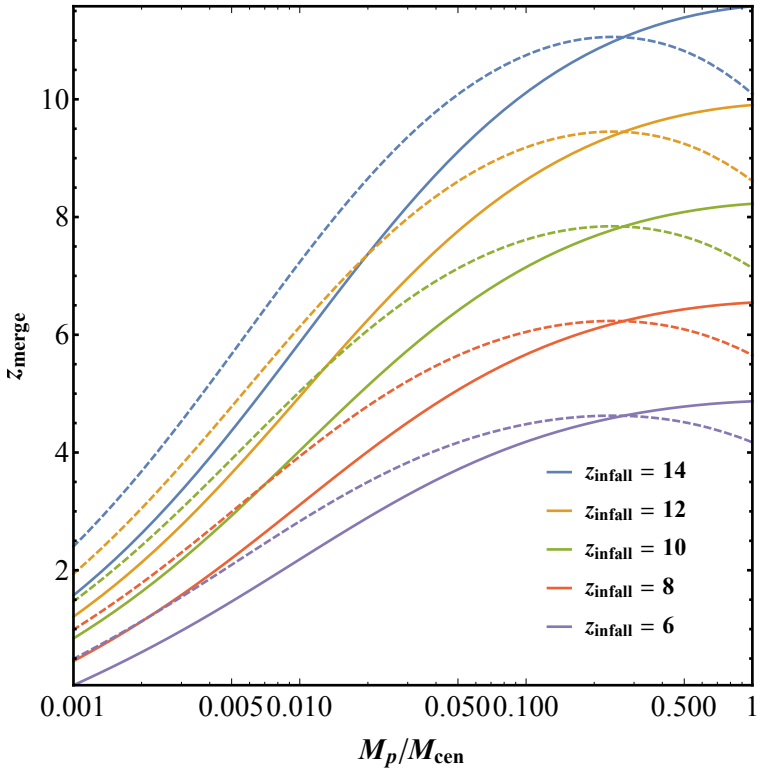

Figure 4.13 *For a range of infall redshifts, $t_{\rm merge}$, is used to calculate a final redshift for the calculation, $z_{\rm merge}$, as a function of the mass ratio between the perturber and the central halo. The solid and dashed lines show the cases for the satellite halo ($r_{\rm s} = r_{\rm sat}$) and naked black hole ($r_{\rm s} = r_{\rm B}$) perturbers respectively.*

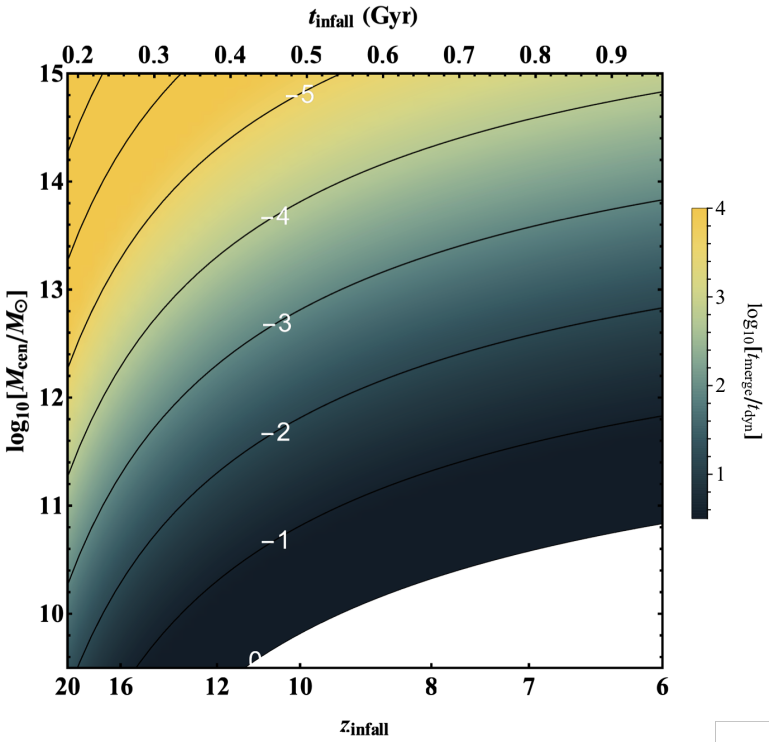

Figure 4.14 *$t_{\rm merge}$, the time it takes for an infalling satellite halo to reach the final radius, $r = x_{\rm end}\, r_{200}$, as a function of the mass of the central halo and the redshift at which the infall begins, $z_{\rm infall}$. The satellite halo is modelled to be an atomic cooling halo at $z_{\rm seed} = 20$ which grows at $\zeta = \zeta_{\rm CR7} = 0.568$, giving $M_{\rm sat}(z_{\rm infall})$. The contours show lines of constant $\log_{10}(M_{\rm sat}/M_{\rm cen})$ (the corresponding value is shown by the white numbers). No cases with $M_{\rm p}/M_{\rm cen} > 1$ are shown.*

event with $M_{\rm p}/M_{\rm cen} \sim 0.01$ to complete prior to $z \sim 6$, it must begin early enough at $z \gtrsim 12$. For $M_{\rm p}/M_{\rm cen} < 0.269$, the shorter $t_{\rm merge}$ in the $r_{\rm s} = r_{\rm B}$ case means the infall completes at an earlier redshift.

The timescale over which the infall process completes is strongly dependent on the relative mass of the perturber and the central halo. Other than requiring that the central halo is more massive than the perturber, the mass of the central halo is a free parameter. The perturber mass on the other hand is determined from another model parameter, the initial redshift of the calculation, i.e. the infall redshift. The satellite subhalo was previously the site of the formation of the DCBH it hosts. During the formation of the DCBH its host halo - the now infalling satellite - must have been an atomic cooling halo. For a given seed formation redshift, one can calculate the mass evolution of the DCBH host halo up to the point of infall $z = z_{\rm infall}$. Figures 4.14−4.21 show the merging time and redshift as a function of the mass of the central halo and the infall redshift.

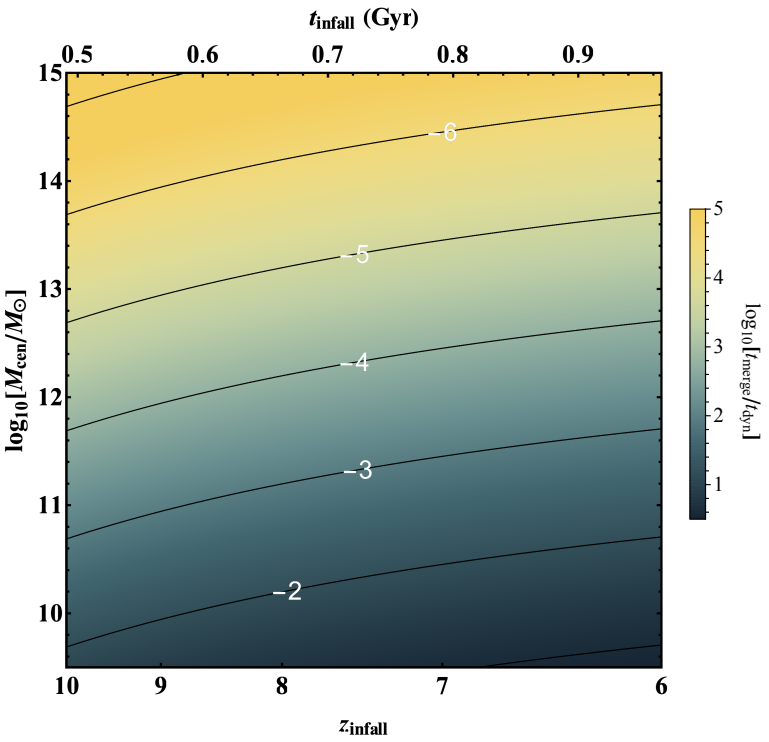

Figure 4.15 *The same as Figure 4.14 except with the satellite halo modelled to be an atomic cooling halo at* $z_{\rm seed} = 10$.

Figure 4.14 shows how the merging time varies with both the mass of the central halo and the initial redshift at the beginning of the infall process. The formation redshift of the seed black hole is assumed to be $z_{\rm seed} = 20$, meaning the satellite is an atomic cooling halo at this same redshift. This halo then grows using Equation 4.8 with $\zeta = \zeta_{\rm CR7}$. The lower $z_{\rm infall}$ is, the later the infall occurs. Pushing the infall to later times decreases the merging time - for a constant value of central halo mass. Meanwhile, at a given infall redshift, increasing the mass of the halo increases the merging time. Both of these last two points come from the dependence of the merging time on the relative masses of the perturber and the central halo. The timescale is largest for high central halo masses and early infall times (higher $z_{\rm infall}$), as shown in the top left of this plot, where the mass ratio is highest. The mass ratio contours are roughly in-line with the trend shown in the $t_{\rm merge}$ colour map, agreeing with the dependence of the merging time on the mass ratio found above (Figure 4.11). Figure 4.15 shows the same except for a later seed formation time. The seed black hole is assumed to form at $z = 10$. The later formation time means that the DCBH host halo cannot reach the same mass, decreasing the mass ratio and increasing the time taken for the perturber to complete its infall.

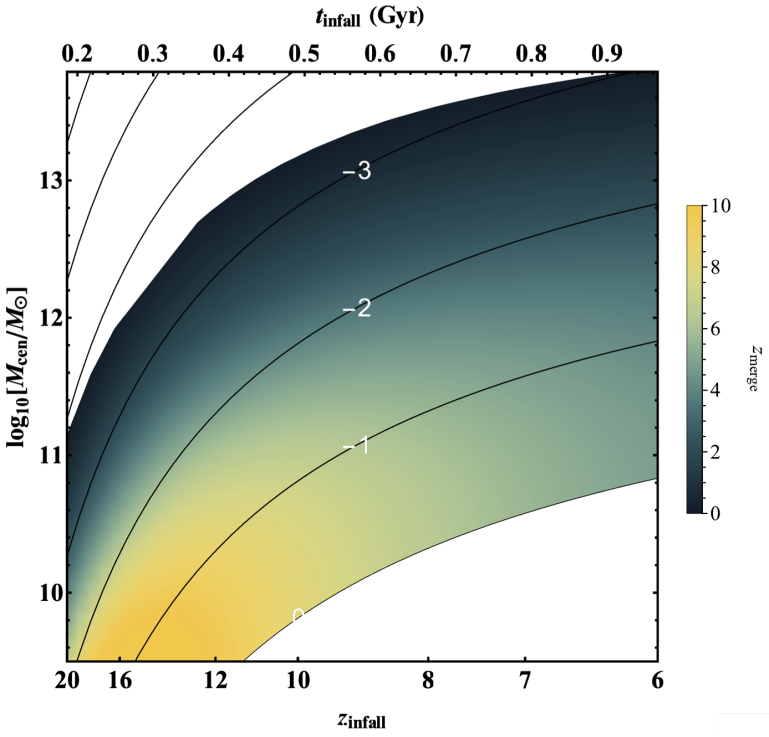

Figure 4.16 *$z_{\rm merge}$, the redshift at which an infalling satellite halo to reaches the final radius, $r = x_{\rm end}\, r_{200}$, as a function of the mass of the central halo and the redshift at which the infall begins, $z_{\rm infall}$. The satellite halo is modelled to be an atomic cooling halo at $z_{\rm seed} = 20$ which grows at $\zeta = \zeta_{\rm CR7} = 0.568$, giving $M_{\rm sat}(z_{\rm infall})$. The contours show lines of constant $\log_{10}(M_{\rm sat}/M_{\rm cen})$ (the corresponding value is shown by the white numbers). No cases with $M_{\rm p}/M_{\rm cen} > 1$ are shown. The top left undefined region indicates where the infall is not complete prior to $z = 0$.*

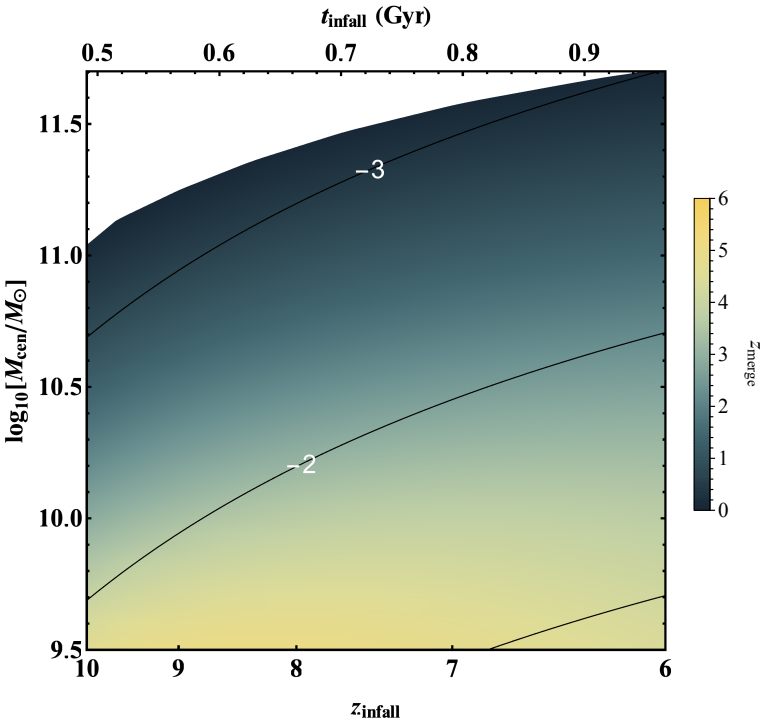

Figure 4.17 *The same as Figure 4.16 except with the satellite halo modelled to be an atomic cooling halo at* $z_{\rm seed} = 10$.

Figures 4.16 and 4.17 show the redshift at which the infall is complete for the cases of an infalling satellite subhalo with $z_{\rm seed} = 20$ and $z_{\rm seed} = 10$, respectively. The first point to notice is that the mass range for the central halo is different in the two cases. For $z_{\rm seed} = 10$ (Figure 4.17), the DCBH hosting subhalo has little time to grow prior falling in and is only a small fraction of the central halo's mass, with $M_{\rm sat}/M_{\rm cen} \lesssim 0.001$ for central halos with masses $M_{\rm cen} \gtrsim 10^{11-11.5}\,{\rm M}_\odot$. For larger central halo masses, the infall process cannot complete prior to $z = 0$, as signified by the undefined, white region at the top left of the plot. For $z_{\rm seed} = 20$, there can be more time for the DCBH host subhalo to grow and therefore for the same infall redshift the mass ratio is larger than the later seed formation case. The shorter merging times from the higher mass ratios means that $z_{\rm merge}$ is higher and larger $M_{\rm cen}$ values are required to delay infall completion past $z = 0$.

The same plots are shown for the infalling naked black hole, Figures 4.18-4.21. In the naked black hole case the perturber mass is determined by following the growth from a $10^6\,{\rm M}_\odot$ seed at $z_{\rm seed} = 20$ to $z_{\rm infall}$ using the tidal torque model. One can see from the contours of Figure 4.18 that the black hole only case results in very small mass ratios, $M_\bullet/M_{\rm cen} \sim 10^{-3}$ to $\sim 10^{-8}$. As would be expected from the analysis above (particularly from Figure 4.11), this results in very long

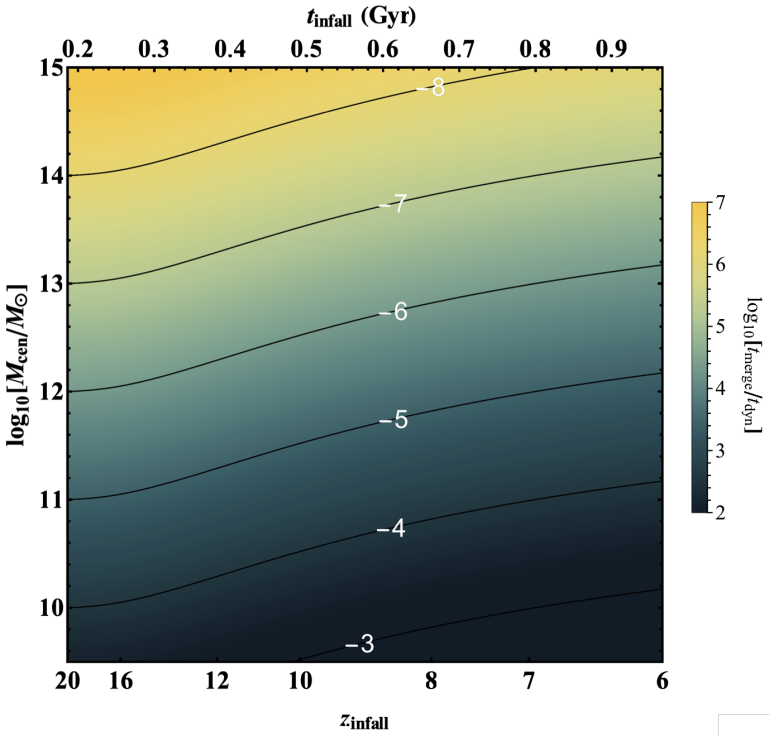

Figure 4.18 *$t_{\rm merge}$, the time it takes for an infalling naked black hole to reach the final radius, $r = x_{\rm end}\, r_{200}$, as a function of the mass of the central halo and the redshift at which the infall begins, $z_{\rm infall}$. The black hole is modelled to grow from a $10^6\,{\rm M}_\odot$ seed at $z_{\rm seed} = 20$ to $z_{\rm infall}$ using the tidal torque model. The contours show lines of constant $\log_{10}(M_\bullet/M_{\rm cen})$ (the corresponding value is shown by the white numbers). No cases with $M_{\rm p}/M_{\rm cen} > 1$ are shown.*

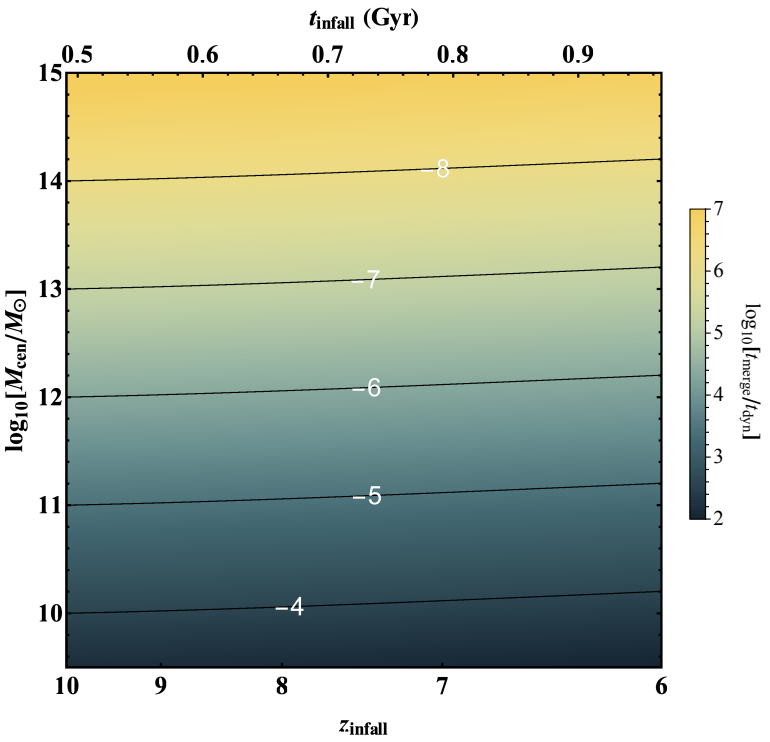

Figure 4.19 *The same as Figure 4.18 except with the naked black hole modelled to grow from a seed which formed at* $z_{\rm seed} = 10$.

merging times. We can see from Figure 4.20 that the range of central halo masses where infall completes prior to $z = 0$ is much smaller. This range decreases even further for the later seed formation redshift case, $z_{\rm seed}$. As shown in Figure 4.21, only the smallest central halos with $M_{\rm cen} \lesssim 4 \times 10^9$, are small enough so that the black hole mass can be almost $\sim 0.1\%$ of the halo mass and infall completes prior to $z = 0$.

Note that there are two apparent maxima in $z_{\rm merge}$ in Figure 4.20. The drop in $z_{\rm merge}$ as $z_{\rm infall}$ is decreased to $z \sim 13$ comes from the change in the halo dynamical time with redshift. The growth of the black hole kicks in at $z \sim 11$, increasing the mass ratio significantly and thus decreasing $t_{\rm merge}$. This is not seen in Figure 4.21 as the black hole is unable to grow sufficiently in this time frame.

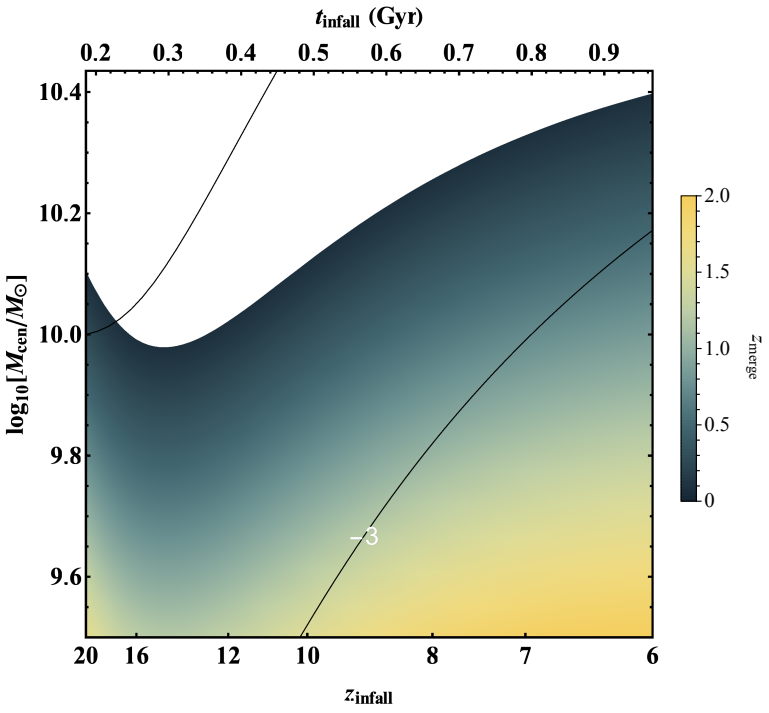

Figure 4.20 *$z_{\rm merge}$, the redshift when the naked black hole perturber reaches the final radius, $r = x_{\rm end}\, r_{200}$, as a function of the mass of the central halo and the redshift at which the infall begins, $z_{\rm infall}$. The black hole is modelled to grow from a $10^6\,{\rm M}_\odot$ seed at $z_{\rm seed} = 20$ to $z_{\rm infall}$ using the tidal torque model. The contours show lines of constant $\log_{10}(M_\bullet/M_{\rm cen})$ (the corresponding value is shown by the white numbers). No cases with $M_{\rm p}/M_{\rm cen} > 1$ are shown. The top undefined region indicates where the infall is not complete prior to $z = 0$.*

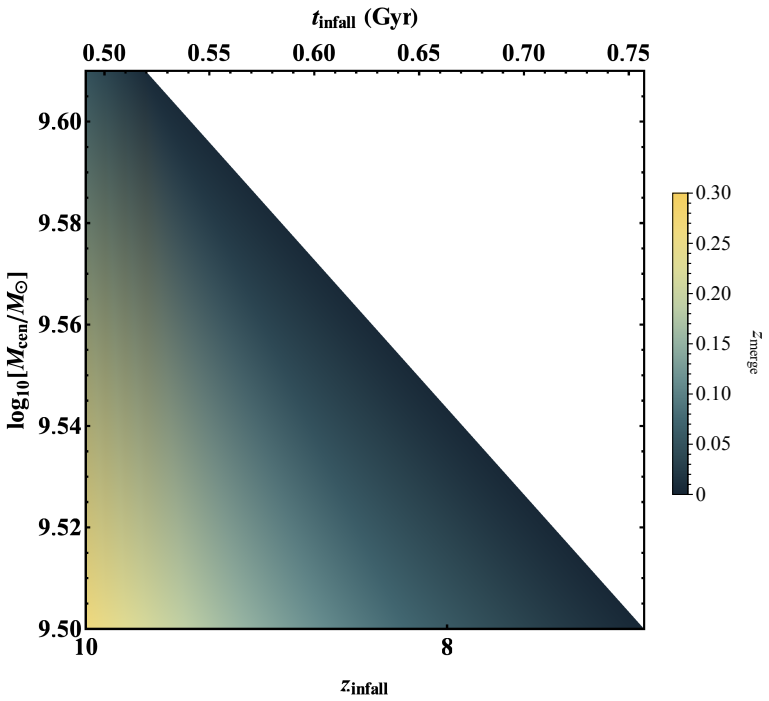

Figure 4.21 *The same as Figure 4.20 except with the naked black hole modelled to grow from a seed which formed at* $z_{\rm seed} = 10$.

4.6 Energy calculations

4.6.1 Dynamical friction heating

Dynamical friction from the halo gas acts as a drag force on the perturber. This process transfers energy from the perturber to the gas. As the dynamical friction causes the perturber to fall into the central halo, the change in the potential energy is transferred into heating the halo gas acting on the perturber. From the work done applying the frictional force $F_{\rm DF}$ to the perturber over a infinitesimal distance dl, the halo gas will gain $dE_{\rm DF}$ in heat energy,

$$dE_{\rm DF} = F_{\rm DF}.dl = F.\frac{dl}{dt}dt \tag{4.27}$$

As the perturber moves within the isothermal sphere the velocity will remain constant with $dl/dt = V_{\rm c}$. We can re-write Equation 4.27 and use the expression for the dynamical friction force (Equation 4.23) to find the rate of change of energy due to dynamical friction,

$$\frac{dE_{\rm DF}}{dt} = F_{\rm DF} V_{\rm c} \tag{4.28}$$

$$= -I\, V_{\rm c}^3 \frac{M_{\rm p}^2}{M_{\rm cen}} \frac{r_{200}}{r^2} \tag{4.29}$$

The potential energy changes with radius due to the gradient of the isothermal sphere potential,

$$\frac{1}{M_{\rm p}} \frac{dE_{\rm pot}}{dr} = \frac{d\Phi}{dr} = \frac{V_{\rm c}^2}{r} \tag{4.30}$$

Substituting this into Equation 4.29,

$$\frac{dE_{\rm DF}}{dt} = -I\, V_{\rm c} \frac{M_{\rm p}}{M_{\rm cen}} \frac{r_{200}}{r} \frac{dE_{\rm pot}}{dr} \tag{4.31}$$

$$= -I\, V_{\rm c} \frac{M_{\rm p}}{M_{\rm cen}} \frac{r_{200}}{r} \frac{dt}{dr} \frac{dE_{\rm pot}}{dt} \tag{4.32}$$

This simplifies using Equation 4.26 to become,

$$\frac{dE_{\rm DF}}{dt} = \frac{dE_{\rm pot}}{dt} \tag{4.33}$$

The change in the potential energy is converted into heat via dynamical friction. The luminosity generated through dynamical friction is calculated using the change in the potential energy from Equations 4.30 and 4.33 which gives the following expression,

$$L_{\rm DF} \equiv \frac{dE_{\rm DF}}{dt} = \frac{M_{\rm p}\, V_{\rm c}^2}{r} \frac{dr}{dt} \tag{4.34}$$

In Figure 4.22, the normalised luminosity from the energy released through dynamical friction heating is shown as a function of time since the perturbation began. Four different values are used for the mass ratio between the perturber and the central halo. With a perturber that is a larger fraction of the central halo mass, for any given time the luminosity is higher. In each case the luminosity peaks as it reaches the final radius of the calculation. The end of the calculation

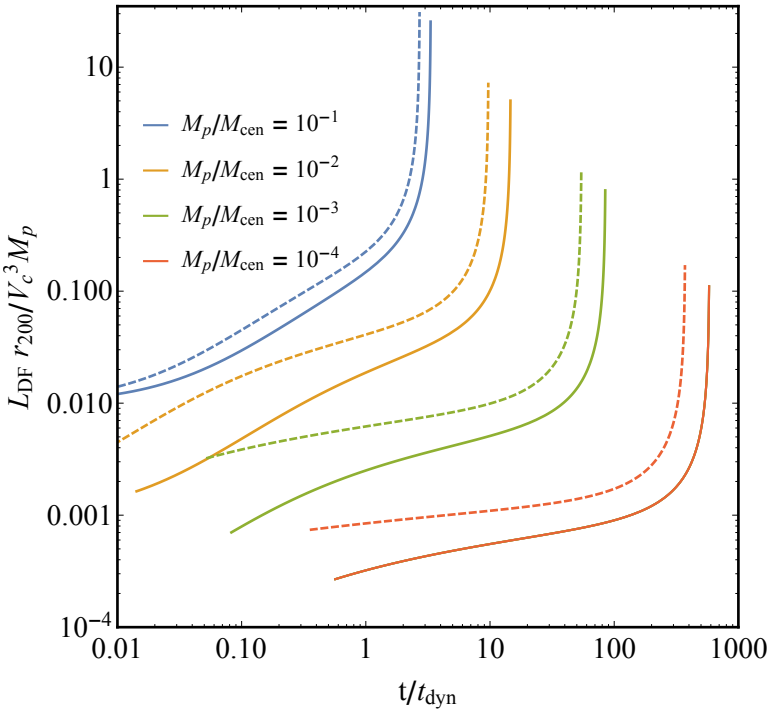

Figure 4.22 *The power (or luminosity) of the transfer of potential energy to thermal energy in the gas due to dynamical friction as a function of the time since the perturbation began. The cases shown are for four different mass ratios* $M_{sat}/M_{cen} = 10^{-4}$, 10^{-3}, 10^{-2}, *and* 10^{-1} *(as represented by the red, green, orange, and blue lines respectively). The solid lines show the infalling satellite case while the naked black hole is shown using the dashed lines.*

occurs at a later time for lower mass ratios as $t_{\rm merge}$ increases. The luminosity peaks at $r_{\rm end}$ as the radial velocity also peaking at this time while r reaches a minimum.

The total heat that goes into the gas, $\Delta E_{\rm DF}$, can be found by integrating $dE_{\rm DF}/dt$ over the full calculation (from $t = 0$ to $t = t_{\rm merge}$ or through substitution with $r = r_{200}$ to $r = r_{\rm end}$). This is simply the change in potential energy,

$$\Delta E_{\rm DF} = \Delta E_{\rm pot} = V_{\rm c}^2 M_{\rm p} \ln\left(\frac{r_{200}}{r_{\rm end}}\right) \tag{4.35}$$

4.6.2 Black hole accretion heating

Over the same timescale that infall occurs, a massive black hole within the infalling satellite subhalo will be able to grow by accreting material in the subhalo. The subhalo itself is shut off from cosmological growth and cannot grow further within the larger central halo. This effectively limits the extent to which the massive black hole can grow as it can only accrete gas which is readily available in the subhalo when it first enters the central halo. For a given black hole accretion rate, $\dot{M}_{\rm acc}$, we can express the power (or luminosity) it outputs at a given time as,

$$L_{\rm acc} = \frac{dE_{\rm acc}}{dt} = \epsilon_{\rm rad} c^2 \dot{M}_{\rm acc} \tag{4.36}$$

Integrating over time from $t = t_{\rm infall}$ to $t = t_{\rm end}$ the total energy released by the accreting black hole is,

$$\Delta E_{\rm acc} = \epsilon_{\rm rad} c^2 \Delta M_{\bullet} \tag{4.37}$$

where $\Delta M_{\bullet} = M_{\bullet}(t = t_{\rm end}) - M_{\bullet}(t = t_{\rm infall})$ which will depend on the black hole growth rate. The energy released through black hole accretion will therefore be strongly affected by the supply of gas available for accretion. Processes which can hinder black hole growth and limit the gas supply, such as star formation and feedback, will of course reduce the energy released. However, an optimistic estimate on the energy released can be calculated by considering a simplified model for black hole growth. In the case where the black hole is assumed to accrete at the Eddington rate the luminosity becomes,

$$L_{\rm Edd} = \frac{\epsilon_{\rm rad} c^2}{t_{\rm Sal}} M_{\bullet} \tag{4.38}$$

where the Salpeter timescale is $t_{\rm Sal} \sim 0.05$ Gyr (with 10 % radiative efficiency). This gives the total energy released by the accreting black hole,

$$\Delta E_{\rm Edd} = \epsilon_{\rm rad} c^2 M_{\rm infall} \left[\exp\left(\frac{t_{\rm end} - t_{\rm infall}}{t_{\rm Sal}} \right) - 1 \right] \tag{4.39}$$

where $M_{\rm infall} = M_\bullet(t = t_{\rm infall})$ and,

$$t_{\rm end} = {\rm Min}\left[t_{\rm maxBH},\, t_{\rm merge}\right] + t_{\rm infall} \tag{4.40}$$

$t_{\rm maxBH}$ is the time it takes for the black hole to reach its maximum mass during infall. As the mass of the black hole cannot become larger than the baryon fraction of the halo, this is calculated from the time required for the black hole growing at the Eddington limit to reach $M_\bullet = f_{\rm b} M_{\rm sat}$,

$$t_{\rm maxBH} = t_{\rm Sal}\, \ln\left(\frac{f_{\rm b} M_{\rm sat}}{M_{\rm infall}}\right) \tag{4.41}$$

Figure 4.23 shows this time as a function of the satellite mass for the case of $z_{\rm infall} = 8$. To find the fraction $M_{\rm sat}/M_{\rm infall}$, the satellite halo is modelled to be an atomic cooling halo at the seed formation redshift which then grows at $\zeta = \zeta_{\rm CR7} = 0.568$. The seed formation redshift, $z_{\rm seed}$, is determined by the mass of the satellite halo at infall. The black hole mass at infall can then be determined by modelling the growth of the black hole from $M_\bullet = 10^6\,{\rm M}_\odot$ at $z_{\rm seed}$ to $z_{\rm infall} = 8$ using the torque growth model. $t_{\rm maxBH}$ is independent of the central halo mass but the merging time is shown for the case of a $M_{\rm cen} = 10^{11}\,{\rm M}_\odot$ central halo for comparison. Where $t_{\rm merge} > t_{\rm maxBH}$ the black hole will reach its maximum mass (i.e. $M_\bullet(t_{\rm maxBH}) = f_{\rm b} M_{\rm sat}(t_{\rm infall})$) prior to the end of infall and will cease growing. This is the case for $M_{\rm sat}/M_{\rm cen} \lesssim 0.16$. For higher central halo masses (or lower $M_{\rm sat}/M_{\rm infall}$) the merging time increases and $t_{\rm maxBH}$ will remain small. As the black hole growth is limited by the available material it will not be able to remain accreting over the full infall period. The total energy output from the black hole cannot exceed,

$$\Delta E_{\rm Edd,\,max} = \epsilon_{\rm rad} c^2 (f_{\rm b} M_{\rm sat} - M_{\rm infall}) \approx \epsilon_{\rm rad} c^2 f_{\rm b} M_{\rm sat} \tag{4.42}$$

where the approximation holds for $M_{\rm infall}/M_{\rm sat} << 1$. For $t_{\rm merge} > t_{\rm maxBH}$ and $M_{\rm infall}/M_{\rm sat} << 1$, the ratio of the change in energies becomes,

$$\frac{\Delta E_{\rm Edd,\,max}}{\Delta E_{\rm DF}} \approx \frac{\epsilon_{\rm rad} c^2 f_{\rm b}}{\ln\left(r_{200}/r_{\rm end}\right) V_{\rm c}^2} \tag{4.43}$$

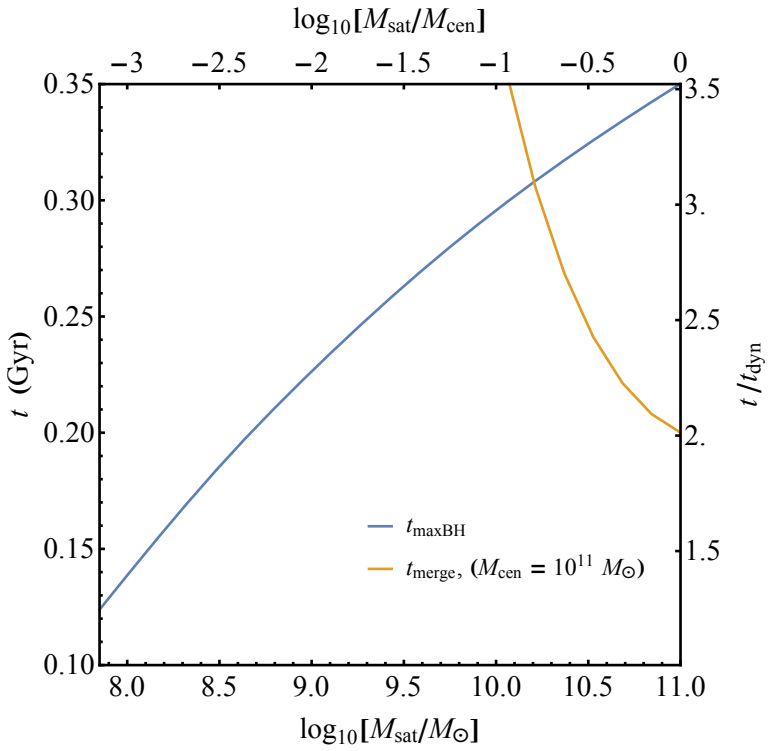

Figure 4.23 *The time needed since infall for a black hole growing at the Eddington limit to reach maximum mass (i.e.* $M_\bullet(t_{\rm maxBH}) = f_{\rm b} M_{\rm sat}(t_{\rm infall})$*), as a function of the satellite mass. The case shown is for* $z_{\rm infall} = 8$*. The satellite halo is modelled to be an atomic cooling halo at the seed formation redshift which then grows at* $\zeta = \zeta_{\rm CR7} = 0.568$*. The seed formation redshift,* $z_{\rm seed}$*, is determined by the mass of the satellite halo at infall. The black hole mass at infall is determined by modelling the growth of the black hole from* $M_\bullet = 10^6\,{\rm M}_\odot$ *at* $z_{\rm seed}$ *to* $z_{\rm infall} = 8$ *using the torque growth model. The merging time is shown for the case of a* $M_{\rm cen} = 10^{11}\,{\rm M}_\odot$ *central halo for comparison.*

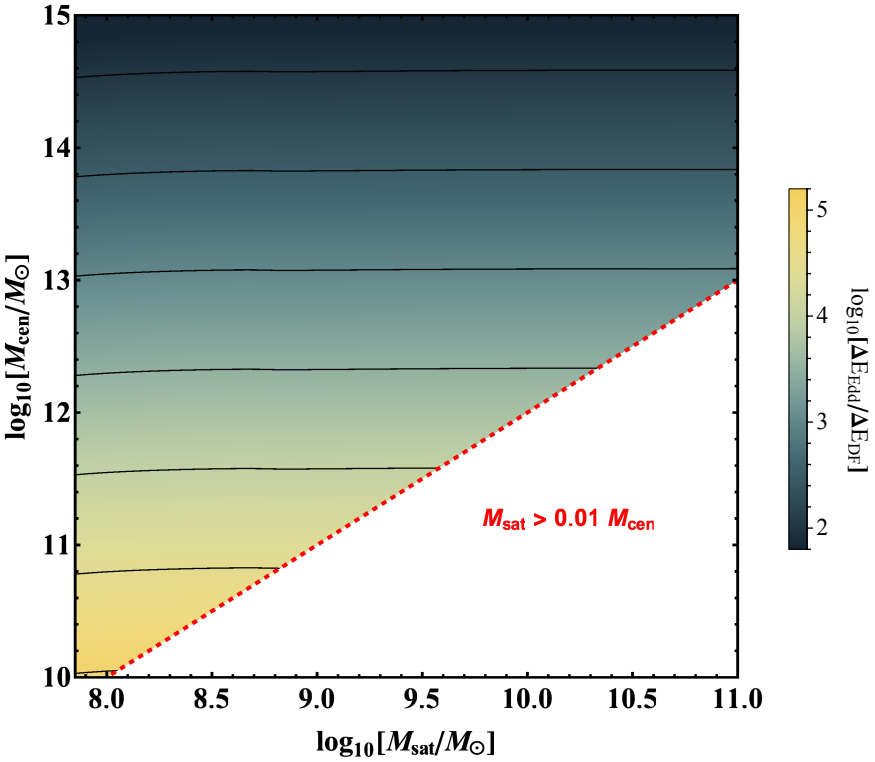

Figure 4.24 *The ratio of the heating from Eddington accretion to the heating due to dynamical friction on the infalling satellite, shown as a function of the satellite and central halo masses. The case shown is for* $z_{\rm infall} = 8$. *The satellite halo is modelled to be an atomic cooling halo at the seed formation redshift which then grows at* $\zeta = \zeta_{\rm CR7} = 0.568$. *The seed formation redshift,* $z_{\rm seed}$, *is determined by the mass of the satellite halo at infall.*

4.6.3 Eddington limited accretion

The ratio of $\Delta E_{\rm Edd}/\Delta E_{\rm DF}$ can be found using Equations 4.39 and 4.35 for a given pair of masses, $M_{\rm sat}$ and $M_{\rm cen}$ and an infall redshift. The initial black hole mass at infall can be calculated from the satellite mass using the torque-driven accretion model for black hole growth. Given a satellite mass at infall, we can calculate the redshift at which the satellite was at the atomic cooling halo mass by assuming a halo growth rate $\zeta = \zeta_{\rm CR7}$. The black hole is assumed to form at this redshift with a mass of $M_{\rm seed} = 10^6\,{\rm M}_\odot$, the fiducial torque-driven accretion model can calculate the black hole mass at infall.

Due to the limitations of the dynamical friction calculation, the mass range is limited to mass ratios below $M_{\rm sat}/M_{\rm cen} < 0.01$. Within this regime, $t_{\rm merge} > t_{\rm maxBH}$, while the other assumption made in finding Equation 4.43, $M_{\rm infall}/M_{\rm sat} << 1$, will hold for all but the smallest satellite subhalo masses

where $M_{\rm infall}/M_{\rm sat} \gtrsim 0.01$. As the circular velocity scales with the mass of the central halo ($V_{\rm c}^2 = GM_{\rm cen}/r_{200}$), and the dependence of $\Delta E_{\rm Edd}/\Delta{\rm DF} \propto 1/M_{\rm cen}$ is apparent in Figure 4.24.

While a black hole accreting at its Eddington limit would initially generate more power than dynamical friction which could heat the halo gas, the release of energy from black hole growth is not maintained throughout infall as black hole growth shuts off towards the end of the infall process (Figure 4.23). The total energy released over the infall of a DCBH host via dynamical friction heating does not exceed the heating from Eddington limited black hole accretion (Figure 4.24). On the other hand, Figure 4.22 implies that dynamical friction heating should be highest at the end of the calculation when the perturber is at $r_{\rm end}$. For low $M_{\rm sat}/M_{\rm cen}$, $t_{\rm maxBH} < t_{\rm merge}$ as the black hole accretes all of the gas available in the host subhalo prior to the end of the infall period. Therefore, when the luminosity from dynamical friction is at a maximum there should be no heating from black hole accretion.

4.6.4 Viscosity-driven inflow

Figure 4.25 shows $\Delta E_{\rm visc}/\Delta E_{\rm DF}$, the ratio of the heating from black hole accretion fed via viscosity-driven inflow to the heating due to dynamical friction on an infalling satellite halo, as a function of the satellite and central halo masses at $z_{\rm infall} = 8$. The initial black hole mass at infall is calculated in the same fashion as described for the Eddington limited case except the viscosity-driven accretion model is used to follow the evolution of the system.

Following the onset of infall, the calculation of the system's evolution is continued over $t_{\rm merge}$ to find the final black hole mass. In this period the subhalo can no longer grow and any change in the disc mass comes from feeding black hole accretion. Also at this stage, to allow for maximum black hole growth, star formation is artificially inhibited.

The viscosity-driven inflow rate is generally lower than the Eddington rate, especially for large black hole masses (e.g. Figure 4.2. Also see Chapter 3). Therefore, black hole masses and growth rates will be lower in the viscosity-driven case than the Eddington limited case above. As $\Delta E_{\rm DF}$ is the same in both cases, we can see by comparing the $\Delta E_{\rm acc}/\Delta E_{\rm DF}$ ratios in Figures 4.24 and 4.25, the energy released through accretion is consistently lower in the

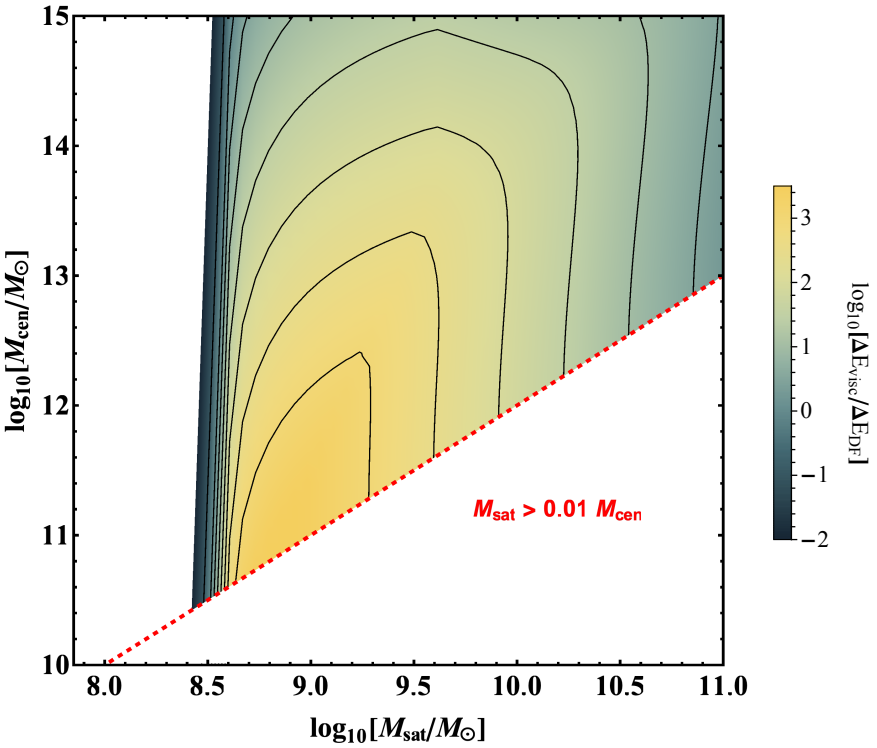

Figure 4.25 *The ratio of the heating from black hole accretion fed via viscosity-driven inflow to the heating due to dynamical friction on the infalling satellite, shown as a function of the satellite and central halo masses. The case shown is for* $z_{\rm infall} = 8$*. The satellite halo is modelled to be an atomic cooling halo at the seed formation redshift which then grows at* $\zeta = \zeta_{\rm CR7} = 0.568$*. The seed formation redshift,* $z_{\rm seed}$*, is determined by the mass of the satellite halo at infall.*

viscosity-driven case; for any given pair of central and satellite halo masses, $\Delta E_{\rm visc}/\Delta E_{\rm DF} < \Delta E_{\rm Edd}/\Delta E_{\rm DF}$. For $\ln(M_{\rm sat}/M_\odot) \lesssim 8.4$, there is no black hole growth as the disc is fully stabilised at the onset of infall. Therefore, in this region with low perturber mass there is no heating from black hole accretion.

Away from the region where black hole growth is inhibited, the $\Delta E_{\rm visc}/\Delta E_{\rm DF}$ ratio peaks around $\log_{10}(M_{\rm sat}/M_\odot) \sim 9$, $\log_{10}(M_{\rm cen}/M_\odot) \sim 11.1$. It decreases for larger $M_{\rm cen}$ and $M_{\rm sat}$, decreasing to around $\Delta E_{\rm visc}/\Delta E_{\rm DF} \sim 1$ at $\log_{10}(M_{\rm sat}/M_\odot) = 11$. The decrease with $M_{\rm cen}$ is due to $\Delta E_{\rm DF} \propto V_{\rm c}^2 \propto M_{\rm cen}^{2/3}$ (Equation 4.27) while the accretion energy is independent of the central halo mass. $\Delta E_{\rm DF}$ increases with the perturber mass while any increase in $\Delta E_{\rm visc}$ is less significant. As we increase the perturber mass, the formation redshift of the subhalo must increase. The increase in the time between the formation of the seed and the onset of infall means that the black hole has had more time to grow prior to infall. The infall timescale also decreases, meaning a larger fraction of the black hole's growth occurs prior to infall and as such the energy released during infall $\Delta E_{\rm visc}$ will not simply scale with the final mass. In the Eddington limited case, the mass of the black hole at infall is well below the maximum value $M_\bullet = f_{\rm b} M_{\rm sat}$. Here however, the disc will quickly stabilises against further inflow after the subhalo ceases to be fed through cosmological accretion.

4.6.5 Torque-driven inflow

Figure 4.26 shows $\Delta E_{\rm Torq}/\Delta E_{\rm DF}$, the ratio of the heating from black hole accretion fed via torque-driven inflow to the heating due to dynamical friction on an infalling satellite halo, as a function of the satellite and central halo masses at $z_{\rm infall} = 8$. The initial black hole mass at infall is calculated in the same fashion as described for the Eddington limited case.

Similarly to the viscosity-driven case, following the onset of infall, the calculation of the system's evolution is continued over $t_{\rm merge}$ to find the final black hole mass. Again, in this period the subhalo can no longer grow and star formation is artificially inhibited.

The torque-driven inflow rate is generally lower than the Eddington rate (e.g. Figure 4.2). The torque-driven inflow model is comparable to the viscosity model at early times but as the system evolves, the torque-driven black hole growth exceeds the viscosity model, leading to larger black hole masses. Therefore,

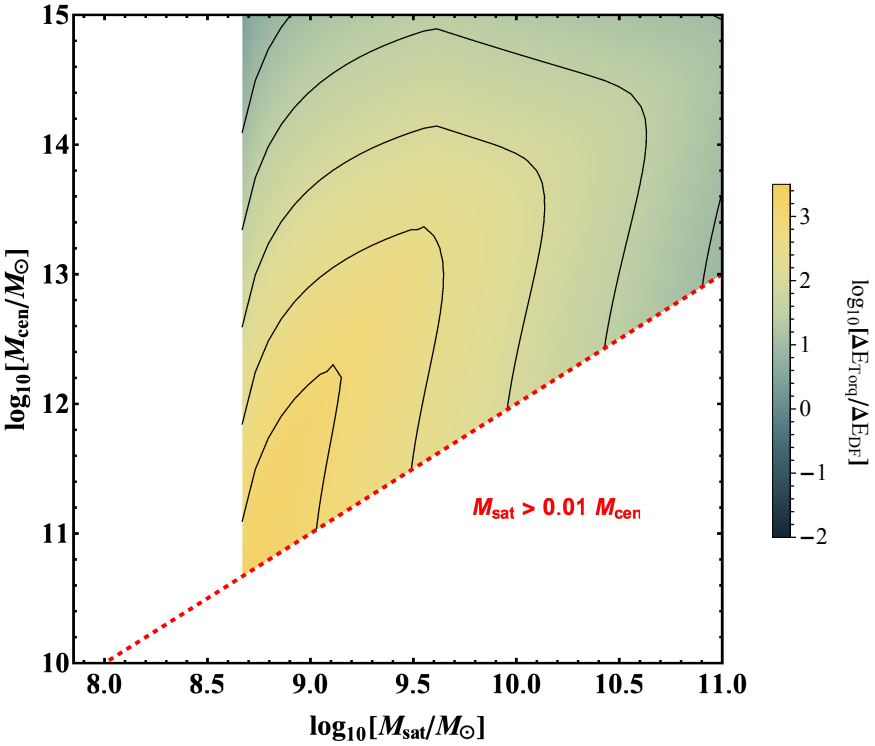

Figure 4.26 *The ratio of the heating from black hole accretion fed via torque-driven inflow to the heating due to dynamical friction on the infalling satellite, shown as a function of the satellite and central halo masses. The case shown is for* $z_{\rm infall} = 8$*. The satellite halo is modelled to be an atomic cooling halo at the seed formation redshift which then grows at* $\zeta = \zeta_{\rm CR7} = 0.568$*. The seed formation redshift,* $z_{\rm seed}$*, is determined by the mass of the satellite halo at infall.*

the change in black hole masses will be lower in the torque-driven case than the Eddington limited case, but higher than the viscosity-driven case. Again, $\Delta E_{\rm DF}$ is the same as the previous two cases. Comparing the $\Delta E_{\rm acc}/\Delta E_{\rm DF}$ ratios in Figures 4.24 and 4.25 with Figure 4.26 we can see that the energy released through accretion is consistently lower in the torque-driven case than the Eddington limited case; for any given pair of central and satellite halo masses, $\Delta E_{\rm Torq}/\Delta E_{\rm DF} < \Delta E_{\rm Edd}/\Delta E_{\rm DF}$. For $\ln(M_{\rm sat}/M_\odot) \lesssim 8.6$, there is no black hole growth as the disc is fully stabilised at the onset of infall. With the torque-driven model, the region where there is no heating from black hole accretion is slightly larger than the viscosity-driven case as the larger black hole mass at a given satellite mass can stabilise higher disc masses.

At $\log_{10}(M_{\rm sat}/M_\odot) \sim 8.8$, $\log_{10}(M_{\rm cen}/M_\odot) \sim 11.1$, $\Delta E_{\rm Torq}/\Delta E_{\rm DF}$ reaches a maximum. The variation in the ratio away from the maximum, is similar to trend in the viscosity case however the change is less extreme. Again the decrease in the ratio for increasing central mass is consistent with the $\Delta E_{\rm DF} \propto V_{\rm c}^2 \propto M_{\rm cen}^{2/3}$ dependence. The stability of the disc means the final black hole mass scales weakly with $M_{\rm sat}$ and an increase in $\Delta E_{\rm Torq}$ with $M_{\rm sat}$ is less significant than the increase in $\Delta E_{\rm DF}$.

4.6.6 Emission from dynamically heated gas

When the gas is heated dynamically by the motion of the perturber, the increase in the kinetic energy in the gas will raise rates of collisional excitation from which de-excitation will lead to cooling through emission. Which species are excited will depend on the metallicity and the temperature of the gas. As we have assumed the central halo is the local source of LW radiation which enabled the DCBH formation, we can infer it has efficiently been forming stars and will be approaching solar metallicity (though there is a wide range of possible metallicities, e.g. Juarez et al. 2009; Izotov et al. 2015). The temperature of the gas in the model will vary with the mass of the central halo. For a $M_{\rm cen} \sim 10^{11}\,{\rm M}_\odot$ halo at $z = 6$, we can estimate the gas temperature by assuming virial equilibrium and using Equation 4.11 to calculate $T_{\rm gas} \sim 5 \times 10^5$ K. The dynamical friction heating rate may reach equilibrium with the radiative cooling rate. At this temperature and metallicity, the gas will primarily cool through metal-line emission (Sutherland & Dopita 1993; Dopita & Sutherland 1996). Dynamical friction heating would therefore in this case lead to an increase in

the bolometric luminosity of the system. The resulting spectrum would differ from quasar spectra through a flatter UV slope in the absence of an accretion disc (Wandel & Petrosian 1988).

4.7 Discussion & Summary

In this study I modelled the dynamical heating of gas in dark matter haloes through the infall of massive black holes and their host subhaloes. An infalling perturber, whether it is a naked black hole or a subhalo, experiences a gravitational drag force from the gas and dark matter in the massive central halo (Chandrasekhar 1943; Ostriker 1999). This force simultaneously aids the infall process by reducing the angular momentum of the perturber while heating the gas acting on the perturber as it passes through. Making a number of assumptions, I calculate the drag force using Equation 4.13 which describes the force on a low mass perturber moving through a uniform gas at constant velocity (Ostriker 1999). By further assuming the perturber's orbit remains approximately circular and dynamical friction acts purely in the tangential direction of the orbit, I find an expression for the radial velocity. This can be solved numerically to determine the change in orbital radius over time as the orbit decays.

I calculate the merging time, the time for the perturber to reach the central galaxy of the halo, and find it is strongly dependent on the relative masses of the perturber and the halo. Except for cases where the central halo is relatively low in mass, $M_{\rm cen} \sim 10^{9-10}\,{\rm M}_{\odot}$, for most naked black holes this timescale is too long for the black hole to reach the central galaxy by $z = 6$, or even $z = 0$ for that matter. A naked black hole would have to have grown to $M_{\bullet} \sim 10^{8-9}\,{\rm M}_{\odot}$ prior to infall occuring to reduce this timescale sufficiently, requiring a growth efficiency not reached by either the visocity- or gravitational-torque-driven inflow rate models.

For the case where the perturber is an infalling satellite halo hosting a massive black hole, I compare the energy released through dynamical heating to the energy released from black hole growth. The halo gas generally receives more energy from black hole accretion heating $\Delta E_{\rm acc}$ than dynamical friction heating $\Delta E_{\rm DF}$. However, black hole accretion rates vary significantly between the black hole growth models and the heating from black hole accretion depends strongly on the model used. In the case of Eddington limited growth, $\Delta E_{\rm Edd}/\Delta E_{\rm DF} > 1$

for the range of satellite and central halo masses explored here. For the cases of viscosity-driven and torque-driven inflow feeding black hole growth the black hole growth rates are much lower and the ratios $\Delta E_{\rm visc}/\Delta E_{\rm DF}$ and $\Delta E_{\rm Torq}/\Delta E_{\rm DF}$ vary more with the mass of the satellite. In both inflow-limited cases heating from dynamical friction is important for both low and high mass satellites but is less significant for satellites with masses around $M_{\rm sat} \sim 10^9\,{\rm M}_\odot$. Again in both cases, low mass satellites $M_{\rm sat} \lesssim 3 \times 10^8\,{\rm M}_\odot$ experience no black hole growth as there is no inflow from the discs in the subhalo being stabilised against gravitational instabilities. At the high mass satellite end, the energy ratio at $M_{\rm sat} \sim 10^{11}\,{\rm M}_\odot$ is $\Delta E_{\rm acc}/\Delta E_{\rm DF} \sim 1$. As the black hole growth rates are generally lower for the viscosity-driven model than for the torque-driven model, the heating from black hole accretion in the viscosity-driven case will be lower.

Even in the Eddington case where $\Delta E_{\rm acc}$ is highest, the dynamical friction heating will be important at late times, when the perturber is close to the final radius. For $M_{\rm p}/M_{\rm cen} \lesssim 0.1$, this period coincides with the point during infall when the accretion onto the black hole has ceased and when the luminosity peaks.

This potentially has significant consequences for inferences of black hole masses. Though I have not considered how much this heating is spread out spatially, we do know that dynamical friction is strongest close in to the perturber. If dynamical friction heating is significant close to the black hole it may contribute to the total bolometric luminosity. This could lead to over-estimates of black hole masses inferred from luminosities (often done by assuming the black hole is growing at the Eddington limit, $M_\bullet \sim L_{\rm bol} t_{\rm Sal}/\epsilon c^2$). The impact this could have on black hole masses determined through spectroscopy (Mortlock et al. 2011; De Rosa et al. 2014; Bañados et al. 2018) is somewhat limited as these studies use a range of quasar emission lines which are thought to come from the region very close to the accretion disc. However, this does help to show the importance of spectroscopic studies for determining black hole masses.

4.7.1 Caveats with the model

The dynamical friction force derivation from Ostriker (1999) made use of several assumptions and was found through linear perturbation analysis. This means that within the derivation the perturber is assumed to be of low mass. In the case of a higher mass perturber the modifications to the density field become non-linear. This limits the applicability of Equation 4.13 and the results shown here

as the relationship may not hold for higher mass perturbers where the assumption of $M_{\rm p}/M_{\rm cen} << 1$ is not true.

A further weakness of the analytic approach is that by using the Ostriker (1999) dynamical friction calculation, we have implicitly assumed the perturber can be treated as a point mass. As discussed above, there is explicitly some size to the perturber which is used in the definition of $r_{\rm min}$. However, Equations 4.13 and 4.14 will not hold if the perturber is significantly extended. Indeed, in the case of an infalling satellite, the outer parts of the satellite will be stripped under tidal forces from the central halo (see, e.g. Nichols et al. 2015). This would result in potential rapid mass loss, greatly reducing the dynamical friction force and increasing the merging time. In extreme cases the satellite merging time could exceed the Hubble time as only a central compact region of the original satellite would remain. In turn any energy released through dynamical friction heating would be greatly reduced. Further study of the infalling DCBH host case would therefore require a numerical investigation into this scenario to test the extent to which tidal forces impact these results. For the naked black hole case, the size of the perturber (the Bondi radius) is generally small enough that the point mass assumption is valid (Kim & Kim 2009).

Particles in quasi-equilibrium within an isothermal sphere will move at the circular velocity, $V_{\rm c}$. As the central halo is modelled as an isothermal sphere, the assumption of a constant velocity of the perturber is sound. However, the background density through which the perturber moves is not uniform. The perturbation wake grows over time. In the radial direction, perpendicular to the direction of travel, the speed of the wake is the sound speed. As the density of the isothermal sphere varies with $\rho(r) \propto 1/r^2$, after a short time the approximation that the background density of the region covered by the wake, $\rho(r) \approx \rho_0$, would no longer hold. This would change the growth of the wake and have an effect on Equations 4.15 and 4.16.

I next hope to investigate whether the break down in the assumptions of the model have a profound effect on the implications of this work. Hydrodynamic simulations have suggested that the linear perturbation calculation for dynamical friction can lead to an over-estimate in the strength of the gravitational drag experienced by a perturber (Kim & Kim 2009). In a simulation the fluid equations are solved at each point and as such dynamical friction does not need to be explicitly implemented, given sufficient resolution. Using a numerical approach means that dynamical friction can be implemented implicitly and further allows

for the inclusion of cosmologically-consistent halo density profiles, and feedback effects (e.g. Davé et al. 2019; Hopkins et al. 2018). Each of these modelling aspects would impact the density of the gas and dark matter in the halo, dramatically changing the dynamical friction force and the resulting heating could be remarkably different from the values calculated here.

Chapter 5

Conclusion

In undertaking the research discussed in this thesis I set out to investigate how massive seed black holes formed through direct collapse can influence their host galaxies as they grow. I have used analytic modelling techniques to study the impact of massive black holes in a number of scenarios.

I first developed an analytic model which followed the growth of a proto-galaxy at high redshift, centred on a massive seed black hole formed through the direct collapse mechanism. By taking into account the feeding of the galaxy's disc from cosmological accretion and its depletion through the growth of the black hole, I was able to determine the evolution of the system as a whole. I find that the gravitational influence of the black hole has a stabilising effect on the disc which, combined with black hole growth depleting the mass of the disc, can reduce the size of the region of the disc where stars form and the total star formation rate. For late seed black hole formation ($z \sim 10$), the growth of even the most massive seed black holes into SMBHs by $z \sim 6$ will inhibit star formation from gravitational disc instabilities within the black holes' host galaxies. Earlier seed formation times can allow for the host to grow in stellar mass however, the onset of star formation can still be delayed.

By making an adaption to the analytic model whereby the black hole growth was fed via disc viscosity-driven inflow, I was able to instead test whether massive seed black holes could achieve the necessary growth to become super-massive by $z \sim 6$. I found that viscosity-driven inflow is far too in-efficient to feed the growth of SMBHs in an isolated system. However, a single major merger event is capable of disrupting the disc sufficiently to drive material into the black hole.

This implies that mergers and environmental effects have an important role to play in the formation of SMBHs.

The findings of both of these studies are made stronger when one considers that these upper limits on stellar and black hole growth were found without considering the effects of feedback, either from black hole growth or stars. With the inclusion of feedback, the added heating and outflow of gas would generally be expected to reduce the ability of black holes to grow further (Johnson et al. 2011; Dubois et al. 2015; Latif et al. 2018) - although positive feedback mechanisms are also possible (see, e.g. Di Matteo et al. 2005) - and AGN feedback is one of the most popular mechanisms used to explain star formation quenching at low redshift (Somerville & Davé 2015).

While my work has shown that isolated systems do not grow to match the observed correlations between black holes and their host galaxies at low redshift, cosmological simulations (e.g. Davé et al. 2019) are able to recreate the scaling relations observed in the local universe. A future study could investigate whether the mechanisms I have identified as significant in my analytic model are no longer important within the cosmological environment of a simulation. For example, with high resolution, cosmological zoom simulations of massive seed hosting galaxies (such as those performed by Latif et al. 2018), one could test whether the gravitational influence of a black hole has an impact on star formation in its host galaxy. A similar test could be done by using the model for viscosity-driven black hole growth within a semi-analytic model. My work has suggested that environmental effects likely play a significant role in the growth of SMBHs and their host galaxies. With halo growth rates from N-body simulations one will be able to test how the picture of black hole growth changes in a range of environments.

The first two studies of this thesis have both lent some weight to an emerging picture for the potential growth of SMBHs seeded through direct collapse whereby the massive seeds originally form in separate haloes to their eventual host galaxies (see, e.g. Agarwal et al. 2014). The final chapter of this thesis was aimed at one aspect of this developing picture of SMBH growth: investigating the effects of massive seed black hole systems falling into a larger, central halo. Using an analytic approach, I modelled the heating of the central halo gas through the dynamical friction acting on the perturbing satellite. I found that the time it takes for the perturber to reach some final radius decreases for larger values of the ratio between mass of the satellite and the mass of the central halo. For a

given central halo mass, this timescale becomes very large for low mass perturbers, effectively ruling out the accretion of naked black holes onto galaxies by $z \sim 6$.

Faster infall is possible with a higher perturber mass, such as a subhalo. If the black hole remains in its subhalo during the infall process (which is not guaranteed Condon et al. 2017; van den Bosch 2017), the black hole will be able to accrete material from the subhalo, releasing energy. By comparing the energy released through black hole accretion to the energy released via dynamical friction heating during infall, I find that black hole growth generally provides more heating however the energy released varies significantly with the black hole growth model used. In most cases, a black hole growing at the Eddington limit is found to accrete all of the available material prior to the end of the infall process. There is therefore a period of time where the primary source of heating in the halo from the infalling satellite comes is as a result of dynamical friction. Assuming this energy is able to escape as radiative, this additional heating will contribute to the total luminosity of the system and potentially lead to over-estimates in the black masses inferred from bolometric luminosity arguments. Future work on this study will also benefit from the use of cosmological, hydrodynamical simulations to more accurately follow the decay of the perturber through dynamical friction while also tracking the sources of heating in the central halo.

Bibliography

Abbott B. P., et al., 2016, Physical Review Letters, 116, 061102

Agarwal B., et al., 2012, MNRAS, 425, 2854

Agarwal B., et al., 2014, MNRAS, 443, 648

Agarwal B., et al., 2016a, MNRAS, 459, 4209

Agarwal B., et al., 2016b, MNRAS, 460, 4003

Agarwal B., et al., 2018, preprint, p. arXiv:1808.09981 (arXiv:1808.09981)

Agertz O., Teyssier R., Moore B., 2009, MNRAS, 397, L64

Alvarez M. A., Bromm V., Shapiro P. R., 2006, ApJ, 639, 621

Alvarez M. A., Wise J. H., Abel T., 2009, Astrophys. J., 701, L133

Anglés-Alcázar D., Özel F., Davé R., 2013, ApJ, 770, 5

Anglés-Alcázar D., et al., 2015, ApJ, 800, 127

Anglés-Alcázar D., et al., 2017, MNRAS, 464, 2840

Bañados E., et al., 2018, Nature, 553, 473

Baldry I. K., et al., 2004, ApJ, 600, 681

Barnes J. E., Hernquist L., 1996, ApJ, 471, 115

Beckmann R. S., Slyz A., Devriendt J., 2018, MNRAS, 478, 995

Begelman M. C., 2010, MNRAS, 402, 673

Begelman M. C., Volonteri M., Rees M. J., 2006, MNRAS, 370, 289

Binney J., Tremaine S., 2008, Galactic Dynamics: Second Edition

Blumenthal G. R., et al., 1984, Nature, 311, 517

Bondi H., 1952, MNRAS, 112, 195

Bondi H., Hoyle F., 1944, MNRAS, 104, 273

Bongiorno A., et al., 2016, A&A, 588, A78

Bournaud F., et al., 2011, ApJ, 741, L33

Bowler R. A. A., et al., 2017, MNRAS, 469, 448

Bromm V., Loeb A., 2003, ApJ, 596, 34

Bromm V., Coppi P. S., Larson R. B., 1999, ApJ, 527, L5

Bromm V., et al., 2009, Nature, 459, 49

Carilli C. L., Walter F., 2013, Annual Review of Astronomy and Astrophysics, 51, 105

Ceverino D., Dekel A., Bournaud F., 2010, MNRAS, 404, 2151

Chabrier G., 2003, Publications of the Astronomical Society of the Pacific, 115, 763

Chandrasekhar S., 1943, ApJ, 97, 255

Chon S., et al., 2016, ApJ, 832, 134

Clark P. C., Glover S. C. O., Klessen R. S., 2008, ApJ, 672, 757

Condon J. J., et al., 2017, ApJ, 834, 184

Correa C. A., Schaye J., Trayford J. W., 2019, MNRAS, 484, 4401

D'Onghia E., et al., 2006, MNRAS, 372, 1525

Davé R., et al., 2019, MNRAS, 486, 2827

De Loore C. W. H., Doom C., 1992, Structure and evolution of single and binary stars. Vol. 179, Springer, Dordrecht, doi:10.1007/978-94-011-2502-4

De Lucia G., et al., 2012, MNRAS, 423, 1277

De Rosa G., et al., 2014, ApJ, 790, 145

Dekel A., Sari R., Ceverino D., 2009, ApJ, 703, 785

Dekel A., et al., 2013, MNRAS, 435, 999

Del Moro A., et al., 2016, MNRAS, 456, 2105

Delvecchio I., et al., 2015, MNRAS, 449, 373

Devecchi B., Volonteri M., 2009, ApJ, 694, 302

Devecchi B., et al., 2010, MNRAS, 409, 1057

Di Matteo T., Springel V., Hernquist L., 2005, Nature, 433, 604

Di Matteo T., et al., 2008, ApJ, 676, 33

Dib S., Bell E., Burkert A., 2006, ApJ, 638, 797

Dijkstra M., et al., 2008, MNRAS, 391, 1961

Dopita M. A., Sutherland R. S., 1996, ApJS, 102, 161

Dubois Y., et al., 2015, MNRAS, 452, 1502

Eastwood D. S., Khochfar S., 2018, MNRAS, 480, 5673

Eastwood D. S., Khochfar S., Trew A., 2019, MNRAS, 488, 2006

Edgar R., 2004, New A Rev., 48, 843

Eisenstein D. J., Loeb A., 1995, Astrophys. J., 443, 11

Elmegreen B. G., Burkert A., 2010, ApJ, 712, 294

Elmegreen D. M., et al., 2005, ApJ, 631, 85

Elmegreen D. M., et al., 2007, ApJ, 658, 763

Fabian A. C., 2012, ARA&A, 50, 455

Fall S. M., Efstathiou G., 1980, MNRAS, 193, 189

Fan X., et al., 2003, AJ, 125, 1649

Fan X., et al., 2006, AJ, 132, 117

Fanidakis N., et al., 2012, MNRAS, 419, 2797

Ferrarese L., Merritt D., 2000, ApJ, 539, L9

Gabor J. M., et al., 2010, MNRAS, 407, 749

Gebhardt K., et al., 2000, ApJ, 539, L13

Genel S., et al., 2008, ApJ, 688, 789

Glebbeek E., et al., 2009, Astron. Astrophys., 497, 255

Governato F., Colpi M., Maraschi L., 1994, MNRAS, 271

Greif T. H., et al., 2008, MNRAS, 387, 1021

Greif T. H., et al., 2010, ApJ, 716, 510

Gurzadian V. G., Ozernoi L. M., 1979, Nature, 280, 214

Häring N., Rix H.-W., 2004, ApJ, 604, L89

Heckman T. M., Best P. N., 2014, ARA&A, 52, 589

Heger A., et al., 2003, Astrophys. J., 591, 288

Henley D. B., et al., 2010, ApJ, 723, 935

Hewlett T., et al., 2017, MNRAS, 470, 755

Hickox R. C., et al., 2014, ApJ, 782, 9

Hirschmann M., et al., 2010, MNRAS, 407, 1016

Hirschmann M., et al., 2012, MNRAS, 426, 237

Hopkins P. F., Quataert E., 2011, MNRAS, 415, 1027

Hopkins P. F., et al., 2006, The Astrophysical Journal Supplement Series, 163, 1

Hopkins P. F., et al., 2009, ApJ, 691, 1168

Hopkins P. F., et al., 2018, MNRAS, 480, 800

Hosokawa T., et al., 2013, ApJ, 778, 178

Hosokawa T., et al., 2016, ApJ, 824, 119

Hoyle F., Lyttleton R. A., 1941, MNRAS, 101, 227

Hunter D. A., Elmegreen B. G., van Woerden H., 2001, ApJ, 556, 773

Inayoshi K., Haiman Z., Ostriker J. P., 2016, MNRAS, 459, 3738

Izotov Y. I., et al., 2015, MNRAS, 451, 2251

Johnson J. L., Bromm V., 2007, Mon. Not. R. Astron. Soc., 374, 1557

Johnson J. L., et al., 2011, MNRAS, 410, 919

Johnson J. L., et al., 2013, ApJ, 771, 116

Juarez Y., et al., 2009, A&A, 494, L25

Juneau S., et al., 2013, ApJ, 764, 176

Kauffmann G., et al., 2003, Mon. Not. R. Astron. Soc., 346, 1055

Kennicutt Robert C. J., 1998, ApJ, 498, 541

Kennicutt R. C., Evans N. J., 2012, ARA&A, 50, 531

Khochfar S., Silk J., 2011, MNRAS, 410, L42

Kim H., Kim W.-T., 2009, ApJ, 703, 1278

King A., 2003, ApJ, 596, L27

King A. R., Pringle J. E., Livio M., 2007, MNRAS, 376, 1740

King A. R., Pringle J. E., Hofmann J. A., 2008, MNRAS, 385, 1621

King A. L., et al., 2013, ApJ, 762, 103

Kitayama T., et al., 2004, ApJ, 613, 631

Klessen R. S., 2018, arXiv e-prints, p. arXiv:1807.06248

Klessen R., Hennebelle P., 2010, Astron. Astrophys., 520, A17

Koh D., Wise J. H., 2016, MNRAS, 462, 81

Kormendy J., Bender R., 2009, ApJ, 691, L142

Kormendy J., Ho L. C., 2013, Annual Review of Astronomy and Astrophysics, 51, 511

Kormendy J., Richstone D., 1995, Annu. Rev. Astron. Astrophys., 33, 581

Kormendy J., Bender R., Cornell M. E., 2011, Nature, 469, 374

Krumholz M. R., Tan J. C., 2007, ApJ, 654, 304

Lacey C. G., Fall S. M., 1983, MNRAS, 204, 791

Lacey C. G., et al., 2011, MNRAS, 412, 1828

Lamastra A., et al., 2010, MNRAS, 405, 29

Latif M. A., et al., 2013, MNRAS, 436, 2989

Latif M. A., et al., 2014, MNRAS, 443, 1979

Latif M. A., et al., 2016, ApJ, 823, 40

Latif M. A., Volonteri M., Wise J. H., 2018, MNRAS, 476, 5016

Li Y., et al., 2007, ApJ, 665, 187

Li C., et al., 2008, MNRAS, 385, 1903

Lin D. N. C., Pringle J. E., 1987, MNRAS, 225, 607

Lin D. N. C., Pringle J. E., 1990, ApJ, 358, 515

Lodato G., 2007, Nuovo Cimento Rivista Serie, 30, 293

Lodato G., 2012, Advances in Astronomy, 2012, 846875

Lodato G., Natarajan P., 2006, MNRAS, 371, 1813

Lynden-Bell D., 1969, Nature, 223, 690

Madau P., Dickinson M., 2014, ARA&A, 52, 415

Madau P., Rees M. J., 2001, ApJ, 551, L27

Magorrian J., et al., 1998, AJ, 115, 2285

Maio U., et al., 2011, MNRAS, 414, 1145

Marchesini D., et al., 2009, ApJ, 701, 1765

Martig M., et al., 2009, ApJ, 707, 250

Martin G., et al., 2018, MNRAS, 476, 2801

Matthee J., et al., 2015, MNRAS, 451, 400

Mazzucchelli C., et al., 2017, ApJ, 849, 91

McAlpine S., et al., 2016, Astronomy and Computing, 15, 72

McConnell N. J., Ma C.-P., 2013, ApJ, 764, 184

McConnell N. J., et al., 2011, Nature, 480, 215

McGaugh S. S., de Blok W. J. G., 1997, ApJ, 481, 689

Merloni A., Heinz S., di Matteo T., 2003, MNRAS, 345, 1057

Merritt D., 2006, ApJ, 648, 976

Mihos J. C., Hernquist L., 1996, ApJ, 464, 641

Milosavljević M., et al., 2009, Astrophys. J., 698, 766

Mo H. J., Mao S., White S. D. M., 1998, MNRAS, 295, 319

Mo H., van den Bosch F. C., White S., 2010, Galaxy Formation and Evolution. Cambridge University Press

Mortlock D. J., et al., 2011, Nature, 474, 616

Moustakas J., et al., 2013, ApJ, 767, 50

Murray S. G., Power C., Robotham A. S. G., 2013, Astronomy and Computing, 3, 23

Muzzin A., et al., 2013, ApJ, 777, 18

Natarajan P., Volonteri M., 2012, MNRAS, 422, 2051

Navarro J. F., Eke V. R., Frenk C. S., 1996, MNRAS, 283, L72

Navarro J. F., Frenk C. S., White S. D. M., 1997, Astrophys. J., 490, 493

Neistein E., Dekel A., 2008, MNRAS, 388, 1792

Nichols M., Revaz Y., Jablonka P., 2015, A&A, 582, A23

Oñorbe J., et al., 2015, MNRAS, 454, 2092

Oh S. P., Haiman Z., 2002, ApJ, 569, 558

Ohsuga K., et al., 2005, ApJ, 628, 368

Omukai K., Schneider R., Haiman Z., 2008, Astrophys. J., 686, 801

Ostriker E. C., 1999, ApJ, 513, 252

Paardekooper J. P., Khochfar S., Vecchia C. D., 2015, Mon. Not. R. Astron. Soc., 451, 2544

Pacucci F., Volonteri M., Ferrara A., 2015, MNRAS, 452, 1922

Pacucci F., et al., 2017, ApJ, 850, L42

Peacock J. A., 1999, Cosmological Physics. Cambridge University Press

Peng C. Y., et al., 2006, ApJ, 649, 616

Planck Collaboration et al., 2016, A&A, 594, A13

Pontzen A., Governato F., 2012, MNRAS, 421, 3464

Qin Y., et al., 2017, MNRAS, 467, 1678

Reed S. L., et al., 2019, arXiv e-prints, p. arXiv:1901.07456

Rees M. J., 1984, ARA&A, 22, 471

Regan J. A., Haehnelt M. G., 2009, Mon. Not. R. Astron. Soc., 396, 343

Reines A. E., Volonteri M., 2015, ApJ, 813, 82

Rice W. K. M., Lodato G., Armitage P. J., 2005, MNRAS, 364, L56

Romeo A. B., Wiegert J., 2011, MNRAS, 416, 1191

Rybicki G. B., Lightman A. P., 1986, Radiative Processes in Astrophysics. Wiley-VCH

Sakurai Y., et al., 2015, MNRAS, 452, 755

Santoro F., Shull J. M., 2006, Astrophys. J., 643, 26

Schaerer D., 2002, A&A, 382, 28

Schawinski K., et al., 2006, Nature, 442, 888

Schawinski K., et al., 2007, MNRAS, 382, 1415

Schawinski K., et al., 2010, ApJ, 714, L108

Schawinski K., et al., 2014, MNRAS, 440, 889

Schaye J., 2004, ApJ, 609, 667

Schaye J., et al., 2010, MNRAS, 402, 1536

Schleicher D. R. G., et al., 2013, A&A, 558, A59

Schmidt M., 1959, ApJ, 129, 243

Shakura N. I., Sunyaev R. A., 1973, A&A, 500, 33

Shang C., Bryan G. L., Haiman Z., 2010, MNRAS, 402, 1249

Shankar F., Weinberg D. H., Miralda-Escudé J., 2009, ApJ, 690, 20

Sheth R. K., Mo H. J., Tormen G., 2001, MNRAS, 323, 1

Silk J., 1997, ApJ, 481, 703

Silk J., 2013, ApJ, 772, 112

Silk J., Rees M. J., 1998, A&A, 331, L1

Simmons B. D., Smethurst R. J., Lintott C., 2017, MNRAS, 470, 1559

Smith B. D., et al., 2018, MNRAS, 480, 3762

Sobral D., et al., 2015, ApJ, 808, 139

Somerville R. S., Davé R., 2015, ARA&A, 53, 51

Spaans M., Silk J., 2006, ApJ, 652, 902

Springel V., Di Matteo T., Hernquist L., 2005a, MNRAS, 361, 776

Springel V., et al., 2005b, Nature, 435, 629

Stark D. P., et al., 2013, ApJ, 763, 129

Stark D. V., et al., 2018, MNRAS, 474, 2323

Steinborn L. K., et al., 2018, MNRAS, 481, 341

Sutherland R. S., Dopita M. A., 1993, ApJS, 88, 253

Tacconi L. J., et al., 2013, ApJ, 768, 74

Takeo E., et al., 2019, arXiv e-prints, p. arXiv:1901.04514

The LIGO Scientific Collaboration et al., 2018, arXiv e-prints,

Thomas J., et al., 2016, Nature, 532, 340

Toomre A., 1964, ApJ, 139, 1217

Toth G., Ostriker J. P., 1992, ApJ, 389, 5

Trayford J. W., et al., 2016, MNRAS, 460, 3925

Umeda H., et al., 2016, ApJ, 830, L34

Villforth C., et al., 2017, MNRAS, 466, 812

Volonteri M., 2010, Astronomy and Astrophysics Review, 18, 279

Volonteri M., Reines A. E., 2016, ApJ, 820, L6

Volonteri M., et al., 2016, MNRAS, 460, 2979

Wada K., Meurer G., Norman C. A., 2002, ApJ, 577, 197

Wandel A., Petrosian V., 1988, ApJ, 329, L11

Wang B., Silk J., 1994, ApJ, 427, 759

Whalen D., Abel T., Norman M. L., 2004, ApJ, 610, 14

Whitaker K. E., et al., 2014, ApJ, 795, 104

White S. D. M., Rees M. J., 1978, MNRAS, 183, 341

Willett K. W., et al., 2013, MNRAS, 435, 2835

Wise J. H., Abel T., 2007, ApJ, 665, 899

Wise J. H., et al., 2019, arXiv e-prints,

Woosley S. E., Heger A., Weaver T. A., 2002, Reviews of Modern Physics, 74, 1015

Yajima H., Khochfar S., 2016, MNRAS, 457, 2423

Yajima H., et al., 2017, ApJ, 846, 30

Yang G., et al., 2018, MNRAS, 475, 1887

Yuan F., Bu D., Wu M., 2012, ApJ, 761, 130

van den Bergh S., et al., 1996, AJ, 112, 359

van den Bosch F. C., 2017, MNRAS, 468, 885

van den Bosch F. C., et al., 2008, MNRAS, 387, 79